CORRELATION BETWEEN EXCITED STATE ORBITAL PARENTAGE AND EXCITED STATE ACID-BASE BEHAVIOR IN TRANSITION METAL COMPLEXES

by

JIM DIMITRAKOPOULOS

A dissertation submitted to the Graduate Faculty in Chemistry in partial fulfillment of the requirements for the degree of Doctor of Philosophy, The City University of New York

2013

© 2013

JIM DIMIRAKOPOULOS

All Rights Reserved

This manuscript has been read and accepted for the
Graduate Faculty in Chemistry in satisfaction of the
dissertation requirement for the degree of Doctor of Philosophy.

9/11/2013	Dr. Harry D. Gafney
Date	Chair of Examining Committee
9/11/2013	Dr. Maria C. Tamargo
Date	Executive Officer

Dr. Harry D. Gafney

Dr. Thomas C. Strekas

Dr. John R. Lombardi

Supervisory Committee

THE CITY UNIVERSITY OF NEW YORK

Abstract

CORRELATION BETWEEN EXCITED STATE ORBITAL PARENTAGE AND EXCITED STATE ACID-BASE BEHAVIOR IN TRANSITION METAL COMPLEXES.

by

Jim Dimitrakopoulos

Adviser: Professor Harry D. Gafney

Chromium (III) polypyridyl and rhodium (III) polypyridyl complexes have been the subjects of considerable interest because of their extraordinary rich photophysical and photochemical properties. The following complexes were synthesized and studied: bis(2,2'-bipyridine) (2,3-bis (pyridyl)pyrazine) chromium(III){$[Cr(bpy)_2dpp^{3+}]$},tris(2,2'-bipyridine) chromium(III) {$[Cr(bpy)_3]^{3+}$}, bis(1,10-phenanthroline) (2,3-bis(pyridyl)pyrazine) chromium(III) {$[Cr(phen)_2dpp]^{3+}$}, bis(2,2'-bipyridine)(2,3-bis(pyridyl)pyrazine) rhodium(III) $[Rh(bpy)_2dpp^{3+}]$, tris(2,2'-bipyridine) rhodium(III) {$[Rh(bpy)_3]^{3+}$}, and bis(2,2'-bipyridine)bis chloride rhodium(III) {$[Rh(bpy)_2Cl_2]^{+}$}. All chromium polypyridyl complexes studied exhibit only metal-centered emissions (d-d); they display a fluorescence at approximately 695 nm ($^4A_{2g} \leftarrow {}^4T_{2g}$) and a phosphorescence at approximately 730 nm ($^4A_{2g} \leftarrow {}^2E_g$). Quenching of both emissions occurs at high pH, while emission is enhanced at low pH. The $[Rh(bpy)_2dpp]^{3+}$ complex is found to display both metal-centered and ligand-centered emissions. The metal-centered emission (d-d) is the dominant luminescence feature at 77 K in ethanol-

methanol glasses (4:1 v/v), but the ligand-centered ($\pi \rightarrow \pi^*$) emission is enhanced relative to the metal-centered luminescence in fluid acetonitrile solutions. The bis complex, $[Rh(bpy)_2C1_2]^+$, displays a dominant metal centered emission under all conditions that were studied. The $[Rh(bpy)_3,]^{3+}$ complex emits only from ligand-centered excited states at 77K. From this thesis, it became clear that the excited-state properties of a complex are related to the energy ordering of its low-energy excited states and, particularly, to the orbital nature of its lowest excited state. The energy positions of the MC, MLCT, and LC excited states depend on the ligand field strength, the redox properties of metal and ligands, and intrinsic properties of the ligands, respectively. Thus, in a series of complexes of the same metal ion, the energy ordering of the various excited states, and particularly the orbital nature of the lowest excited state, can be controlled by the choice of suitable ligands. It is therefore possible to design complexes having, at least to a certain degree, desired properties.

I dedicate this thesis to my family.

Αφιερώνω αυτή την διατριβή στην οικογένειά μου.

ACKNOWLEDGEMENTS

Above all and foremost I would like to thank my mentor Dr. Harry D. Gafney. I want to thank you for all you have taught me in chemistry. The knowledge and wisdom you have imprinted upon me will serve as a great help and support throughout my career and my life for that matter. I believe my success is in a large part due to your sincere support and mentorship. I want to express my deepest gratitude for believing in me. You have been an excellent teacher, mentor and a great inspiration for me. You have inspired me to pursue my goals with hard work and dedication. I truly appreciate and value everything I have learned from you. Thank you for infinite patience and for being so generous with your time.

I would like to thank Dr. Gerald Koeppl for his mentorship, support, encouragement, advice and kind words.

I want to thank my parents, Panagiotis and Theone Dimitrakopoulos, for their unconditional love, prayers, endless support, financial assistance and all the sacrifices they had to make. My sisters Foteini and Anggeliki, although we have been apart for so many years you were never far from my thoughts.

I want to thank my grandparents Dimitris and Foteini Dimitrakopoulos, Elias and Anggeliki Fertakis for their love and constant support.

I want to thank Eleni Damanakis for her love, support, friendship, jokes and infectious smile.

I want to thank my Godmother Maria Eliades and my best friend Damiamos Eliades for providing a home for me away from home.

I want to thank my thesis committee members, Dr. Thomas C. Strekas and Dr. John R. Lombardi, for their longsuffering and keen insights.

I want to thank all my friends and family members, both here in the United States and back home in Patrai, Greece, especially my uncle Sam Dimos and my friend Antonios Balassis.

I want to thank all my lab mates, past and present, Dr. Jose Zambrana, Marta Kowalczyk, Dr. Elena Ferloni, Anthony Perri, Ester Frederick, Dr. Sunil Dehipawala, Dr. Shanta Amarasinge, Dr. Rolande Hodel, but especially Dr. Edward Look for his friendship and constant support, Dr. Julie Colis Leventhal a.k.a. the lady with the magic touch and the laser whisperer, for her enormous help with lifetime measurements and, of course, Dr. Parbatee Samaroo Jagassar for being such a great friend and cheerleader.

I want to thank Diane Adebowale and Vivian Mason of the Doctoral Chemistry Office, for their kind and encouraging words and great organization.

I want to thank Molash Alemayehu, Jeanne Deutsch and Linda Didomenick Queens College Department of Chemistry & Biochemistry secretaries who make working at Queens College a pleasure.

Table of Contents

List of Tables

List of Figures

BISC, back intersystem crossing
bpy, 2,2"-bipyridine
dpp, 2,3-bis-(pyridyl)pyrizine
CT, charge transfer
ε, molar extinction coefficient in units of M^{-1} s^{-1}
ES, excited state
Φ°, quantum yield
Φ_A, quantum yield for process A
F, fluorescence
GS, ground state
IC, internal conversion
IL, intra-ligand
ISC, intersystem crossing
LC, ligand centered
LEES, lowest energy excited state
λ_{ex}, excitation (irradiation) wavelength
LF, ligand field
LLCT, ligand to ligand charge transfer
LMCT, ligand to metal charge transfer
MC, metal centered
phen, 1,10-phenanthroline
MLCT, metal to ligand charge transfer
MO, molecular orbital
NHE, normal hydrogen electrode
NR, non-radiative
P, phosphorescence
SCE, saturated calomel electrode
SSCE, saturated sodium chloride calomel electrode
VR, vibrational relaxation
k^o_F , inherent rate constant for fluorescence
k^o_P, inherent rate constant for phosphorescence
τ^o_F, lifetime due only to fluorescence
τ^o_P, lifetime due only to phosphorescence
k_{ST}, rate for intersystem crossing from an excited singlet state to an excited triplet state
k_{TS}, rate for intersystem crossing from an excited triplet state to a ground singlet state
T_n, where n>1, upper excited triplet states
S_n, where n>1, upper excited singlet states
k_{isc}, rate constant for intersystem crossing
hν, light energy
CV, cyclic voltammetry
HOMO, highest occupied molecular orbital
LUMO, lowest occupied molecular orbital
r.t., room temperature

CHAPTER 1

1. INTRODUCTION

1. A. CONTEXT / GENERAL CONSIDERATIONS

Transition metal complexes with organic ligands have been investigated with increasing interest over the last few decades, since these complexes exhibit an enormous potential for the discovery of new physical and chemical properties and applications. For example, their photo-redox properties can be utilized for solar energy conversion, organic light emitting diodes, in medicine, for the treatment of cancer and drug delivery systems, and in genetics, as DNA probes. All of these systems require a specific and controlled response to an external input of energy, and early investigations of the photophysical and photochemical properties of coordination compounds suggested that transition metal complexes were ideal candidates for the fulfillment of many of these functions. Most of the possible applications are related to the properties of the lowest excited electronic states. Thus, these are the states that are extensively studied in great detail. In particular, they exhibit a series of not fully-elucidated electronic properties, which are found neither in already well-studied pure organic molecules nor in simple metal complexes with d-d* transitions. More specific, the lowest excited states of $[Rh(bpy)_3]^{3+}$ can be classified as ligand centered (LC) of (bpy)π-π* ,although slightly distorted by the metal, those of $[Ru(bpy)_3]^{2+}$ result from metal-to-ligand charge-transfer (MLCT) of (Ru)4d-(bpy)π* character, while those of $[Cr(bpy)_3]^{3+}$ are considered to be metal centered (MC) of (Cr)3d-3d* character. These three types of transitions may be regarded as three extreme situations, which lead to distinctly different properties of the corresponding compounds. Figure 1 shows a generic molecular orbital (MO) diagram for a transition metal complex

in octahedral (O_h) symmetry representing the three aforementioned transition metals. More information on the molecular orbital diagram shown below is given in section 1. D.

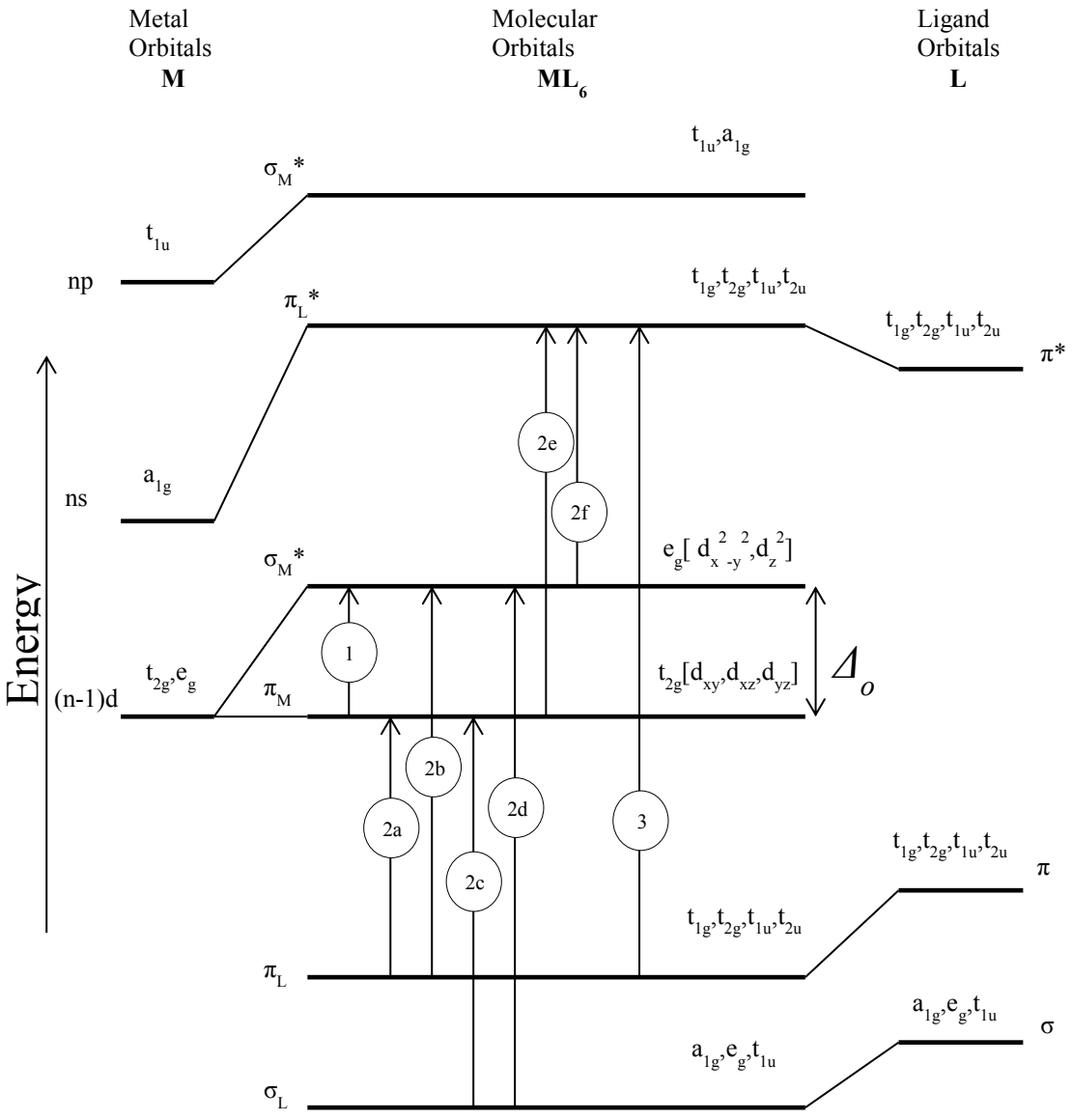

Figure 1. Schematic orbital energy diagram representing various types of electronic transitions in octahedral complexes.
1: Metal centered transition (MC)
2a, 2b, 2c, 2d: ligand-to-metal charge transfer transitions (LMCT)
2e, 2f: metal-to-ligand charge transfer transitions (MLCT)
3: Internal ligand transition (LC)

Charge transfer, especially metal-to-ligand charge transfer (MLCT) excited states generally gather the most attention. Since, the photoredox properties of $[Ru(bpy)_3]^{2+}$ were first suggested by Gafney and Adamson and confirmed by others, Ru(II) tris-diimine complexes have been unquestionably one of the most extensively studied transition metal complexes and most widely used in research laboratories. A unique combination of chemical stability, redox properties, excited state reactivity, luminescence emission, and excited state lifetime has attracted the attention of many research workers first on this complex and then on some several hundred of its derivatives. The great interest generated by the study of this class of complexes has stimulated the growth of several branches of pure and applied chemistry. In particular, the Ru(II)polypyridyl complexes have played and are still playing a key role in the development of photochemistry, photophysics, photocatalysis, electrochemistry, photoelectrochemistry.

A few years after the Gafney and Adamson article appeared, Bolleta et al. presented the first evidence that the ligand-field ^2E_g excited state of $[Cr(bpy)_3]^{3+}$ was a strong one-electron photooxidant, and displayed a long-lived room temperature luminescence. However, Cr(III) polypyridyl complexes, along with Rh(III) polypyridyl complexes, have received comparatively little attention relative to analogous Ru(II) polypyridyl complexes. This neglect may arise in part from the somewhat more difficult synthetic chemistry of Cr(III) polypyridyl complexes, with efficient means to produce heteroleptic complexes only afforded by recently published methodologies, and the fact that Rh(III) polypyridyl complexes are not emissive at room temperature.

The aims of this thesis are to synthesize polypyridyl complexes of Cr(III) and Rh(III), collect data concerning the absorption and emission, investigate the excited state properties of these complexes in solution and compare them with those of Ru(II) polypyridine complexes. Figures 2 and 3 show the structures of the complexes synthesized and studied in this thesis.

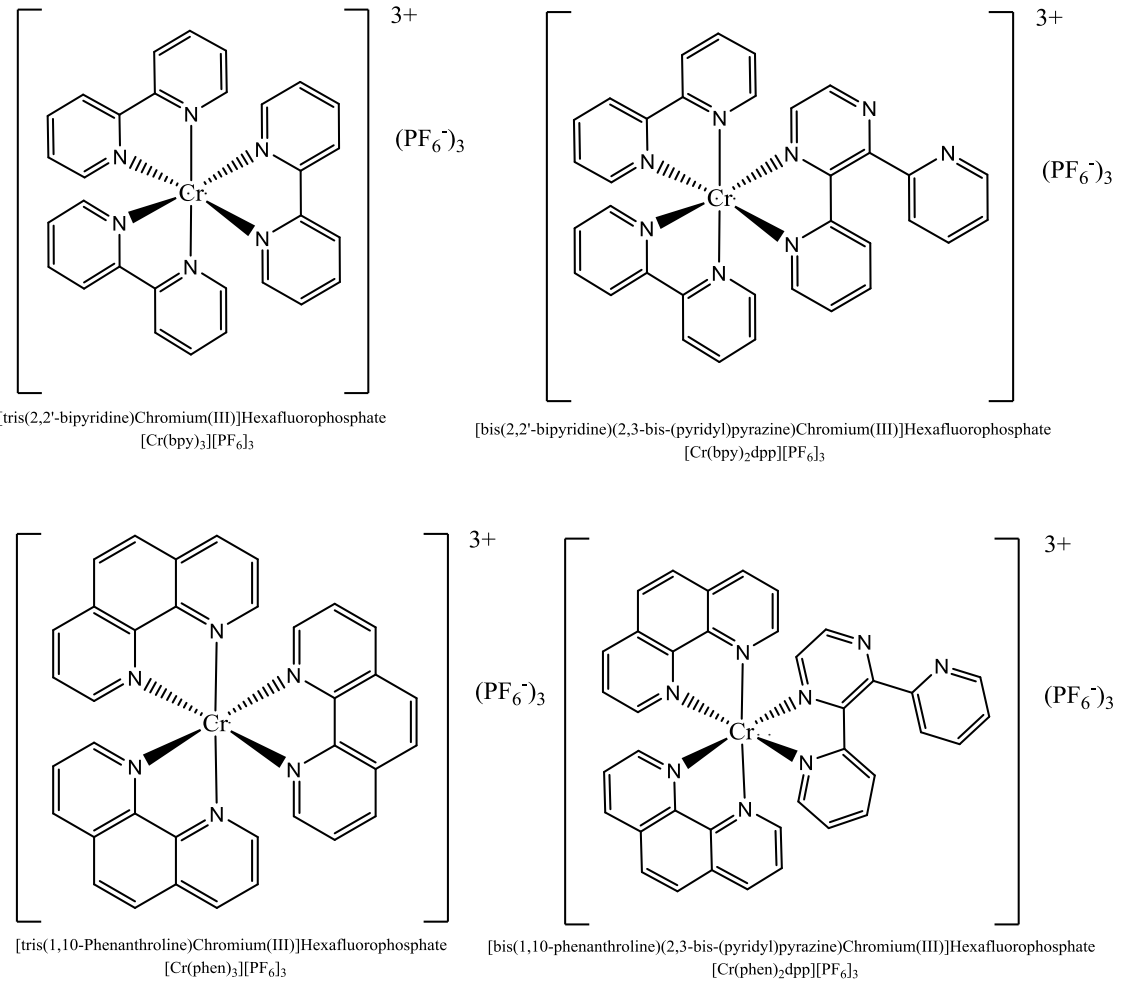

Figure 2. Chromium (III) polypyridine complexes.

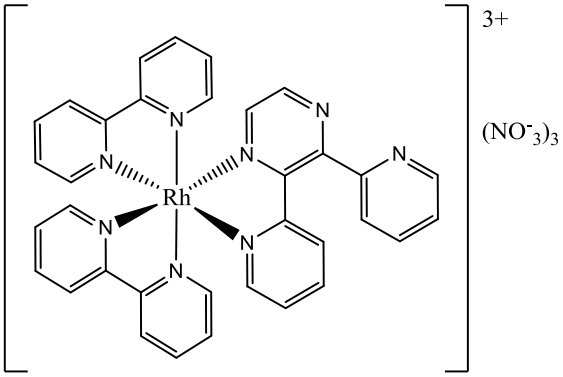

bis(2,2'-bipyridine)(2,3-bis-(pyridyl)pyrazine)Rhodium(III)nitrate
$[Rh(bpy)_2dpp][NO_3]_3$

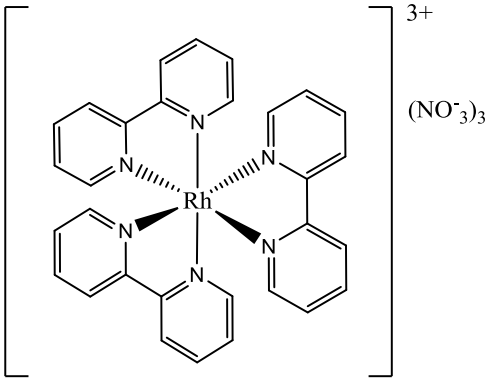

tris(2,2'-bipyridine)Rhodium(III)nitrate
$[Rh(bpy)_3][NO_3]_3$

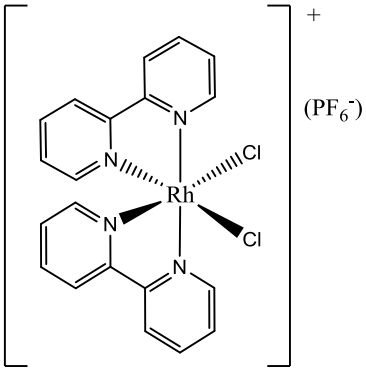

[bis chlorine bis(2,2'-bipyridine) Rhodium(III)]Hexafluorophosphate
$[Rh(bpy)_2Cl_2][PF_6]$

Figure 3. Rhodium (III) polypyridine complexes.

1. B. QUANTUM MECHANICS IN PERSPECTIVE

The quantitative treatment of electronic excitation and the absorption and emission of radiation by chemical species falls within the realm of wave mechanics. A fundamental concept of quantum mechanics is that matter has wave-like properties. This attribute is normally not evident for macroscopic objects but it dominates the nature of subatomic particles such as the electron. An electron is described by a wavefunction, Ψ, which is a mathematical function of the position coordinates x, y and z and of the time t. The wavefunction for an electron is found by solving the Schrödinger equation:

$$H \Psi = E \Psi \qquad (1)$$

where H is the Hamiltonian operator acting on Ψ, the wavefunctions of electrons, to yield a set of eigenvalues of the energies, E. When this equation is solved for a free electron it is found that there is no restriction on the energy, so it can exist with all possible energies. However, when the equation is solved for an electron that that is bound to an attractive center, it is found that acceptable solutions can be obtained only for certain energies. Thus, we speak of the energy as being quantized, meaning that species can exist only in certain defined, discrete energy states. A transition, between two such states of specific energy, must also have associated with it a definite energy. A direct result of the quantization of energy levels is that, for each individual species only specific energies, and therefore frequencies or wavelengths, of radiation can be adsorbed or emitted. The characteristic line and band spectra of chemical species are a consequence of this behavior.

Molecules, in addition to electronic energy, which depends on the distance of the

electron from the nucleus and the type of orbital it occupies, possess other sorts of internal energy: specifically rotational energy and vibrational energy. Each of these energies is quantized and arises from the periodic oscillations of atoms in a molecule. When a molecule adsorbs a quantum of radiation, it becomes excited. How the molecule assimilates that energy- in rotational, vibrational or electronic modes- depends on the wavelength of the incident radiation. The longer the wavelength of electromagnetic radiation the lower the energy is. As the molecular rotational and vibrational energy levels are closer together in energy than the electronic levels, absorption at the lower energies associated with infra-red radiation usually only leads to transitions between rotational or vibrational states of the molecules. The energy of radiation in the visible to ultraviolet region, however, induces transitions between the electronic energy levels of a molecule. It is assumed for simplicity that electronic, vibrational and rotational energy are entirely independent because of the great differences in frequency or wavelength between the three types of motion. This is a known as the Born-Oppenheimer approximation. A further consequence of this assumption forms the basis of the Franck-Condon principle. The idea behind the principle is that the nuclei of a molecule can be assumed to be fixed during an electronic transition, so that the transition can be presented on a potential energy diagram as a vertical line between upper and lower states as illustrated in Figure 4.

1. C. ENERGY LEVEL DIAGRAM

One way to view the properties of molecular excited states is shown by the potential energy diagram in Figure 4, known as a Franck-Condon energy level diagram. The Franck-Condon principle is of a basic importance for processes involving electronically excited states. This principle states that electronic transitions are so fast (10^{-15} s) in comparison to nuclear motion (10^{-12} s) that, during the act of the electronic transition, the nuclei do not alter appreciably their relative positions or their kinetic energies. This diagram shows potential energy curves for the ground state (S_o), and first excited singlet state (S_1) of a complex as a function of internuclear distance, r. These curves are sometimes referred to as potential energy wells, because of their shape. The horizontal lines within each curve represent the vibrational levels of each electronic state. The lowest vibrational state for each energy level is designated as 0, and the levels above it are successively 1, 2, and so on. As shown in Figure 4, an excited state will generally differ from the ground state not only for its higher energy, but also for the different equilibrium nuclear separation. When considering two atoms bonded to each other, the bottom of the well corresponds to the equilibrium bond length. Because excitation involves the movement of electron density from a bonding or non-bonding orbital into an antibonding orbital, the bond of the complex in the excited state is weakened, consequently the equilibrium bond length in S_1 is generally longer than in S_0. This is illustrated in Figure 4 by the slight displacement of the S_1 well to the right of the S_0 well. At room temperature, most of the complexes are in the lowest (ν=0) vibrational level of the electronic ground state. One key feature of the Franck-Condon principle is that only

vertical transitions are allowed since instantaneous changes in bond length cannot occur, and results in the complex having excess vibrational energy. The excess vibrational energy can be dissipated through the non-radiative process of vibrational relaxation, which returns the complex to the lowest vibrational level of S_1. The radiative process of fluorescence usually occurs from the lowest vibrational level of S_1. Because these transitions occur at lower energies than absorption, fluorescence is observed at longer wavelengths (λ) than absorption (Stokes shift), as shown Figure 4.

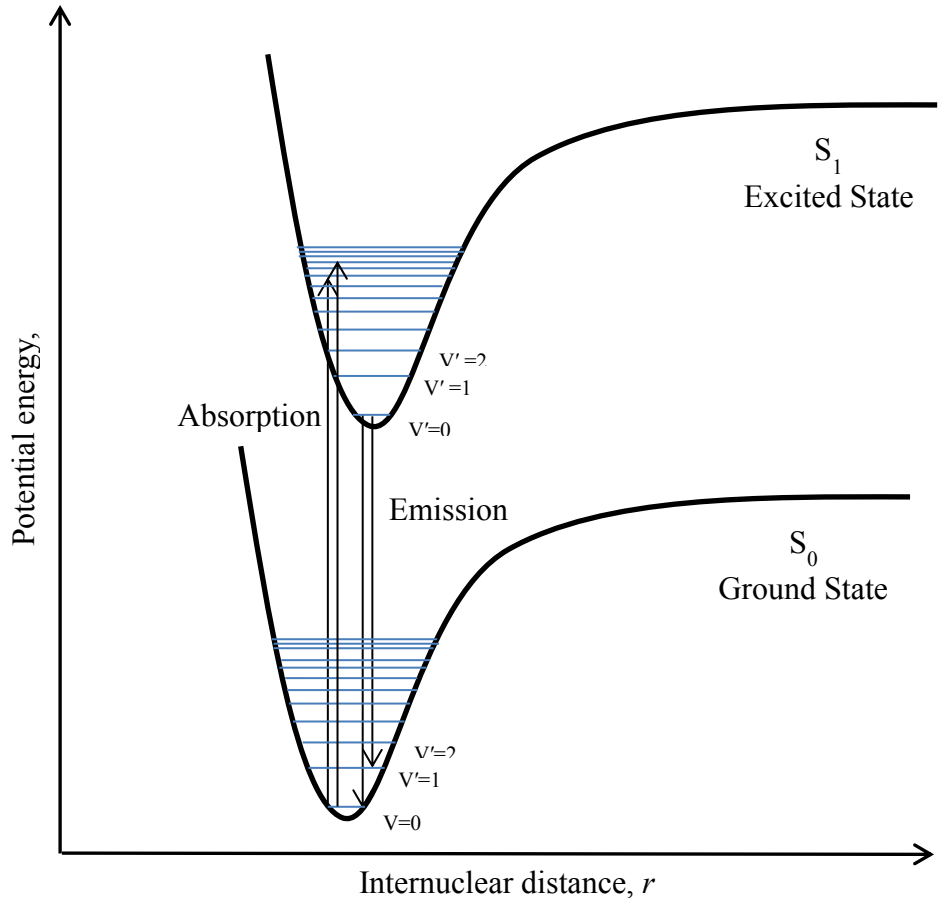

Figure 4. Franck-Condon Principle.
Absorption and emission from vibrational levels within electronic states.

1. D. CRYSTAL FIELD THEORY AND MOLECULAR ORBITAL THEORY

Crystal field theory was first applied to the magnetic properties of the transition metal ions and has been widely used to explain the so-called d-d spectra of complexes in the visible region. Moreover, the stability of coordination compounds of the transition elements could be further understood by applying this theory.

The essence of crystal field theory is that the five d orbitals, which are degenerate and equal in energy in the gaseous metal ion, become differentiated in the presence of the electrostatic field due to the ligands.

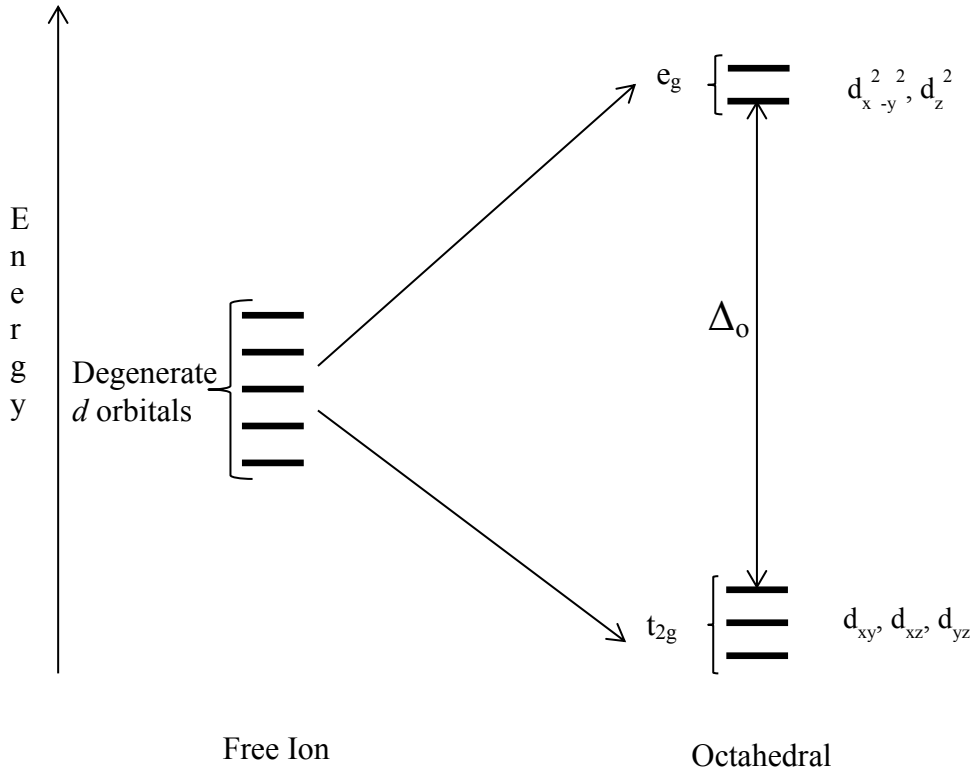

Figure 5. Octahedral ligand field splitting of d orbitals.

In an octahedral complex the d_{x2-y2} and d_{z2} orbitals are raised in energy relative to the d_{xy}, d_{yz} and d_{xz} orbitals. Those orbitals lying in the direction of the ligands are raised in energy with respect to those lying away from the ligands. By preferentially filling the low-lying levels, the *d* electrons can stabilize the system, as compared to the case of random filling of the *d* orbitals. The gain in bonding energy achieved in this way is called the crystal field stabilization energy (C.F.S.E.). It is caused by the distribution of charge around the central atom of the complex not being symmetrical. If the *d* orbitals were occupied equally, the resulting electron density would have spherical symmetry.

Ligand field theory is the application of molecular orbital (M.O.) theory only to the *d* orbitals. In M.O. theory, the wavefunction of a molecule is described as the superposition of linearly combined atomic orbitals, resulting in the same number of molecular orbitals, having energies similar to, greater than, and lower than those atomic orbitals. The electrons are assumed to move in molecular orbitals which extend over all the nuclei of the system. Figure 1 shows a molecular orbital (MO) diagram for a transition metal complex in O_h symmetry. In this diagram, possible σ-donor, π-donor, and π-acceptor orbitals are included. The subscripts indicate whether the MO is predominantly metal (M) or ligand (L) in character. The π_M and σ_M^* orbitals in the center of the MO diagram are predominantly metal d-orbitals with t_{2g} and e_g symmetry, respectively. In the case of a ligand that is exclusively a sigma donor (such as bpy and phen), the π_M MOs are non-bonding. For ligands that are both σ- and π-donating (e.g. the halides), the π_M MO's are antibonding with respect to the M–L bond; and for ligands with dominant π-acceptor

character, the π_M MO's are bonding. Notably, the predominantly metal e_g MO's are always antibonding with respect to the M–L bond.

Excited configurations can be obtained from the ground state configuration by promoting one electron from occupied to vacant MO's. At relatively low energies, one expects to find electronic transitions of the following types (Figure. 1): metal-centered (MC) transitions from π_M orbitals of t_{2g} symmetry to σ_M^* orbitals of e_g symmetry (1); ligand-centered (LC) transitions from π_L orbitals to π_L^* orbitals (3); ligand-to-metal charge-transfer (LMCT) transitions from π_L orbitals to σ_M^* orbitals of e_g symmetry (2b); and metal-to-ligand charge-transfer (MLCT) transitions from π_M orbitals of t_{2g} symmetry π_L^* orbitals (2e). The relative energy ordering of the resulting excited electronic configurations depends on the nature of metal and ligands in more or less predictable ways. Relatively low-energy metal-centered transitions are expected for metals of the first transition row; such as chromium (III) polypyridyl complexes. Higher energy metal-to-ligand charge-transfer transitions are expected when the metal is easy to oxidize and a ligand is easy to reduce, such as ruthenium (II) polypyridyl complexes. Ligand-centered transitions are expected for aromatic ligands with extended π and π^* orbitals and not easily oxidized metals, such as rhodium(III) polypyridyl complexes.

Figure 6 shows the molecular orbital diagram of a chromium(III) polypyridyl complex. The Pauli Exclusion Principle requires that each MO be populated with no more than two electrons, while the Aufbau principle requires that the orbitals are filled from the MO with lowest energy to that with the highest. Furthermore, Hund's rules

states that the lowest energy state is comprised of the least amount of electron spin pairing,

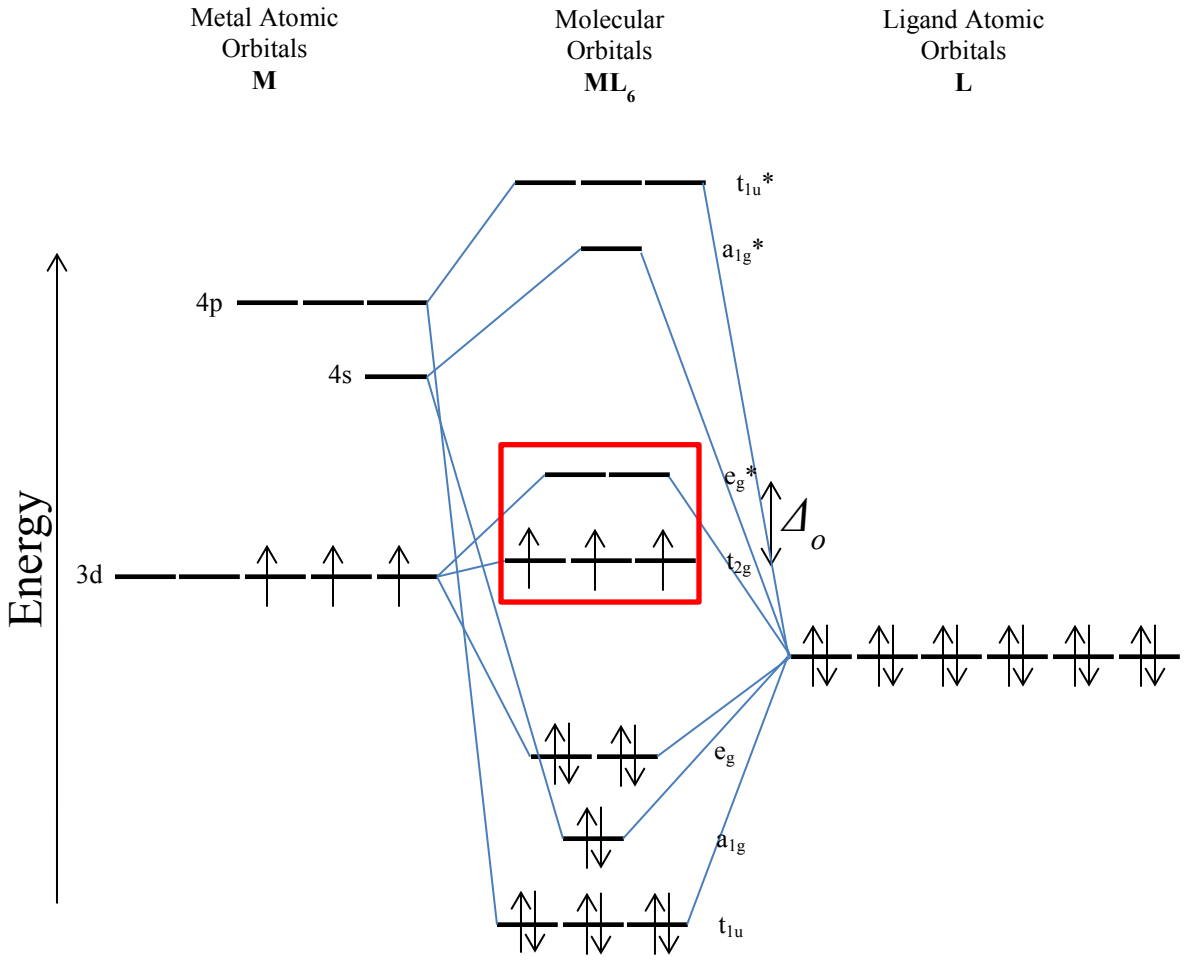

Figure 6. Molecular orbital diagram of Cr(III) complex.

1. E. SELECTION RULES FOR ELECTRONIC TRANSITIONS

It is frequently the spin, orbital momentum, and symmetry properties of the two wavefunctions in the excited (upper) and ground (lower) states that determine whether or not an interaction with electromagnetic radiation is possible. Individual electrons possess both spin angular momentum and orbital angular momentum. These momenta are vector quantities; there are therefore angular momenta associated with a species resulting from the vector addition of the spin and orbital angular momenta, a process known as spin-orbit coupling. This process of combining electron angular momenta by summing first the spins, then the orbital momenta, and finally the two resultants is called Russell-Saunders coupling. Level notation is accordingly based on this scheme, and the symbol characterizing each level has the form $^{2S+1}L_J$ where S is the total spin quantum number, J is the total angular momentum quantum number, and L is the orbital quantum number.

The intensities of transitions in complexes depend on the strength with which the complex couples with the electromagnetic field. Intense transitions indicate strong coupling, while, weak transitions indicate feeble coupling. The strength of coupling when an electron makes a transition from a state with wavefunction ψ_i to one with wavefunction ψ_f is measured by the transition dipole moment, which is defined as the integral

$$\mu_{fi} = \int \psi_f \, \mu \, \psi_i \, d\tau \qquad (2)$$

where μ is the electric dipole moment operator $-er$, e is charge of the electron and the integration takes place over spatial coordinates r. An allowed transition is a transition

with a nonzero transition dipole moment, and hence nonzero intensity. A forbidden transition is a transition for which the transition dipole moment is calculated as zero.

The Selection Rules governing transitions between electronic energy levels of transition metal complexes are:

1. $\Delta S = 0$ The Spin Rule
2. $\Delta \ell = +/- 1$ The Orbital Rule (Laporte)

The first rule states that allowed transitions must involve the promotion of electrons without a change in their spin. In other words, transitions that involve a change in multiplicity are forbidden. The Laporte selection rule reflects the fact that for light to interact with a molecule and be absorbed there should be a change in dipole moment. When a transition is forbidden, it means that the transition does not lead to a change in dipole moment. The Laporte selection rule states that transitions where there is no change in parity are forbidden:

$$g \not\rightarrow g \quad u \not\rightarrow u \qquad g \rightarrow u \quad u \rightarrow g$$

Forbidden Allowed

Consequently, charge transfer bands, which are Laporte and spin allowed, are very intense, while, metal centered, which are Laporte and spin forbidden, are very weak. Relaxation of these selection rules can occur through: 1) Spin-Orbit coupling, where this gives rise to weak spin forbidden bands; 2) Vibronic coupling, where an octahedral complex may have allowed vibrations, thus the complex becomes asymmetric and

absorption of light at that moment is then possible; 3) Mixing of states, where π-acceptor and π-donor ligands can mix with the d-orbitals so transitions are no longer purely d-d.

1. F. THE BEER-LAMBERT LAW

Absorption is treated quantitatively by using the Beer-Lambert law. This law gives the fraction of monochromatic light transmitted through an absorbing system. The mathematical expression of this law is giving by the following relations:

$$T = I_t/I_0 = 10^{-\varepsilon bc} \quad (3)$$

$$A = -\log (I_t/I_0) = -\log (10^{-\varepsilon bc}) = \varepsilon bc \quad (4)$$

where I_t and I_0 are transmitted and incident light intensities, c is the concentration of the absorber, b is the pathlength of the sample holder through which the light beam has passed, and ε is molar extinction coefficient. The relationship follows naturally from the assumption that the rate of loss of photons is proportional to the rate of bimolecular collisions between photons and the absorbing species. The Beer-Lambert law is of particular importance in determining the intensity of absorbed radiation in photochemical experimentation, and in calculating concentrations from absorption measurements.

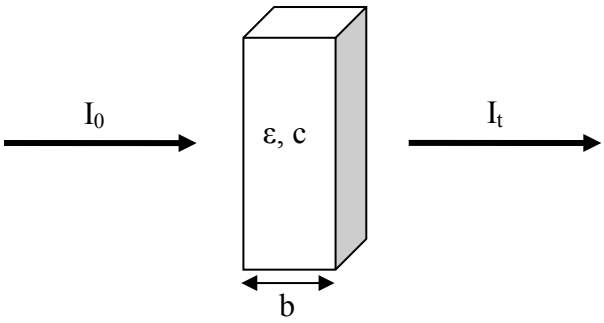

Figure 7. Diagram of Beer–Lambert absorption of a beam of light as it travels through a cuvette of width b.

1. G. LIGHT ABSORPTION AND FATE OF EXCITATION ENERGY

Absorption of light is the first process involved in a photochemical or photophysical sequence:

$$D + h\nu \rightarrow D^*$$

The absorption of radiation by an atom or molecule leads to the production of an electronically excited species that can exhibit new chemistry that is different from that of the parent, ground state species. Not only does the species possess more energy, but it can also participate in different reactions as a result of the new electronic arrangement. The electronically excited molecules obtained must, within a more or less short time, lose their excess energy in order to place themselves in equilibrium with the surrounding medium. The deactivation is achieved through either radiative or nonradiative processes. Radiative processes are always first order processes and involve the emission of light (figures 8 and 9). The nonradiative processes may be further subdivided into chemical and physical; chemical are second order processes and involve the interaction of the excited molecule with a quencher (bimolecular quenching), while physical are pseudo first order and involve the dissipation of energy absorbed through heat into the surrounding medium (figures 8 and 9).

Scheme 1

$D^* \rightarrow D + h\nu$	Radiative deactivation
$D^* \rightarrow D + \text{heat}$	Nonradiative deactivation
$D^* + Q \rightarrow D + Q^*$	Nonradiative deactivation (Bimolecular Quenching)

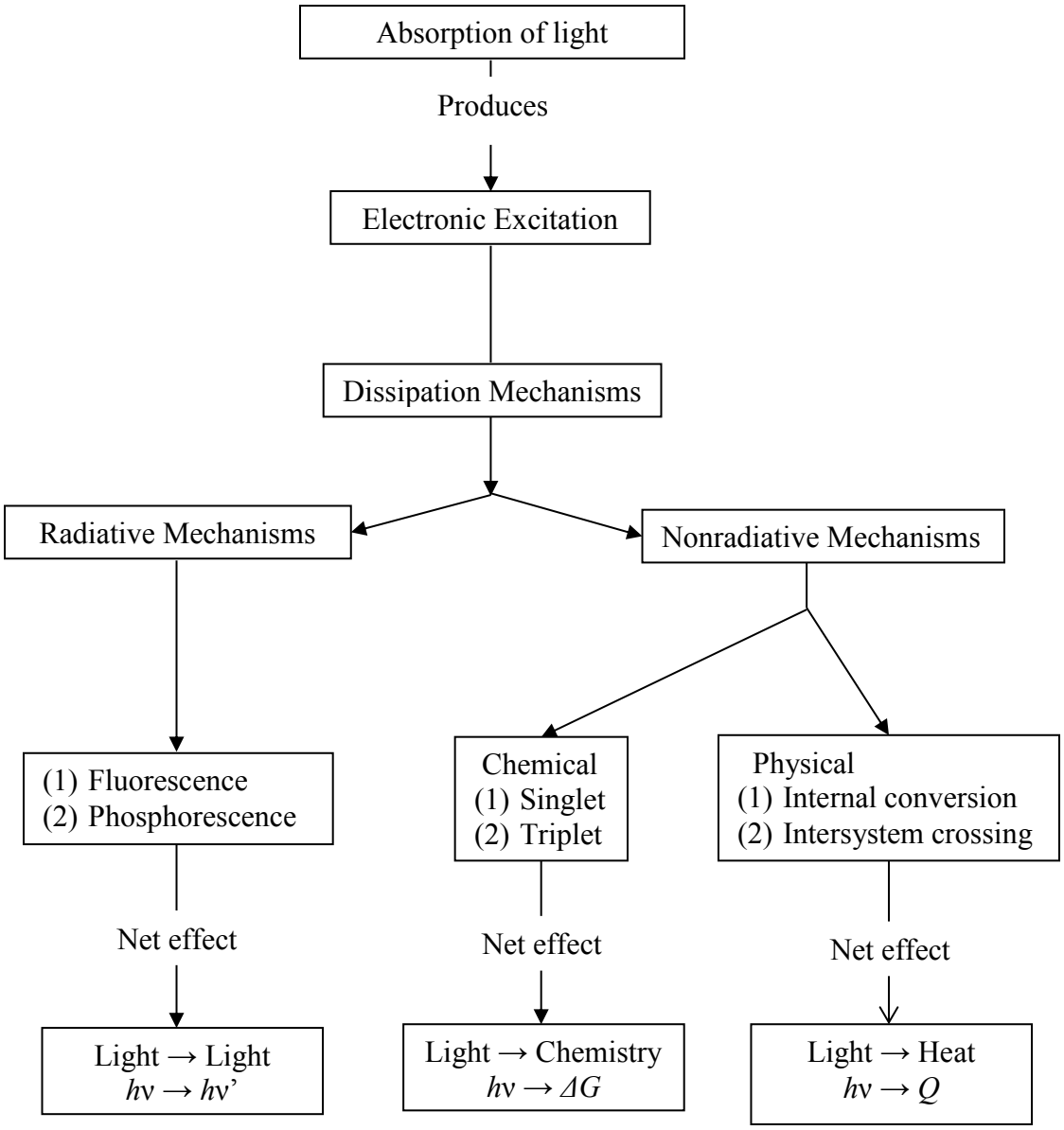

Figure 8. A schematic representation of photochemical dissipation mechanisms.

1. H. PLAUSIBLE FATES OF EXCITED SPECIES

Figure 9 is a Jablonski diagram for a species with a singlet ground state (S_o), two excited singlet states (S_1 and S_2) and two excited triplet states (T_1 and T_2). As shown, there are several photophysical pathways for excited state deactivation in addition to excited state chemical reactions. Internal conversion and fluorescence are non-radiative and radiative, respectively, transitions between states of the same spin multiplicities. Vibrational relaxation is an energy dissipation mechanism within the same state. Intersystem crossing and phosphorescence are non-radiative and radiative transitions, respectively, between states of different spin multiplicities. Transitions between states of the same spin multiplicity are allowed and fast, while transitions between states of different spin multiplicities are forbidden and, thus, slow. Non-radiative decay leads from the electronic excited state to the ground state without concomitant emission of light. The possible deactivation pathways and their rates constants are shown in Scheme 1.

Scheme 1.

Excitation	$h\nu + S_0 \rightarrow S_1$	Rate = I_a
Internal Conversion	$S_1 \rightarrow S_0$ + heat	Rate = $k_{IC}[S_1]$
Intersystem Crossing	$S_1 \rightarrow T_1$ + heat	Rate = $k_{ISC}[S_1]$
Intersystem Crossing	$T_1 \rightarrow S_0$ + heat	Rate = $k'_{ISC}[T_1]$
Phosphorescence	$T_1 \rightarrow S_0 + h\nu$	Rate = $k_{Ph}[T_1]$
Fluorescence	$S_1 \rightarrow S_0 + h\nu$	Rate = $k_F[S_1]$

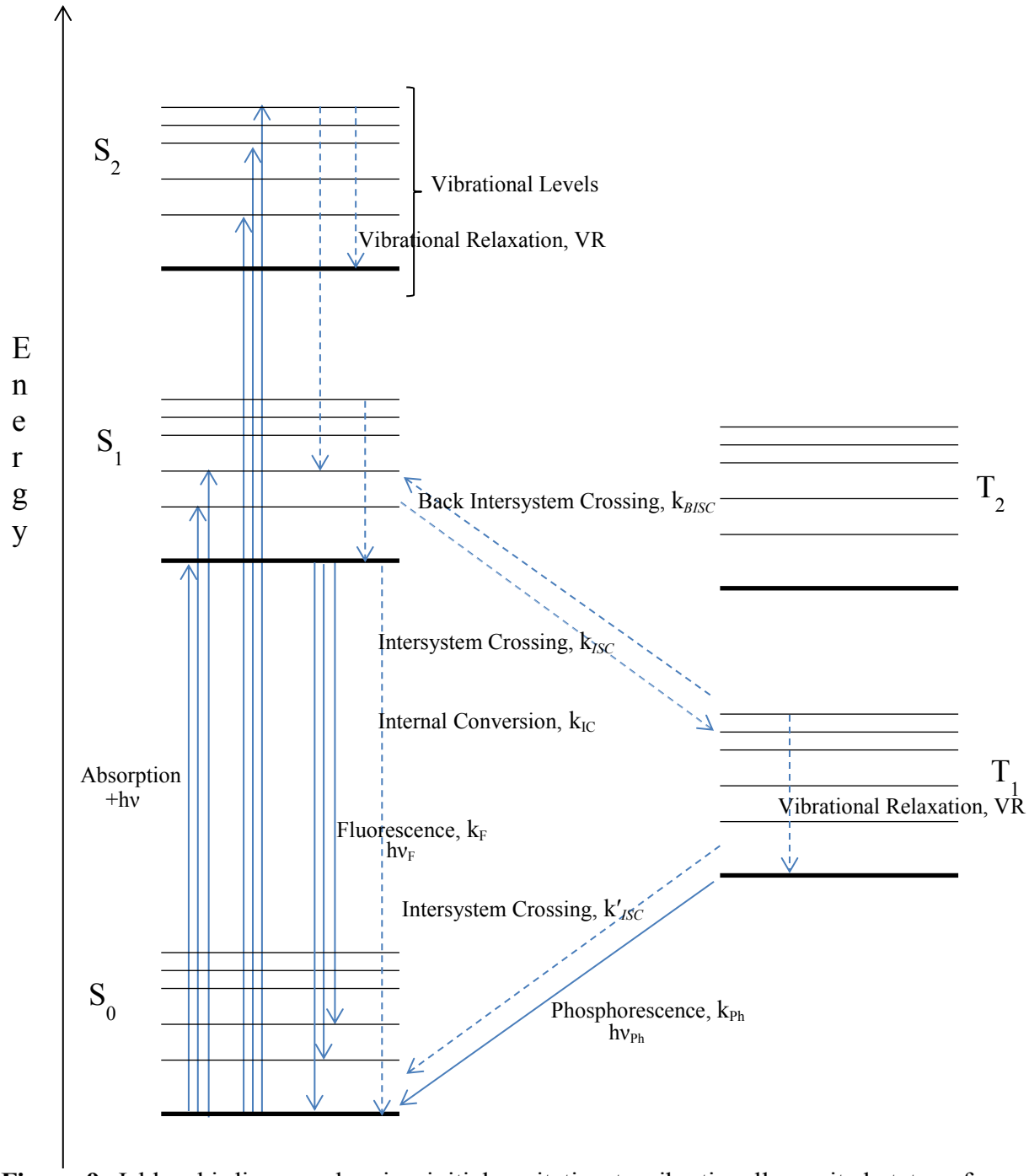

Figure 9. Jablonski diagram showing initial excitation to vibrationally excited states of S_1 and S_2, vibrational relaxation (VR), internal conversion (IC), intersystem crossing (ISC), back intersystem crossing (BISC), fluorescence (F), phosphorescence (Ph), and non-radiative decay (NR). By convention, processes involving absorption or emission of a photon are designated by a straight line, while nonradiative processes are designated with a doted or wavy arrow.

1. I. LUMINESCENCE

Luminescence is the emission of light from any substance and occurs from electronically excited states. Luminescence can be divided into two categories: phosphorescence and fluorescence. Phosphorescence is the emission of light from triplet-excited states, in which the electron in the excited orbital has the same spin orientation as the ground-state electron. Transitions to the ground state are forbidden and the emission rates are slow (10^{-1} to 10^{6} s^{-1}), so phosphorescence lifetimes are typically milliseconds to seconds.

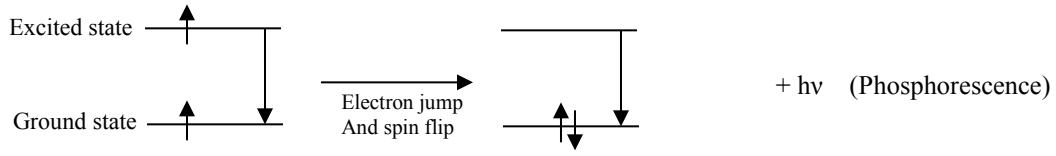

Figure 10. Energy level diagram for phosphorescence.

Fluorescence, on the other hand, is emission of light from singlet-excited states, in which the electron in the excited orbital has an opposite spin orientation as the electron in the ground-state orbital. Return to the ground-state is spin-allowed and occurs rapidly by emission of a photon. Emission rates of fluorescence are typically $10^{8}s^{-1}$, and a typical fluorescence lifetime is ≤ 10 ns.

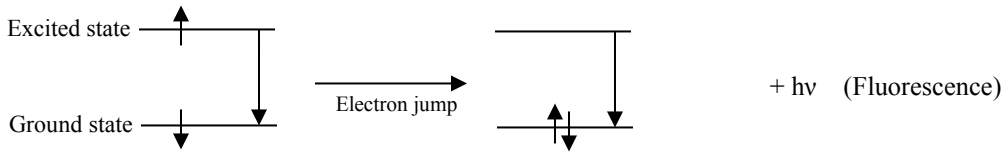

Figure 11. Energy level diagram for florescence.

1. J. BIMOLECULAR QUENCHING MECHANISMS

Quenching refers to any process that leads to a decrease in luminescence intensity. Photophysically, this can occur through a loss of absorption or a decrease in quantum yield. The quenching of luminescent molecules provides useful information on the nature of bimolecular interactions in free solution. More specific, analysis of the time-resolved and steady-state emission data yield invaluable information on the nature of the interaction and proximity between the fluorophore and the quencher. In most steady-state luminescence experiments, data is presented in the form of Stern-Volmer plots where the quenching efficiency is related to the total quencher concentration. In homogeneous solvents of low viscosity, linear Stern-Volmer plots are obtained and the bimolecular rate constant may be calculated assuming that the excited-state lifetime of the luminophore is known.

$$I_o/I = 1 + k_q\tau_o[Q] = 1 + K_{SV}[Q] \qquad (5)$$

where I and I_o are the intensities in the presence and absence of quencher, respectively, k_q is the diffusion-controlled bimolecular quenching constant, and τ_o is the lifetime in the absence of the quencher. The product $k_q\tau_o$ is labeled as K_{SV}, the Stern-Volmer constant. Scheme 1 shows the possible deactivation pathways by a quencher following excitation.

Scheme 1

$$^*D + Q \xrightarrow{k'} D + Q + \Delta \qquad \text{Exchange Energy Transfer} \qquad (I)$$

$$^*D + Q \xrightarrow{k''} D + Q^* \qquad \text{Resonance Energy Transfer} \qquad (II)$$

$$^*D + Q \xrightarrow{k'''} D^{\pm} + Q^{\pm} \qquad \text{Electron Transfer} \qquad (III)$$

where D and *D are the ground and excited state form of the donor species under study. Q is a quencher which can, on close interaction with the excited donor *D, deactivate it by a catalytic step (I), and energy transfer (II), or an excited state electron transfer (III). $D^{\pm}$ and $Q^{\pm}$ are the oxidized and reduced forms of the donor and quencher, respectively. k', k'' and k''' are the rate constants for each step. In general, these bimolecular quenching processes may or may not involve diffusional motion of Q and D, depending on how the system is organized and the type of interaction.

Resonance energy transfer is a long range process, which can occur over intermolecular distances much greater than collisional diameters. Such a process occurs as a result of intermolecular dipole-dipole interactions which couple the initial and the final state of the system. A necessary condition for resonance energy transfer is an overlap between the donor's emission spectrum and the quencher's absorption spectrum. Exchange energy transfer and electron transfer are short range processes, occurring only when the donor and the quenching molecules are close enough for the overlapping of their electron clouds. All of these quenching processes exhibit diffusion-controlled quenching.

1. K. STATIC OR COLLISIONAL QUENCHING

There are two basic types of quenching processes: static and collisional. Both types require an interaction between the luminophore and the quencher. Collisional quenching occurs by the quencher diffusing through solution and interacting with luminophore, resulting in a deactivation of the excited state. The emission intensity is reduced because,

in addition to the deactivation pathways available before the presence of quencher, the presence of quencher now adds another deactivation pathway in competition with luminescence. This quenching process is controlled by how fast the quencher can diffuse through solution and collide with the luminophore, and as diffusion is usually a very fast process in solutions, it can be very efficient. During this process the molecules are not chemically altered. Linear Stern-Volmer plots can be obtained using equation 5**,** and it allows for the experimental determination of the quenching rate constant, k_q. Figure 12 illustrates the process of collisional quenching.

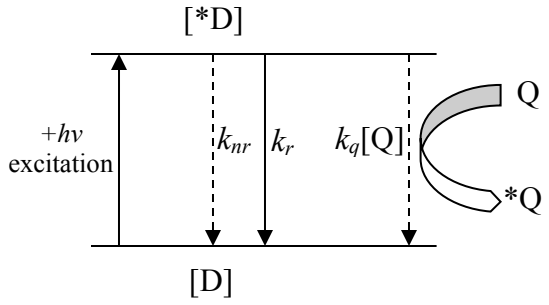

Figure 12. Schematic illustration of collisional quenching.

Static quenching involves the formation of a complex between the luminophore and the quencher that does not rely on diffusion of the excited molecule. In this case of static quenching, quenching molecules Q simply form ground-state complexes with the luminophore D (Figure 13). These complexes can be excited, but are not luminescent. In the case of static quenching the lifetime of the sample will not be reduced since those luminophores which are not complexed will have normal excited state properties and hence are able to emit after excitation.

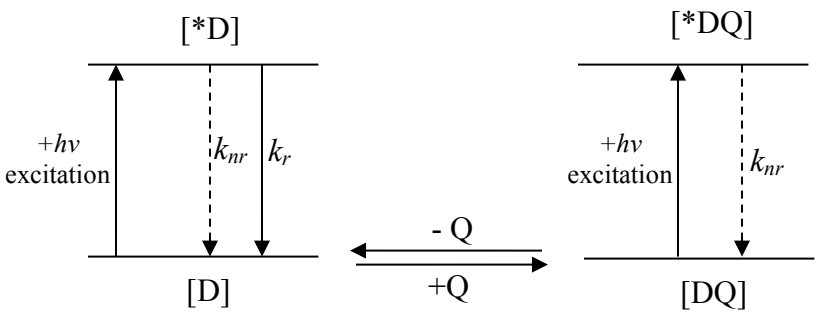

Figure 13. Schematic illustration of static quenching.

The equilibrium between free and complexed luminophores is controlled by an association constant K_s :

$$D + Q \rightarrow DQ \quad (6)$$

$$K_s = [DQ] / [D][Q] \quad (7)$$

$$\text{where, } [DQ] = [D]_o - [D] \quad (8)$$

$$\text{thus, } K_s = [D]_o - [D] / [D][Q] \quad (9)$$

$$[D]_o = [D] + K_s[D][Q] \quad (10)$$

$$\text{dividing by [D] gives,} \quad (11)$$

$$[D]_o/[D] = I_o/I = 1 + K_s[Q] \quad \text{since } I_o=k_L[D]_o \text{ and } I=k_L[D] \quad (12)$$

where [D], [Q] and [DQ] are the concentrations of luminophore, quencher and luminophore-quencher complexes, respectively. $[D]_o$ is the total concentration of the luminophore. k_L is the rate of luminescence, either fluorescence or phosphorescence. The

above modified Stern-Volmer equation, describes the decrease of luminescence intensity with increasing quencher concentration.

Both static and collisional quenching give linear Stern-Volmer plots, thus to distinguish between these two processes temperature and lifetime measurements must be taken under consideration. An increase in temperature leads to an increase in the diffusion constant of quencher and will generally lead to an increase in collisional quenching. In contrast, an increase in temperature will generally lead to a decrease in the association constant between the luminophore and quencher, which will result in an increase in luminescence intensity and a decrease in static quenching. Furthermore, in collisional quenching, lifetime is deceased as intensity luminescence is decrease, whereas, in static quenching, lifetime remains constant as luminescence intensity is decreased (Figure 14).

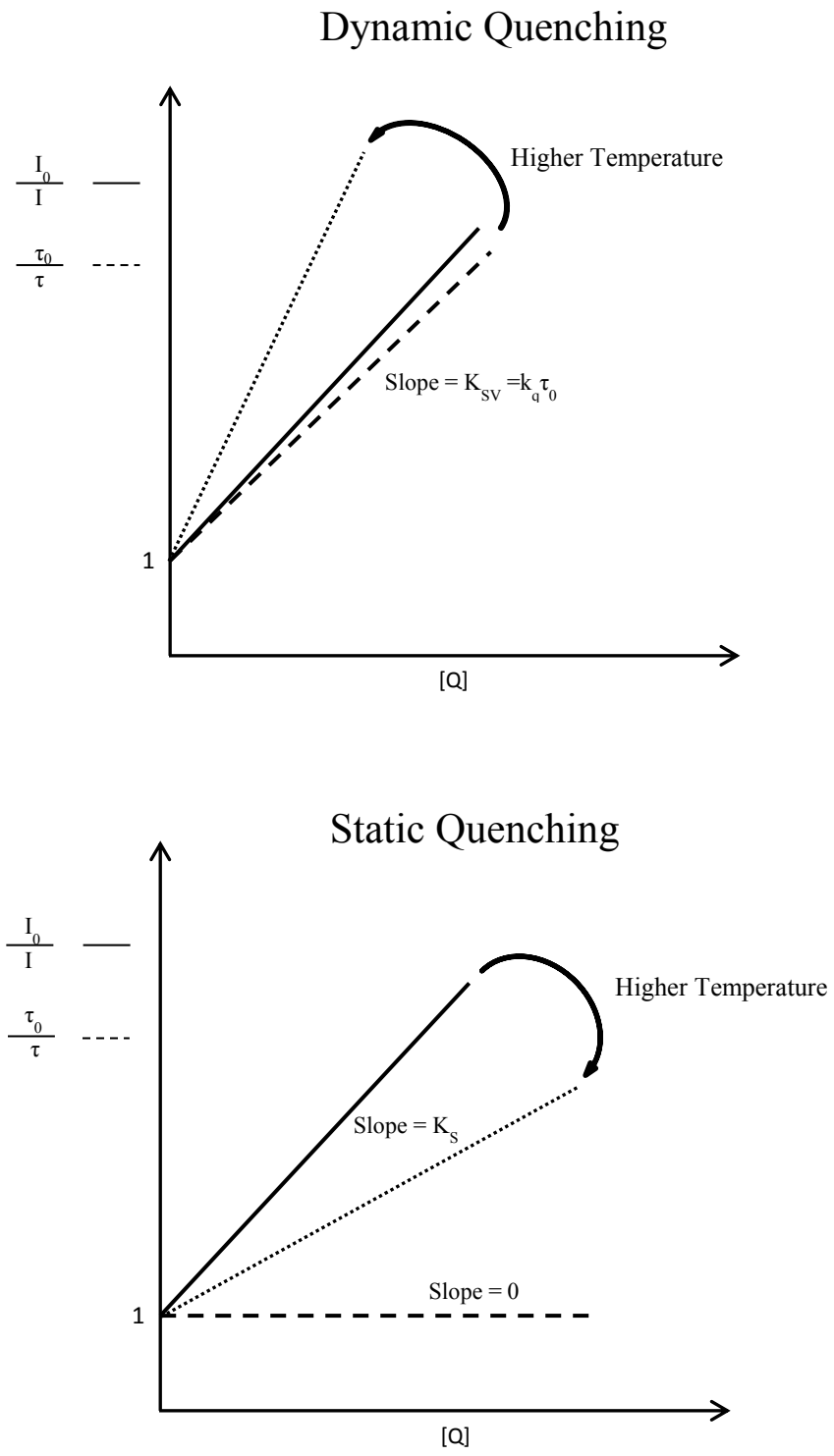

Figure 14. Dynamic Quenching vs. Static Quenching.

1. L. QUANTUM YIELD AND LIFETIME OF LUMINESCENCE

The quantum yield, Φ, is defined as the ratio of the number of fluorescence photons emitted by the sample n_E to the number of photons absorbed n_A.

$$\Phi = \frac{n_E}{n_A} \tag{13}$$

More generally, if the excited state D* directly reached by irradiation gives rise to n primary processes, the quantum yield of a specific process a is given by the ratio of the rate constant of that process to the sum of the rates of all the n processes which deactivate the excited state. Thus, Φ is the ratio of the rate of the radiative transition, k_r, to the rates of all transitions, which in the simplest cases is the sum of the radiative and non-radiative rate, k_{nr}, *i.e.* ($k_r + k_{nr}$), in which the excited state is involved. Therefore, any molecular mechanism leading to a non-radiative depopulation of the excited state reduces the quantum yield. Each quantum yield is typically a number between 0 and 1, and the total of all quantum yields for a particular absorption event should sum to one.

$$\Phi_a = \frac{k_a}{\sum_n k_n} \tag{14}$$

$$\Phi = \frac{k_r}{k_r + k_{nr}} \tag{15}$$

The other important characteristic feature of luminescence is its time response, namely the decay of luminescence intensity following infinitesimally short excitation. The majority of lifetime measurements involve first-order or pseudo first-order kinetic processes. The scheme presented in Figure 15 is a simplified Jablonski diagram, which can be used to explain the basic kinetics of fluorescence.

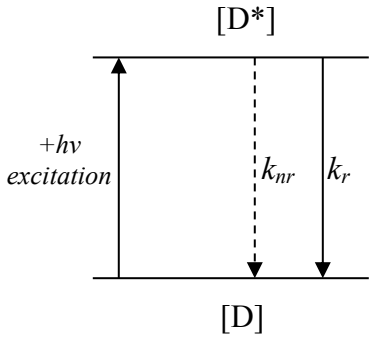

Kinetics:

$$d[D^*]/dt = -(k_r + k_{nr})[D^*] \quad (16)$$

Solution: integration of (1) gives

$$[D^*](t) = D_o^* \exp(-t/\tau_o) \quad (17)$$

Figure 15. Kinetic scheme to illustrate luminescence lifetime and quantum yield.

Figure 15 shows an excitation (*hv)* with a pulse, whose time duration is short in comparison to the excited state lifetime, and the population of the excited molecules [D*] generated at the moment of excitation, t=0, starts to decrease exponentially through the radiative (k_r) and non-radiative (k_{nr}) transitions to the ground state. The characteristic time of this process, τ_o, is defined as the reciprocal of the summation of the deactivation rate constants, radiative and non-radiative.

$$\tau_o = \frac{1}{\sum_n k_n} \quad (18)$$

Thus, from Figure 15.

$$\tau_o = \frac{1}{k_r + k_{nr}} \tag{19}$$

The lifetimes of the lowest spin-allowed (τ (S_1)) and spin-forbidden (τ (T_1)) excited states in Figure 9 are as follows:

$$\tau(S_1) = \frac{1}{k_{ic} + k_f + k_{isc}} \tag{20}$$

$$\tau(T_1) = \frac{1}{k'_{isc} + k_{ph}} \tag{21}$$

The quantum yields of fluorescence emitted by the lowest spin-allowed excited state, S_1, and phosphorescence emitted by the lowest spin-forbidden excited state, T_1, in Figure 9, are given by the following expressions:

$$\Phi_f = \frac{k_f}{k_{ic} + k_f + k_{isc}} \tag{22}$$

$$\Phi_{ph} = \frac{k_{ph} + k_{isc}}{(k_{ph} + k'_{isc}) \text{ x } (k_{ic} + k_f + k_{isc})} \tag{23}$$

1. M. LIGANDS

The bpy, phen and dpp ligands are remarkable for the wide range of formal oxidation states with which they can be associated. Even in a single metal, it is possible to find these ligands associated with formal oxidation states ranging from -2 to +7. The principle interaction between the metal and the ligand is the σ-bonding resulting from an interaction of a vacant d orbital on the metal and the lone pairs on the nitrogen atoms. Associated with this, is the presence of filled π and vacant π* orbitals on the rings; the precise energies of the π and π* orbitals depend on the metal ion, and the matching of energies enables these ligands to act as a π-donor to high oxidation state complexes and a π-acceptor in low oxidation state complexes.

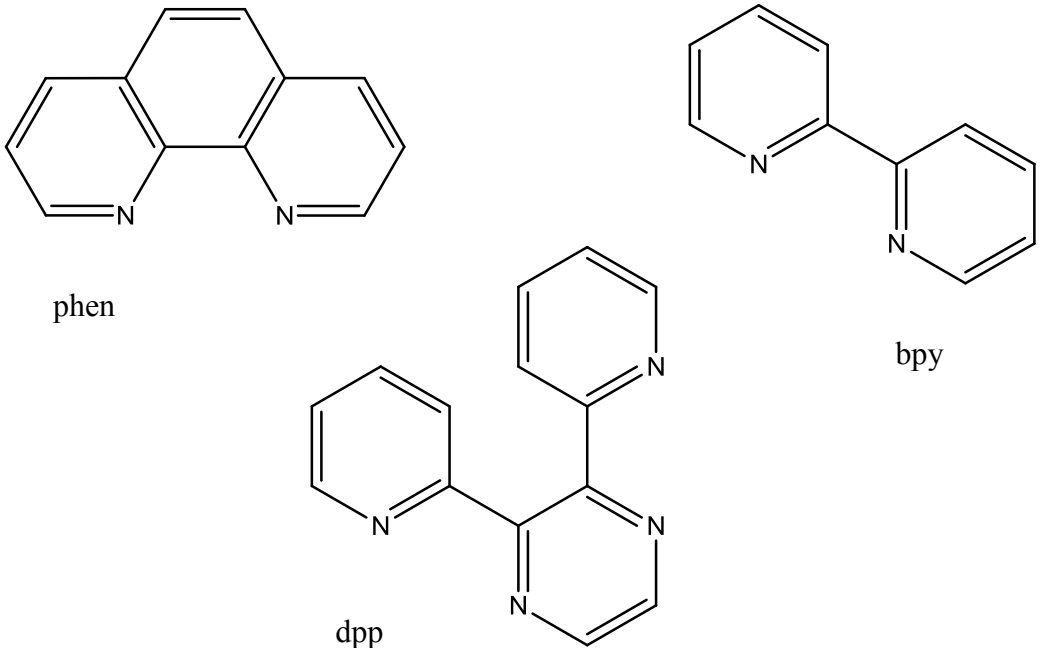

Figure 16. Ligands: 1, 10- Phenanthroline (phen), 2, 3-bis (2-pyridyl) pyrazine (dpp), 2, 2′-Bipyridine (bpy).

CHAPTER 2

2. *EXPERIMENTAL*

2. A. MATERIALS

2. A. 1. SYNTHETIC REAGENTS

1, 10- Phenanthroline monohydrate (phen, $C_{12}H_8N_2 \cdot H_2O$, 198.23 g/mol, Alfa-Aesar, Lot: 10159345), 2, 3-bis (2-pyridyl) pyrazine (dpp, $C_{14}H_{10}N_4$, 234.26 g/mol, Sigma-Aldrich, Lot: 34297LJ), Rhodium (III) hydrate ($RhCl_3 \cdot xH_2O$, 209.26 g/mol, Sigma-Aldrich, Lot: 09207E), 2, 2′-Bipyridine (bpy, $C_{10}H_8N_2$, 156.19 g/mol, Sigma-Aldrich, Lot: 01223DO), Chromium(III) Chloride, Anhydrous ($CrCl_3$,158.35 g/mol, Alfa-Aesar, Lot: H30R051), Zinc Metal Dust (Zn, 65.37 g/mol, Mallinckrodt Chemical Works, Lot: 8681), Potassium Hexafluorophosphate (KPF_6, 184.06 g/mol, Alfa Aesar, Lot: A31Y004), Trifluoromethanesulfonic Acid (triflic acid, CF_3SO_3H, 150.08 g/mol, Alfa-Aesar, Lot: F10X056), Potassium Chloride (KCl, 74.56 g/mol, Fisher Scientific Chemical Company, Lot: 960064), Tetrabutylammonium Hexafluorophosphate (Bu_4NPF_6, $C_{16}H_{36}F_6NP$, 387.43 g/mol, Fluka Chemica, Lot: 2214726), Sodium Acetate ($C_2H_3O_2Na$, 82.03 g/mol, Sigma-Aldrich, Lot: 05418TH), Acetic Acid, Glacial ($C_2H_4O_2$, 60.05 g/mol, Pharmco-Aaper, Lot: PL001508AAG), Hydrazine monohydrochloride (H_2NNH_2•HCl, 68.51 g/mol, Sigma-Aldrich, Lot: 05816KH), Sodium Hydroxide Pellets (NaOH, 40.00 g/mol, J.T. Baker Chemical Co, Lot: 3722-05), Drierite Non-Indicating, Calcium Sulfate Anhydrous ($CaSO_4$, 136.15 g/mol, EMD Chemicals Inc., Lot: TA18AZEMS), N,N-Dimethylformamide, Anhydrous (DMF, C_3H_7NO, 73.09 g/mol, Alfa Aesar, Lot: D12S033) were all used as received.

2. A. 2. SOLVENTS

Ethanol (EtOH, C_2H_6O, 46.07 g/mol, Macron Chemicals, Lot: K30B10), Diethyl Ether ($C_4H_{10}O$, 74.12 g/mol, Fisher Scientific, Lot: 113760), Methanol, Anhydrous (MeOH, CH_4O, 32.04 g/mol, Sigma- Aldrich, Lot: 00236EC), Acetone (C_3H_6O, 58.08 g/mol, Spectrum, Lot: ZC0526), Acetonitrile (C_2H_3N, 41.05 g/mol, Sigma-Aldrich, Lot: 10096EK), Dichloromethane (methylene chloride, CH_2Cl_2, 84.93 g/mol, Sigma-Aldrich, Lot: 99196JJ), Ethylene Glycol ($C_2H_6O_2$, 62.07 g/mol, J.T. Baker Chemical Co, Lot: 9300-03) were all used as received.

2. A. 3. CHROMATOGRAPHIC MATERIALS

DOWEX 1X8 ion-exchange resin (($C_{10}H_{12}.C_{10}H_{10}.C_8H_8.C_3H_9N$)x, Sigma-Aldrich, Batch#: 12129CH), CM Sephadex C-25 (Sigma-Aldrich, Lot: 125K1355), Aluminum Oxide, Activated, Neutral, Brockmann I , STD grade (Al_2O_3,101.96 g/mol, Sigma-Aldrich, lot: S57681-288) were all as received.

2. A. 4. BUFFERS

Buffer solutions (Fisher Scientific Chemical Company) at pH 1 (KCl/HCl, Lot: 074117), pH 2 (KCl/HCl, Lot: 073771), pH 3 ($C_8H_5O_4K$/HCl, Lot: 075391), pH 4 ($C_8H_5O_4K$/HCl, Lot: 092867), pH 5 ($C_8H_5O_4K$/NaOH, Lot: 071202), pH 6 (KH_2PO_4/NaOH, Lot: 075931), pH 7 (KH_2PO_4/NaOH, Lot: 076515), pH 8 (KH_2PO_4/NaOH, Lot: 075930), pH 9 (H_3BO_3/KCl/NaOH, Lot: 092656), and pH 10 (K_2CO_3/K_3BO_3/KOH, Lot: 076519); were used as obtained. Buffer solutions (Ricca

Chemical Company) pH 11 (Na_2HPO_4/NaOH, Lot: 2710252), pH 12 (NaOH/KCl, Lot: 2709201), pH 13 (NaOH/KCl, Lot: 2712345); were used as obtained.

2. B. 1. SYNTHESIS OF [Cr(phen)$_2$Cl$_2$]Cl•2H$_2$O

The synthesis of $[Cr(phen)_2Cl_2]Cl$ was similar to the synthesis reported by Burstall *et al*.[14] Anhydrous chromic chloride (1.5 g, $9.48x10^{-3}$ mol) and 1,10- phenanthroline monohydrate (5.7 g, $2.88x10^{-2}$ mol) in ethanol (50 *mL*) were mixed in a round-bottom flask, fitted with a condenser and heated to boiling after addition of a trace of zinc dust (2 mg) as a catalyst. A vigorous reaction took place, the chromic chloride dissolving to a deep green-brown solution. The mixture was kept at the boiling point for 1 hour and allowed to cool. The dark-red crystals separated and were filtered off and recrystallized using a small quantity of hot water to remove traces of catalytic zinc. This solution was filtered and allowed to crystallize in an ice water bath for approximately 20 minutes; the chromium complex separated as dark brown crystals which were filtered off and dried in an 80ºC oven overnight; after drying the crystals had turned a green color. Yield: 3.9g, $6.60x10^{-3}$ mol, 70%.

2. B. 2. SYNTHESIS OF [Cr(phen)$_2$(CF$_3$SO$_3$)$_2$] (CF$_3$SO$_3$)

$[Cr(phen)_2(CF_3SO_3)_2](CF_3SO_3)$ was prepared by a modification of the literature method.[15, 41] In a three-necked round-bottom flask, trifluoromethanesulfonic acid (10 mL) was slowly added to $[Cr(phen)_2Cl_2]Cl•2H_2O$ (2.1 g, $3.79x10^{-3}$ mol) under an atmosphere of dinitrogen. The resultant reddish brown solution was warmed to and maintained at 90-

100°C and a stream of dinitrogen bubbled through it until the evolution of HCl had ceased. This required approximately 4 hours, at which point the effluent gas no longer produced a white AgCl precipitate when bubbled through an aqueous solution of $AgNO_3$. While maintaining the atmosphere of dinitrogen, the solution was cooled in an ice water bath to 0°C. With vigorous mechanical stirring, anhydrous diethyl ether was added drop wise *via* a syringe and septum until formation of a pink precipitate was complete (~95 mL). The solid was isolated by vacuum filtration, washed three times with 30 mL portions of diethyl ether. Due to the apparent air sensitivity of the complex, the complex was stored in the desiccator under vacuum until required for the next step in the synthesis. The compound was used in the next synthetic step without further purification or characterization. Yield: 2.91g, 3.39×10^{-3}mol (89%). The supernatant was retained and the excess trifluoromethanesulfonic acid was recovered as the sodium salt.[41]

2. B. 3. SYNTHESIS OF [Cr(phen)$_2$dpp] (CF_3SO_3)$_3$

This synthesis was similar to the synthesis reported by Barker *et al*.[16] A complete schematic representation of this synthesis is shown in Figures 17 and 18. A mixture of 0.0436 g (1.86×10^{-4} mol) of dpp and 0.105 g (1.17×10^{-4} mol) of *cis*-$[Cr(phen)_2(CF_3SO_3)_2]CF_3SO_3$ in 55 ml of CH_2Cl_2 was refluxed with stirring for 27 hours. The light brown solid produced during reflux was filtered at room temperature, washed with 50 ml of CH_2Cl_2, then 50 ml of ether and dried under vacuum. Yield: 0.0987 g (75%). C, H, N elemental analysis for $CrC_{41}H_{26}N_8F_9S_3O_9$: C, 43.55; H, 2.30; N, 9.91. Found: C, 43.23; H, 2.27; N, 9.83%.

2. B. 4. SYNTHESIS OF [Cr(phen)$_3$] (CF_3SO_3)$_3$•2H_2O

The synthesis of [Cr(phen)$_3$] (CF_3SO_3)$_3$•2H_2O was similar to the synthesis reported by Barker *et al*.[16] To a 0.145 g (7.24 x 10^{-4} mol) sample of 1,10- phenanthroline monohydrate in 10 ml of dichloromethane was added 0.216 g (2.412 x 10^{-4} mol) of *cis*-[Cr(phen)$_2$(CF_3SO_3)$_2$] (CF_3SO_3). The mixture was refluxed for 4.5 hours, which resulted in a red to yellow solution color change and the formation of a bright yellow precipitate. The product was filtered, washed with 50 ml of diethyl ether, then with 50 ml of dichloromethane, and then with an additional 50 ml of diethyl ether. It was dried in a vacuum oven at 45°C for an hour and then stored in a desiccator. Yield: 0.191 g (1.746x10^{-4} mol, 72%).

2. B. 5. SYNTHESIS OF [Cr(bpy)$_2$$Cl_2$]Cl•2$H_2O$

The synthesis of [Cr(bpy)$_2$$Cl_2$]Cl was similar to the synthesis reported by Burstall *et al*.[14] Anhydrous chromic chloride (1.5 g, 9.48x10^{-3} mol) and 2, 2′-bipyridine (4.7 g, 3.01x10^{-2} mol) in methanol (70 *mL*) were mixed in a 125 mL Erlenmeyer flask and heated to boiling after the addition of a trace of zinc dust (~2 mg) as a catalyst. A vigorous reaction took place, the chromic chloride dissolving to a deep brown solution. The mixture was kept at the boiling point for 15 minutes and allowed to cool to room temperature. Subsequently, the solution was cooled in an ice water bath; green crystals separated and were filtered off. Recrystallization was performed using a small quantity of hot water to remove traces of catalytic zinc. This solution was filtered and the filtrate was allowed to crystallize in an ice water bath for approximately 20 minutes; the

chromium complex separated as olive green colored crystals which were dried in an 80ºC oven overnight. Yield: 4.2 g, 8.29×10^{-3} mol, 87%. This compound was used without any further purification.

2. B. 6. SYNTHESIS OF $[Cr(bpy)_2(CF_3SO_3)_2]$ (CF_3SO_3)

The synthesis of $[Cr(bpy)_2(CF_3SO_3)_2](CF_3SO_3)$ was similar to the synthesis reported by Ryu *et al.*[15] Under a dinitrogen atmosphere in a three-necked round-bottom flask, trifluoromethanesulfonic acid (5 mL) was slowly added to solid cis-$[Cr(bpy)_2Cl_2]Cl \bullet 2H_2O$ (1.1g, 2.17×10^{-3} mol) to give a red-orange solution. Dinitrogen was bubbled through the stirring solution until the evolution of HCl ceased. Periodically the effluent gas was bubbled through a solution of $AgNO_3$ to confirm the evolution of HCl, and to establish completion of the reaction. No further white AgCl precipitate was produced after approximately 25 hours at room temperature. Subsequently the solution was cooled in an ice-bath to 0°C; while maintaining the dinitrogen atmosphere, diethyl ether was added drop wise with vigorous stirring with a stirring bar until the formation of a beige-peach precipitate was complete (*ca.* 210 mL). The solid was isolated by vacuum filtration, washed three times with 30 mL portions of diethyl ether, and dried in a vacuum oven at 100°C for three hours. The dried solid was then placed in desiccator over anhydrous $CaSO_4$. 1.51 g (86%) of the compound was recovered and was used without any further purification. The supernatant was retained and the excess trifluoromethanesulfonic acid was recovered as the sodium salt.[41]

2. B. 7. SYNTHESIS OF [Cr(bpy)$_3$](PF$_6$)$_3$

The synthesis of $[Cr(bpy)_3]^{3+}$ was similar to the synthesis reported by Barker *et al*.[16] A 0.184 g (1.18×10^{-3} mol) sample of 2, 2′-bipyridine was dissolved in 17 ml of CH_3CN in a round-bottom flask, and 0.313 g (3.86×10^{-4} mol) of solid *cis*-$[Cr(bpy)_2(CF_3SO_3)_2]CF_3SO_3$ was added. A condenser was fitted to the round-bottom flask and the solution mixture was refluxed for 25 min, and then evaporated to dryness under a nitrogen gas stream (*ca.*10 hours). The dry solid was extracted via room temperature sonication with 6 ml of water. After filtering off some undissolved material, an aqueous solution of saturated KPF_6 was added and a bright yellow precipitate formed immediately. Recrystallization using a minimum amount of hot water was performed to remove impurities. Yield: 0.256 g, $2.74\text{x}10^{-4}$ mol, 71%.

2. B. 8. SYNTHESIS OF [Cr(bpy)$_2$dpp](CF$_3$SO$_3$)$_3$ and *[Cr(bpy)$_2$dpp](PF$_6$)$_3$*

The synthesis was adapted from Vandiver *et al.* [48] A 0.214 g ($2.64\text{x}10^{-4}$ mol) sample of cis-$[Cr(bpy)_2(CF_3SO_3)_2]CF_3SO_3$ was combined with 0.080 g ($3.43\text{x}10^{-4}$ mol) of dpp, and the mixture was refluxed in 18 mL of anhydrous CH_2Cl_2 solution while stirring for 80 min. After brief sonication, the yellow-brown $[Cr(bpy)_2dpp](CF_3SO_3)_3$ product was filtered at room temperature, and washed with 20 mL of CH_2Cl_2, 60 mL of ether. After suction dried, the yield was 0.201g ($1.92\text{x}10^{-4}$ mol). This initial product was then extracted with sonication into 7.5 mL of water at room temperature, and the solution filtered to remove undissolved material. The product was purified using cation exchange

chromatography on CM Sephadex C-25 with an aqueous 0.5 M NaCl solution as the eluent. The PF_6^- salt was isolated from the eluent by the addition of saturated KPF_6. The product of $[Cr(bpy)_2dpp](PF_6)_3$ was filtered and washed with 1 mL of water, 60 mL of ether, and then suction dried. Yield: 0.179 g, $1.73x10^{-4}$ mol, (66%). C, H, N elemental analysis for $CrC_{34}H_{26}N_8P_3F_{18}$: C, 39.50; H, 2.52; N, 10.83. Found: C, 39.10; H, 2.61; N, 10.54%.

2. B. 9. SYNTHESIS OF [cis-[Rh(bpy)$_2$Cl$_2$][PF$_6$]

This synthesis is modeled after one reported by Amarante *et al.*[10] $RhCl_3 \bullet xH_2O$ (0.200 g, $9.56x10^{-4}$ mol), 2,2′-bipyridine (0.328 g, $2.10x10^{-3}$ mol), 16 mL of ethylene glycol and 0.2 mL of water were placed in a 50 mL double-necked round-bottom flask, fitted with a condenser, and degassed by stirring under dinitrogen for 30 min. The open neck was sealed with a septum. The reaction mixture was heated at 130°C for 20 min under dinitrogen. The solution changed from maroon to yellow-orange. Using a syringe, saturated aqueous KPF_6 (23 mL) was added to the warm solution to precipitate the product. After stirring on ice for 30 min, the resulting pale-yellow solid was vacuum filtered, and rinsed with water followed by three 30 mL portions of diethyl ether. The product was then purified by neutral alumina chromatography using a 1:1 (v/v) acetonitrile/ethanol solvent mixture as the eluent. The first band eluted was the unreacted ligand followed by a second bright yellow band which was the desired product. This purification was carried out in a fume hood to avoid acetonitrile inhalation. The solution was concentrated by rotary evaporation, cooled on ice water for 30 minutes and

approximately 300 mL of diethyl ether was slowly added to induce precipitation, while using vigorous mechanical stirring. The precipitate was again separated by vacuum filtration and washed with diethyl ether. This chromatographic procedure was repeated twice to ensure product purity. The final product was recrystallized from hot ethanol, collected and dried in a vacuum oven at 80°C for three hours to produce 0.537 g ($9.56x10^{-4}$ mol, 89%) of purified pale yellow, microcrystalline product. After drying, it was kept in a desiccator over anhydrous $CaSO_4$.

2. B. 10. SYNTHESIS OF $[Rh(bpy)_2dpp][NO_3]_3$

The synthesis was adapted from Burke *et al*. [11] The synthesis is shown schematically in Figure 19. 0.300 g ($4.75x10^{-4}$ mol) of [cis-$[Rh(bpy)_2Cl_2][PF_6]$ and 0.114g ($4.87x10^{-4}$ mol) of dpp in 25 mL aqueous ethanol (95%) were placed in a 50 mL round-bottom flask, fitted with a condenser, and degassed by stirring under dinitrogen for 30 min. The solution was then heated to reflux for 24 hours at 70°C, while maintaining the dinitrogen atmosphere. The pale pink solution was cooled in an ice water bath for 20 minutes. Saturated aqueous solution of KPF_6 was added drop wise to the solution. An off-white precipitate, which immediately formed, was filtered off, and collected. 30 ml of Dowex 1-X8, a strongly basic ion-exchange resin, was loaded onto a 25 cm chromatography column, washed first with distilled water, and then rinsed with 2.0 liters of 6M sodium nitrate solution until no more Cl^- was detectable in the eluent by testing with a 0.1M solution of $AgNO_3$. The column was finally rinsed several times with distilled water. The precipitate was dissolved in a minimum volume of a 25% acetonitrile/water (v/v)

mixture, charged onto the column, and eluted with the same solvent mixture. To the collected solution an equal volume of 95% ethanol was added to assist in the evaporation of acetonitrile/water by creating an azeotrope of lower boiling point, and the solution is evaporated to dryness using a rotary evaporator. The residue was dissolved in a minimum amount of acetonitrile. Thin layer chromatography was performed to determine which solvents and at which ratio gives the best separation of the components in the mixture. This ratio was determined to be 40:3:1 acetonitrile/water/ethanol by volume. The solution was loaded to a 25 cm chromatography column of neutral alumina and eluted with the aforementioned mixture of solvents. In this purification, the first fraction is faintly yellow and contains any remaining unreacted dpp ligand and excess sodium nitrate, the second yellow fraction is the unreacted starting material ($Rh(bpy)_2(Cl)_2^+$). The third light red fraction, which was the [$Rh(bpy)_2(dpp)^{3+}$] complex, was collected, and the eluent was removed by evaporation. A fourth deep red-colored fraction, which is the bimetallic $[(bpy)_2Rh(dpp)Rh(bpy)_2](NO_3)_6$, was discarded. 0.205g ($2.45x10^{-4}$ mol, 52%) of $[Rh(bpy)_2(dpp)](NO_3)_3$ were recovered. A small amount of the compound was precipitated as a PF_6^- salt and sent for elemental analysis. C, H, N elemental analysis for $C_{34}H_{26}N_8RhF_{18}P_3$: C, 37.62; H, 2.40; N, 10.32. Found: C, 37.59; H, 2.35; N, 10.21%.

2. B. 11. SYNTHESIS OF $[Rh(bpy)_3][PF_6]_3$

This synthesis is similar to the synthesis reported by Gidney *et al.*[13]A mixture of $RhC1_3•xH_20$ (0.209 g, $1x10^{-3}$mol, in 20 mL of H_2O), 2, 2′-bipyridine (0.515 g, $3.3x10^{-3}$ mol, in 10 mL of ethanol), and a catalytic amount of hydrazine monohydrochloride

(0.021 g, $0.3x10^{-3}$ mol) was heated at reflux for 30 minutes. The resulting pale yellow solution was cooled on ice water for 15 minutes and aqueous saturated KPF_6 solution (~35 mL) was added. The fine white crystals that precipitated were removed by vacuum filtration, then washed with 30 mL of water, 30 mL of ethanol, and 45 mL of diethyl ether sequentially, and air-dried overnight. The resulting product was dissolved in a minimum amount of acetonitrile then purified by neutral alumina chromatography using a 1:1 (v/v) acetonitrile/ethanol solvent mixture as the eluent. The first pale yellow band eluted was probably the ($Rh(bpy)_2(Cl)_2^+$) along with unreacted bpy ligand followed by a second band which was the desired product. This purification was carried out in a fume hood to avoid acetonitrile inhalation. The solution was concentrated by rotary evaporation, then cooled in an ice water bath for 30 minutes. While maintaining vigorous mechanical stirring, approximately 160 mL of diethyl ether was slowly added to induce precipitation. The precipitate was again separated by vacuum filtration and washed with diethyl ether. The final product was recrystallized from hot ethanol. The purified white, microcrystalline product was collected and dried in a vacuum oven at 80°C for three hours. 0.725 g ($7.2x10^{-4}$ mol, 72%) of the product were collected and it was kept in a desiccator over anhydrous $CaSO_4$. C, H, N elemental analysis for $C_{30}H_{24}N_6RhF_{18}P_3$: C, 35.78; H, 2.36; N, 8.35. Found: C, 35.74; H, 2.41; N, 8.28%.

2. B. 12. ELEMENTAL ANALYSIS

Chromium and Rhodium complexes were analyzed for carbon, hydrogen and nitrogen composition by Galbraith Laboratories, Inc. Samples of approximately 20 mg were used for the analysis.

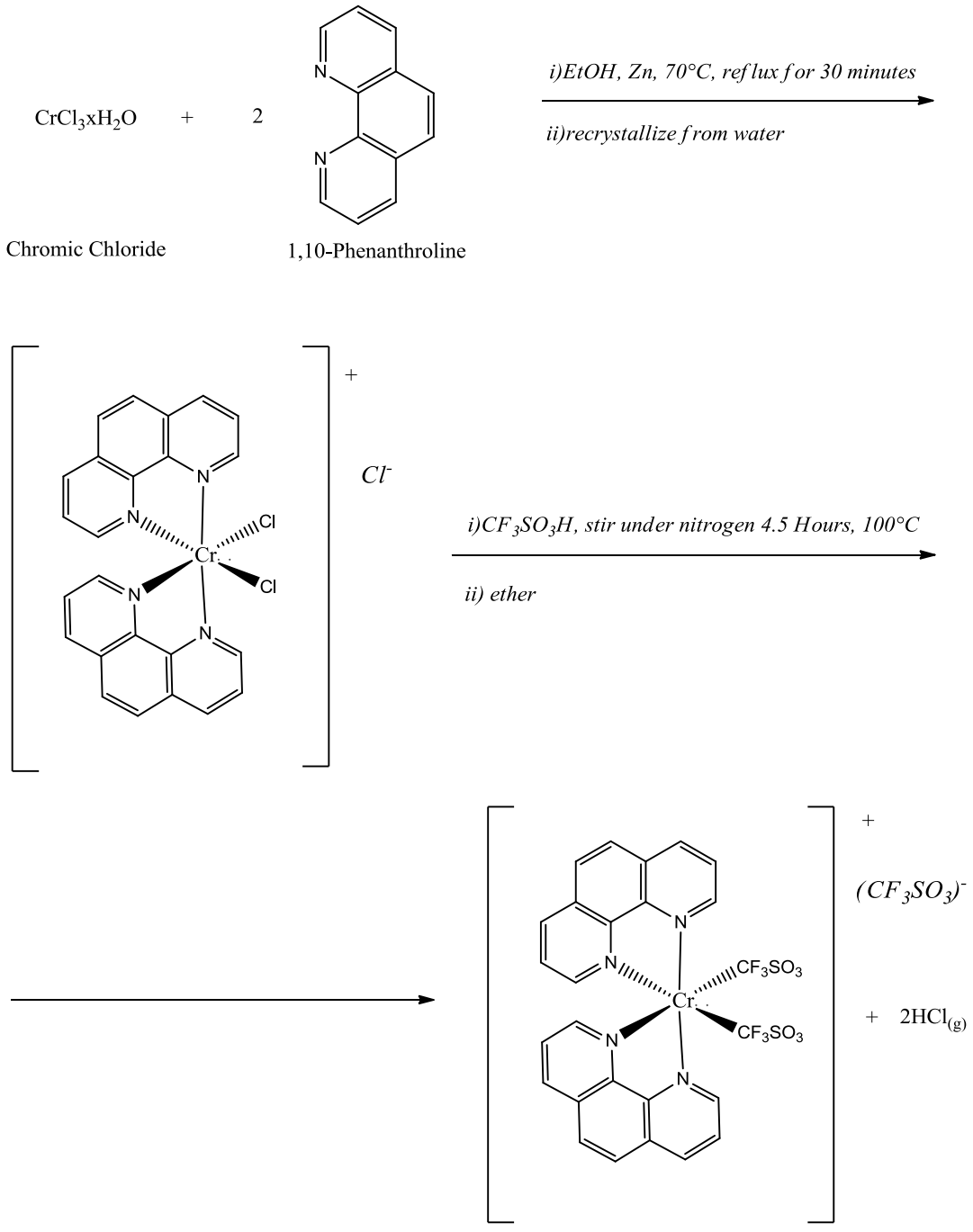

Figure 17. Synthetic scheme of $[Cr(phen)_2(dpp)](PF_6)_3$. Part I.

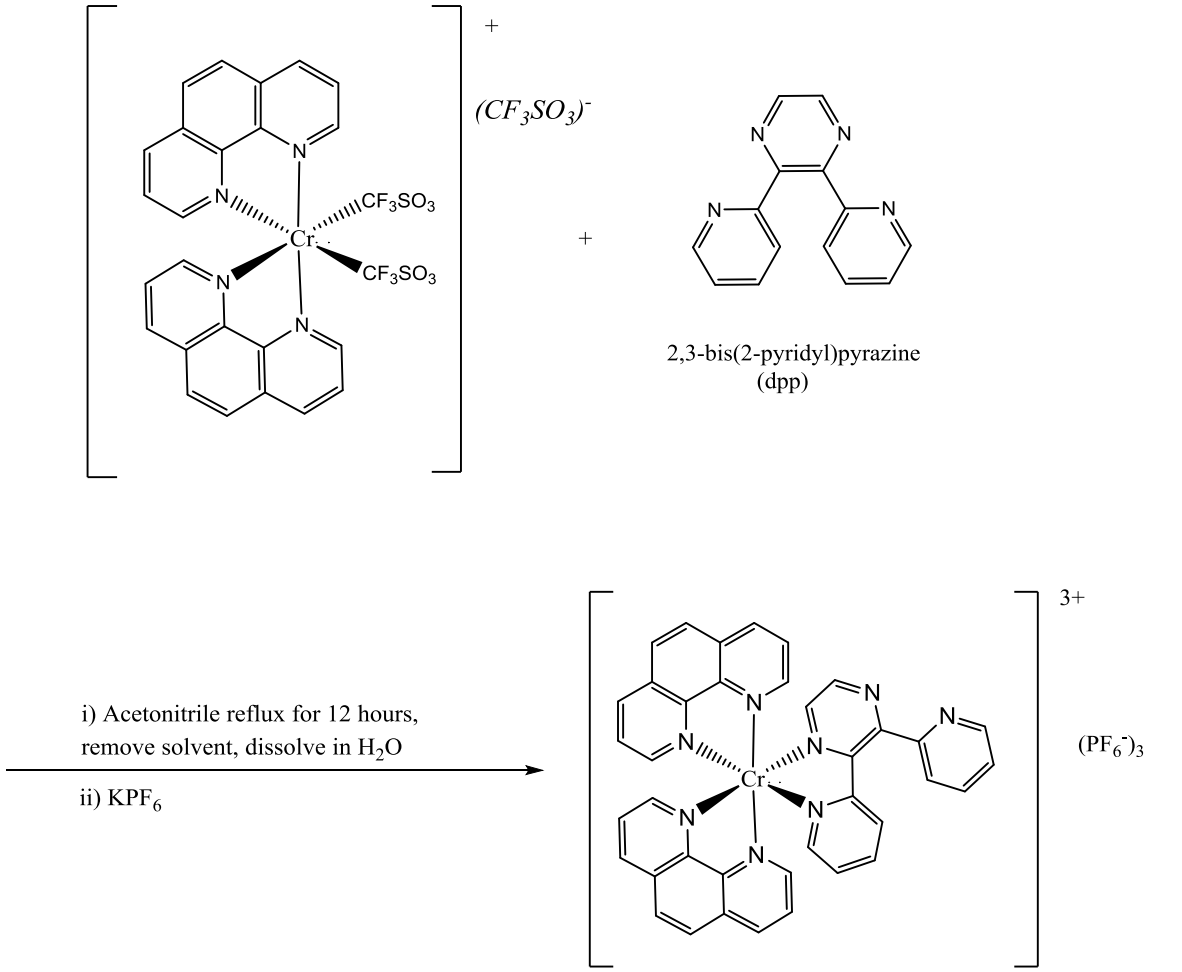

Figure 18. Synthetic scheme of $[Cr(phen)_2(dpp)](PF_6)_3$. Part II.

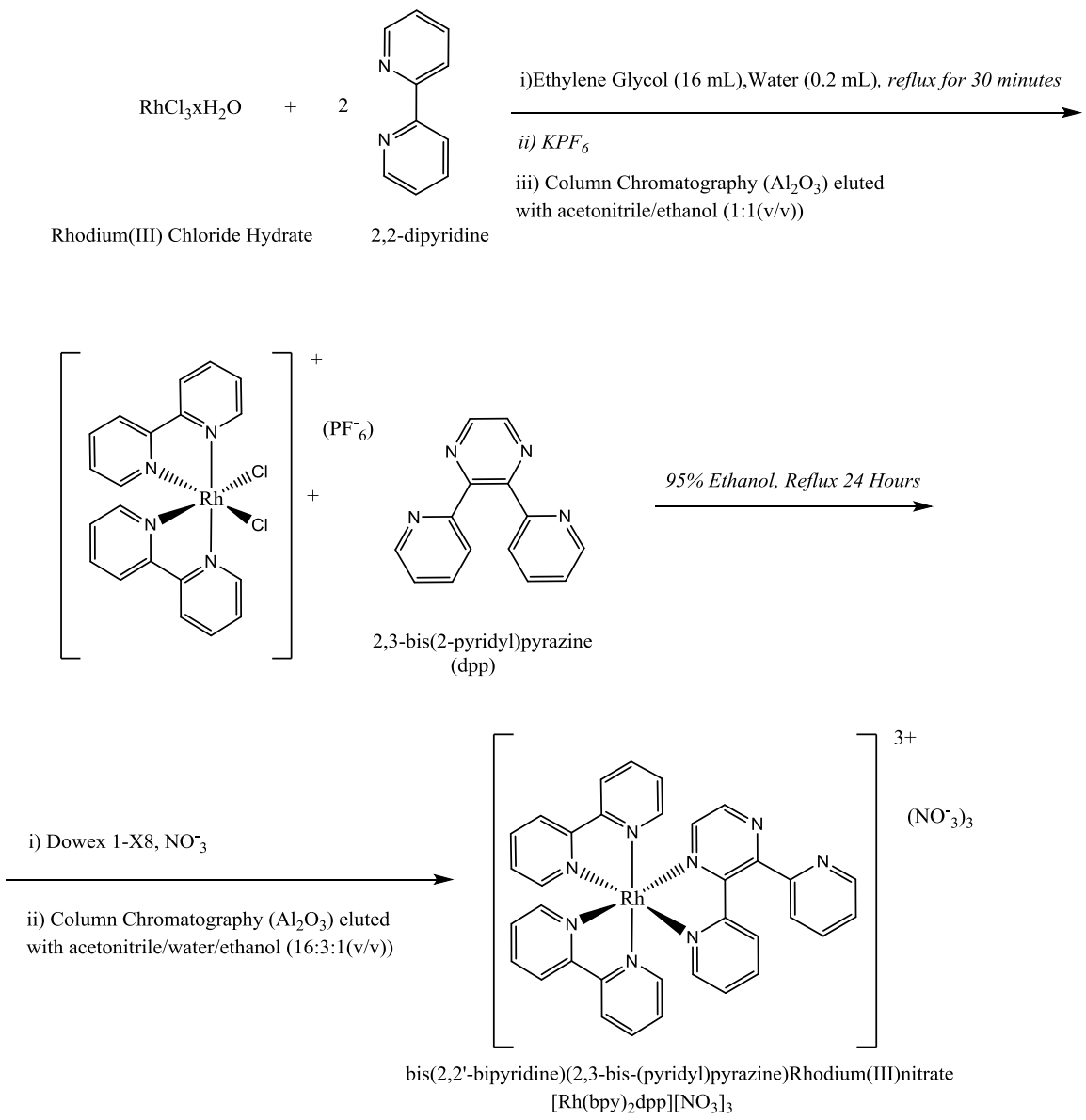

Figure 19. Synthetic scheme of $[Rh(bpy)_2(dpp)](NO_3)_3$

2. C. INSTRUMENTAL

2. C. 1. ELECTRONIC ABSORPTION SPECTROSCOPY

All ultraviolet-visible (UV-VIS) absorption spectra were obtained on a Varian-Cary 5000 UV-Vis-NIR scanning double beam spectrophotometer. Spectral data were exported as .txt files (wavelength, absorbance), and imported into spreadsheet software for further analysis and presentation. The solutions were analyzed using a quartz cuvette with 1 cm path length, customized with a top joint of 14 mm x 20 mm (H.S. Martin Incorporated). All electronic absorption spectra were obtained in room temperature spectrophotometric grade acetonitrile or deionized water.

2. C. 2. LUMINESCECE SPECTROSCOPY

Steady-state emission spectra were collected using standard techniques. All steady-state emission spectra were obtained on a FluoroMax-3 emission spectrometer by Jobin Yvon Horiba. The instrument was controlled with the factory standard FluoroMax software suite. Emission spectra were recorded in room temperature spectroscopic grade acetonitrile and deionized water using a quartz cuvette with 1 cm path length, customized with a top joint of 14 mm x 20 mm (H.S. Martin Incorporated). Low temperature emission spectra were obtained from 4:1 v/v ethanol/methanol solutions immersed in a liquid nitrogen filled finger Dewar flask (77 K) using NMR test tubes (5 mm economy, 7”, 600 MHz, Wilmad LabGlass).

2. C. 3. TIME-RESOLVED EMISSION SPECTROSCOPY

A considerable amount of time was invested in mastering the usage and troubleshooting for various problems of the ICCD time-resolved emission spectrometer, which will hence be described in extensive detail. A diagram of the ICCD camera/spectrograph/laser/timing-generator/computer system used is shown in Figure 20.

2. C. 3. a. OVERVIEW

The laser used for time-resolved experiments, is a Quanta Ray DCR-2A pulsed Nd: YAG (Neodymium doped yttrium aluminum garnet) laser fitted with a HG-2 harmonic generator and an amplifier, giving optimum output at 10Hz. The output pulse has a diameter of 6.4mm, and the linewidth at the fundamental, 1064 nanometers (nm), is less than 1 cm^{-1}. The different laser outputs are listed in Table 1.

TABLE 1. Quanta Ray DCR-2A pulsed Nd: YAG laser outputs.

Wavelength (nm)	Pulse Width (ns)	Energy Stability	Pulse Energy (mJ/pulse), oscillator	Pulse Energy (mJ/pulse), amplifier
1064	8-9	± 1%	300	800
532	6-7	± 3%	150	360
355	5-6	± 3%	60	150
266	4-5	± 5%	20	60

The oscillator begins the firing sequence in the pulsed laser that is followed by the flashlamps, the Q-switch, and then the pulse. A harmonic generator mixes the 1064 nm fundamental to produce the 532 nm, 355 nm, and 265 nm harmonic wavelengths above it.

Both the 532 nm line and the 355 nm line were extensively used throughout this project. The laser can be externally controlled at each stage via inputs at the oscillator, flashlamps, and Q-switched. Both the oscillator and Q-switch are triggered externally in this system. A variable output timed from the Q-switch can be used to trigger a shutter in the camera system (Figure 20). The amplifier was never employed. A system of dichroic high-energy laser mirrors were employed to reflect the 355 nm line (Model BSR-31-1537, CVI Laser Corporation, Lot 64024), and the 532 nm line (Model BSR-51-1525, CVI Laser Corporation, Lot 130938). When the 355 nm line is used, mirror M1 reflects primarily the higher energy 355nm light to another similar mirror M2, which reflects the pulse onto the sample compartment. When the 532 nm line is used, mirror M3 reflects the light to another similar mirror M4, which reflects the pulse also onto the sample compartment (Figure 20). When one exciting wavelength is in use, the other is blocked. Beyond the M 1/3 mirror, a 90° elbow of ½ inch diameter copper tubing serves as a photon trap for the powerful 1064 nm pulse. Both excitation pulses (355 nm or 532 nm) proceed through the sample compartment at close to right angles to the entrance slit of the spectrograph, which is a SpectraPro Model SP-308 (Acton Research Corporation). Since the 532 nm pulse is predominantly used and can damage the camera, a 532 nm holographic notch filter (Model HNF 532.0-1.0, Kaiser Optical Systems, Inc.), F1, is placed before the entrance slit of the spectrograph to block scattering of the laser pulse light from entering.

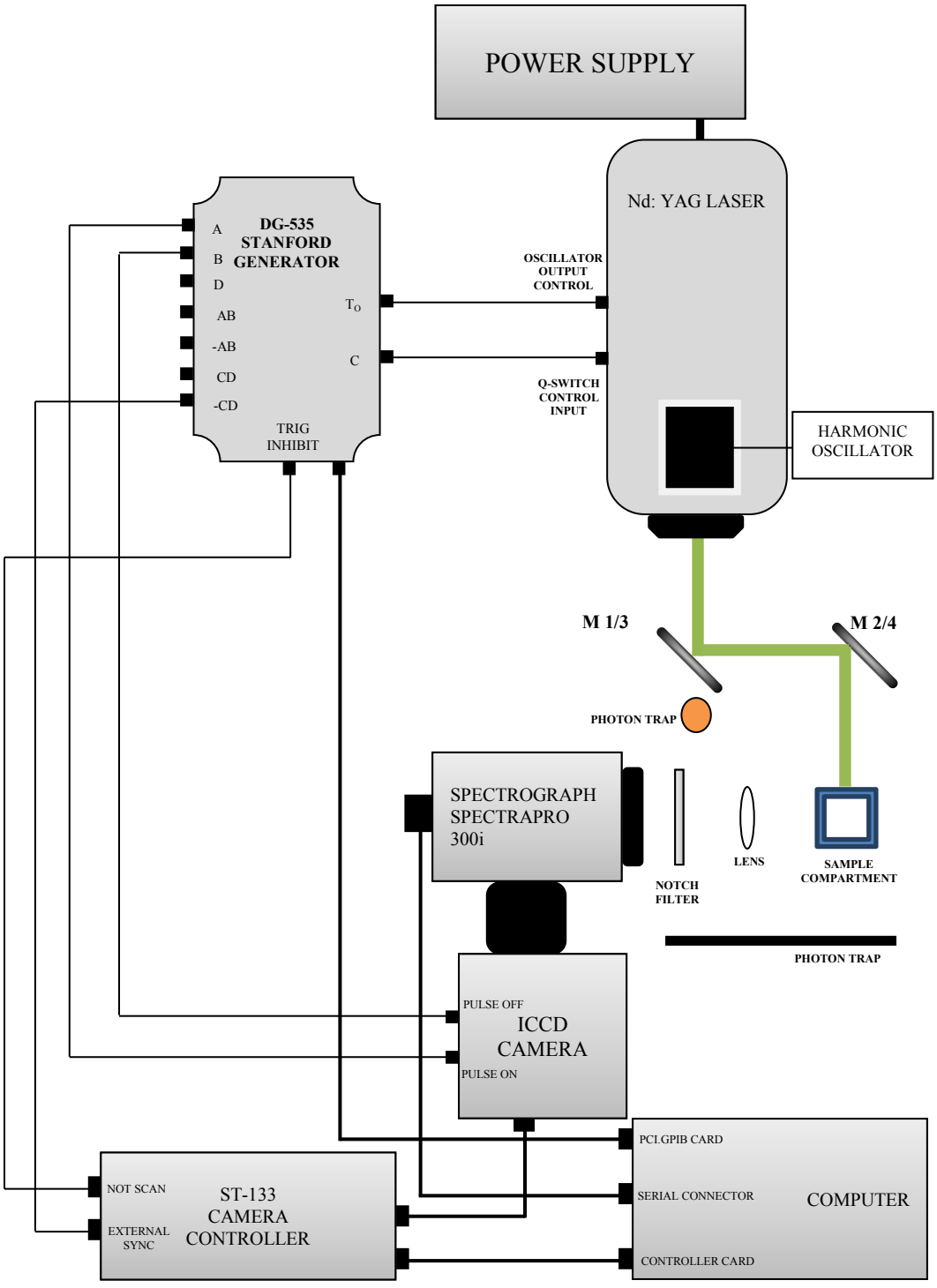

Figure 20. Nd: YAG Laser/ICCD Camera Setup

2. C. 3. b. Nd: YAG LASER THEORY

The term laser is an acronym for **l**ight **a**mplification by **s**timulated **e**mission of **r**adiation. As a consequence of their light-amplifying characteristics, lasers produce spatially narrow, extremely intense beams of light. The process of stimulated emission produces a beam of highly monochromatic and remarkably coherent radiation.

The Nd: YAG laser is a solid state laser. It consists of neodymium (III) ions [Nd^{3+}] in a host crystal of yttrium aluminum garnet. The Nd^{3+} ions provide the electrons for excitation; while the crystalline matrix propagates the energy between ions. This system offers the advantage of being a four-level laser (Figure 22), which makes it much easier to achieve population inversion. The Nd: YAG laser has a very high radiant power at 1064 nm, which is doubled to give an intense line at 532 nm and tripled to give a line at 355nm. The host material in a Nd: YAG laser is a complex crystal of yttrium aluminum garnet with the chemical composition $Y_3AI_5O_{12}$. The YAG crystal has a relatively high thermal conductivity, which improves thermal dissipation in the laser cavity, so continuous wave operation up to a few hundred Watts is possible. When operated in a pulsed mode, high pulsing rates can be achieved, and average powers of up to 1 kW are available. The actual lasant is the Nd^{+3} ions which have been doped into a YAG crystal. The YAG crystal is transparent and colorless. When doped with approximately 1% Nd, the crystal takes on a light blue color.

The essential features of a Nd: YAG Laser are shown in Figure 21. The lasing material is contained within a cylindrical tube with a mirror at each end. One of these mirrors is totally reflecting, while the other one is partial reflecting to enable some of the

light being produced to be utilized. The laser cavity is made to be resonant at the wavelength of the radiation, so that as the radiation traverses the medium the intensity increases through constructive interference. In the excited system, some of the excited species will lose their energy by spontaneous emission. The photons produced in this way can then interact with further excited species to stimulate the emission of more photons, and so on, thus greatly amplifying the radiation. Spontaneous emission seeds the process of stimulated emission. The light amplification can continue until the population inversion is destroyed, so that the light is produced in pulses as population inversions are created and destroyed.

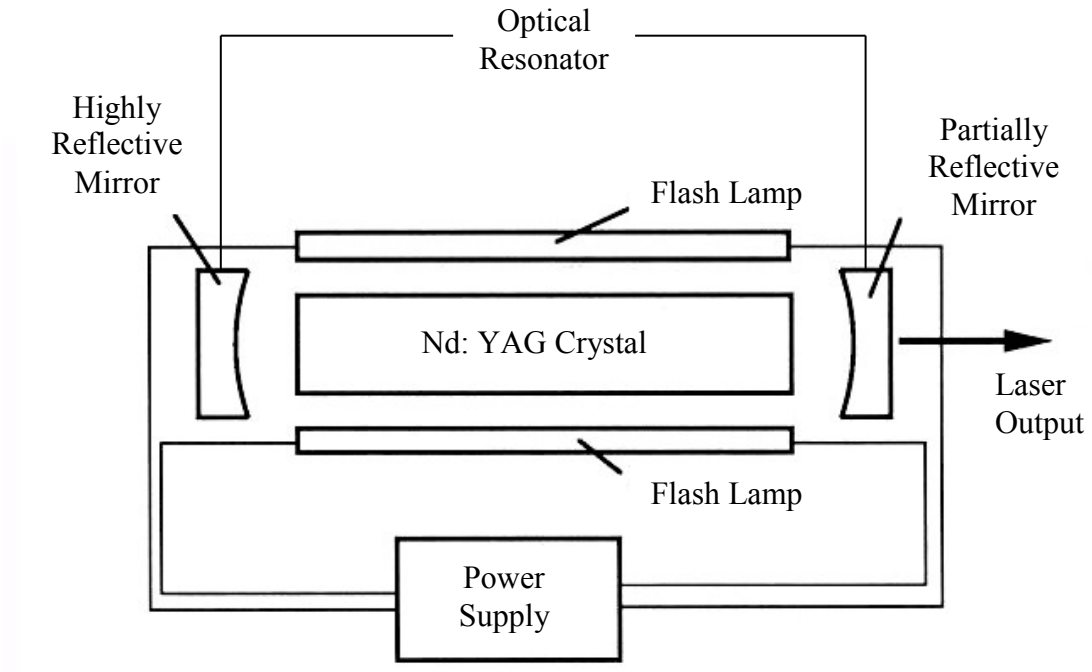

Figure 21. Schematic representation of a Nd: YAG laser.

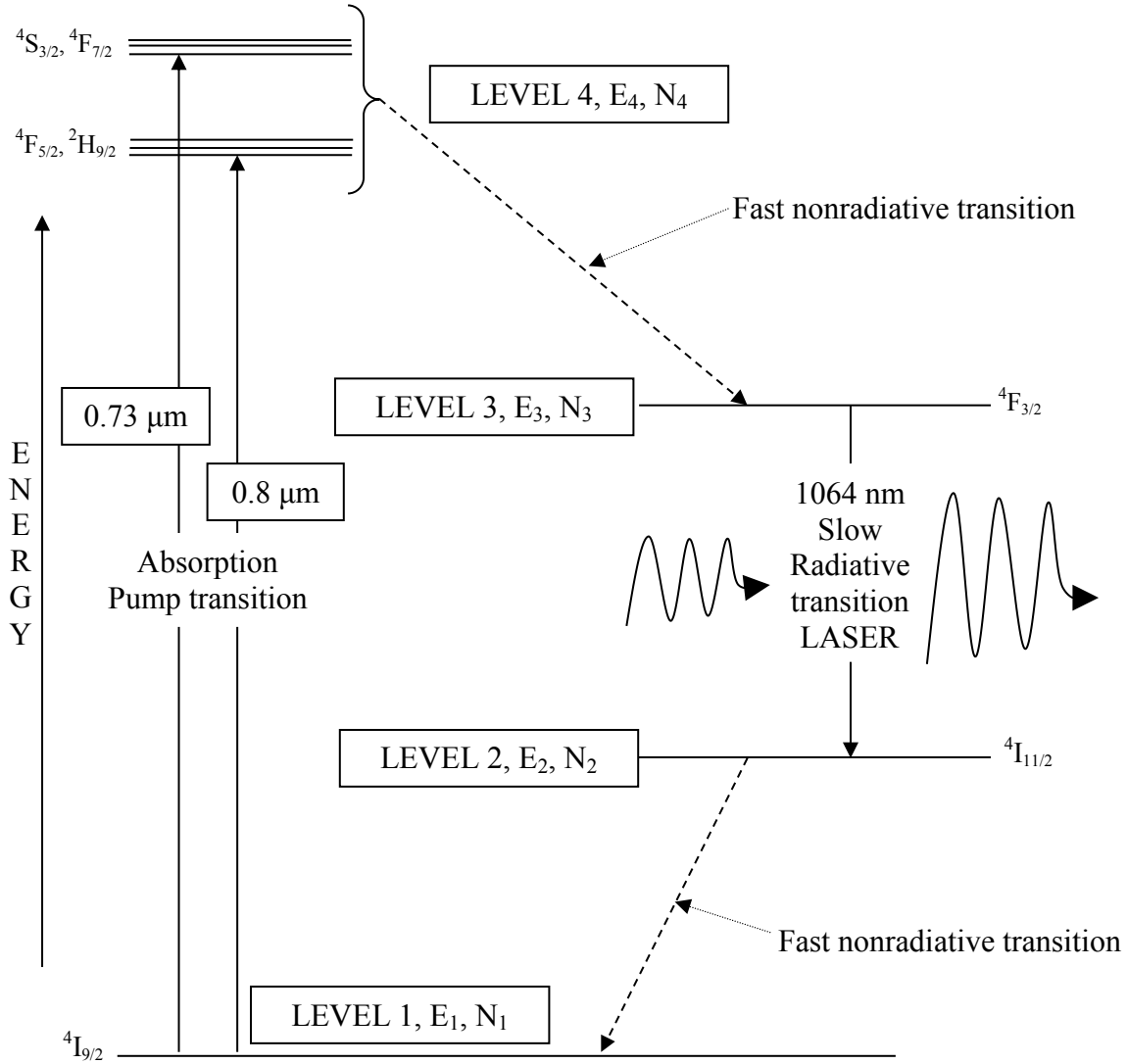

Figure 22. Energy level diagram for four-level laser system.

The energy levels in Figure 22 arise from the three inner-shell 4f electrons of the Nd^{3+} ion, which are effectively screened by eight outer electrons ($5s^2$ and $5p^6$). The crystal field of YAG only weakly influences energy levels, so the Russell-Saunders coupling scheme of atomic physics can be used. In figure 22, there are four energy levels, with energies E_1, E_2, E_3, E_4, and populations N_1, N_2, N_3, N_4, respectively. The energies of each level are such that $E_1 < E_2 < E_3 < E_4$. Nd^{3+} ions have two absorption bands, and excitation is done by optical pumping using flash lamps. In this system, the pumping transition excites the atoms in the ground state (level 1) into the excited state (level 4). From level 4, the atoms again decay by a fast, nonradiative transition into the level 3. Since the lifetime of the laser transition is long compared to that of the nonradiative transition to level 3, a population accumulates in level 3 (*the upper laser level*), which may relax by spontaneous or stimulated emission into level 2 (the *lower laser level*) and the wavelengths of the emitted photons are 1.06 μm. This level likewise has a fast, nonradiative decay into the ground state. The presence of a fast, nonradiative decay transitions result in population of the level 4 being quickly depleted ($N_4 \approx 0$). In this four-level system, any atom in the lower laser level E_2 is also quickly de-excited, leading to a negligible population in that state ($N_2 \approx 0$). This is important, since any appreciable population accumulating in level 3, the upper laser level, will form a population inversion with respect to level 2. That is, as long as $N_3 > 0$, then $N_3 > N_2$ and a population inversion is achieved. Thus optical amplification, and laser operation, can take place.

2. C. 3. c. ICCD CAMERA

The system used in these experiments (Figure 20) employs a Princeton Instruments PI Max ICCD Camera (Roper Scientific) with a Generation II Intensifier (red enhanced). The CCD array is 1024 pixels wide by 256 pixels high, each pixel being 26 μm x 26 μm, with a well capacity of 500 keV. The 18mm wide intensifier, using 1:1 fiber optic coupling, is bonded to the front of the CCD array which is just over 26mm. 4mm on either side of the intensifier is not illuminated. A gain of 6-8 electrons per photon count is possible, and the sensitivity ranging from 1-70 counts depending on the adjustment of the signal gain. The phosphor screen (P43) has a decay time of 2ms. The intensifier gating on/off ratio is $5x10^6$: 1, and can be gated to a window (resolution) of 1.7ns. Jitter is less than 100 ps when the ICCD is cooled to -11°C, which is its normal operating temperature. The camera controller, a Princeton Instruments Model ST-133 (Roper Scientific), houses the analog-to-digital (A/D) converter, reads the temperature of the CCD array, powers the camera, and is the interface by which the computer controls the camera. The A/D converter can handle 1 megapixel per second at 16 bits. The controller reads out 1 pixel per microsecond (1.024ms to read the entire row of 1024 pixels), and it takes 15 microseconds to move to the next row on the CCD. The camera is connected via a serial cable to a high-speed PCI card installed on the computer for data processing and display. Data can be displayed nearly in "real time" with the fast readout, digitizing, and output ability of the controller, coupled with the high-speed serial interface and fast processor of the computer.

2. C. 3. d. COMPUTER AND SOFTWARE

A PC with 1000Mhz AMD Athlon Processor, 256MB Ram, 6GB Hard drive, and installed GPIB/PCI Card and High-Speed 89 Serial PCI Card running Windows XP (SP2) are used to control the instrumentation, set experiment parameters, run experiments, process data, and display data. WinSpec32 software package provided by Princeton Instruments (Roper Scientific) serves as the interface, controlling the spectrograph, timing generator, and camera controller. WinSpec32 allows for display of time-resolved and steady state data, and it contains a functionality that allows to convert and to export data files in ASCII format to be further analyzed using Microsoft's excel software.

2. C. 3. e. SPECTROGRAPH

Incoming light is dispersed by a SpectraPro 300i series (SP-308) spectrograph (Acton Research Corporation). It has a 0.300 meter focal length, f/4 aperture ratio, and focal plane 27mm wide by 14mm high which extends 1.0" outside at the CCD port for ease of mounting an ICCD camera. Manually adjustable micrometers at the entrance slit and two exit slits (chosen by a motorized mirror) can range from 10μm to 3mm. Light passing through the entrance slit is directed by the entrance mirror onto a back mirror and then onto a triple grating turret, which is driven electronically. Three gratings are mounted on the turret: the first with 600 grooves/mm is blazed for optimum reflectivity at 500 nm (600/500 shorthand), the second with 150 grooves/mm is blazed for 500 nm (150/500 shorthand), and the third with 150 grooves/mm is blazed for optimum reflectivity at 800nm (150/800 shorthand). The two gratings with 150 grooves/mm allow display of the

full spectrum of a typical luminescent compound throughout the visible spectrum. The grating with higher resolution allows focusing in on features of a particular emission. Dispersed light from the grating is then reflected off another back mirror onto the motorized exit mirror which reflects the dispersed light across the ICCD. The spectrograph comes with its own software and can be used as a monochromator. The spectrograph is connected via cable from the RS232 interface to the COM2 port on the computer. The WinSpec32 software is able to control the SP-308.

2. C. 3. f. TIMING GENERATOR

The sequence of events and their timing is initiated by the computer software and controlled by a Model-DG535 Digital Delay/Pulse Generator (Stanford Research Systems, Inc.) which has a 5 picosecond (ps) resolution. Four delay outputs (2-3 nanosecond rise time) are available, A,B,C,D, or various combinations (AB, -AB, CD, -CD) in addition to time zero T_0, and all can terminate at 50 Ω or high impedance, and deliver a variety of output levels including transistor-transistor logic (TTL, 0 to 4Vdc, normal or inverted), emitter-coupled logic (ECL, -1.8to -0.8 Vdc, normal or inverted), nuclear instrumentation module (NIM, -0.8 to 0 Vdc, normal or inverted), and variable (ranging from -3Vdc to +4Vdc). This setup employs TTL at 4V, normal, terminating in high impedance load. The generator uses a 25ppm crystal oscillator timebase, and RMS jitter from T_0 to any output is 50ps + delay x 10^{-8}. It is connected via cable from the IEEE488 GPIB (General Purpose Interface Bus) interface to a specially installed GPIB/PCI card from National Instruments. This allows the computer to control the

generator and initiate the timing, quickly advancing the time delay as set forth by the WinSpec 32 experiment acquisition parameters.

2. C. 3. g. TIMING SEQUENCE

A diagram for the timing sequence is provided in Figure 23. When the computer initiates the DG535 (Point 1, Figure 23), the T_0 output pulses the oscillator input on the laser (Point 2, Figure 23). Approximately 210 microseconds after the oscillator fires, the flash lamps of the laser fire (Point 3, Figure 23). The laser Q-switch is externally controlled by the DG535 through output C (Point 4, Figure 23) which is at a fixed time delay of 3.242 milliseconds from T_0 to achieve the maximum intensity of the laser pulse. Since the laser pulse itself appears approximately 50ns after the Q-switch voltage drops to nominal voltage (Point 5, Figure 23), this affords a clear and convenient starting point for data acquisition, and thus the camera is able to capture data starting just before the pulse is delivered to the sample. Therefore, output A of the DG535 which turns on the camera intensifier (Point 6, Figure 23), is set to start at 3.242 ms after T_0, and is advanced forward according to experimental conditions which were usually every 2 ns for Rhodium complexes and 50 μs for Chromium complexes. Output B of the DG535, which turns off the camera intensifier (point 7, Figure 23) occurs at a fixed time delay after Output A. The time between Outputs A and B defines the width of the exposure window, and in turn the time resolution of the camera. As stated above, the intensifier can be gated on and off down to a 1.7 ns window, but 2 ns and 2 ms windows are used for Rhodium complexes and a 50 μs window for Chromium complexes. Output D is timed to output B

(also Point 7, Figure 23) and being connected to the "external sync" input of the camera controller, initiates a readout cycle of the data. Once the controller begins to readout data from the CCD array, it sends a signal through the NOT SCAN output to the INHIBIT input on the timing generator (Point 8, Figure 23) which prevents another timing sequence from occurring until readout is complete. The controller A/D converter digitizes the data and sends it to the computer for processing and display (Point 9, Figure 23).[54]

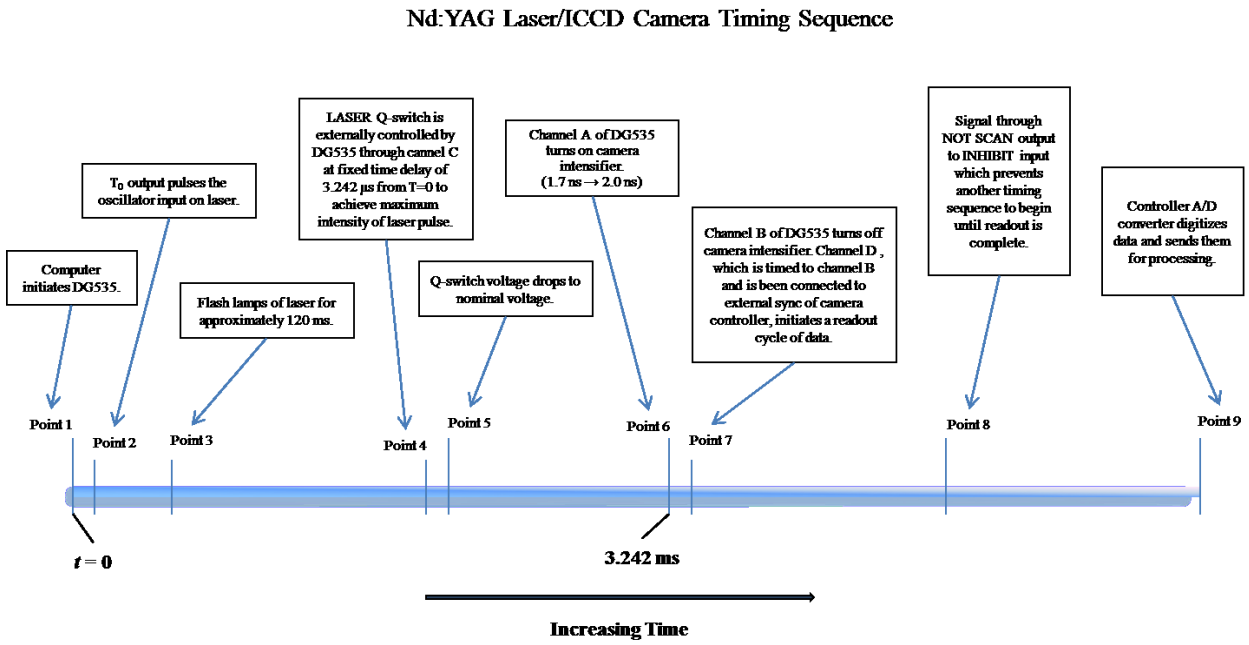

Figure 23. Nd:YAG Laser/ICCD Camera Timing Sequence

2. D. ELECTROCHEMICAL MEASUREMENTS

2. D. a. THEORY AND APPLICATION

Electrochemistry is often used to characterize electroactive transition metal complexes, including those incorporating polypyridine ligands. Cyclic voltammetry (CV) is commonly used to evaluate relative energies of various donor and acceptor orbitals of the species of interest. CV also provides information about electron transfer kinetics at the electrode surface and also details about chemical steps competing with electron transfer processes. Bulk electrolysis provides the number of electrons per molecule per electrochemical step and for evaluating the electronic structure and electronic absorption properties of electrochemical products. Changes to the electronic absorption properties following oxidation or reduction of a light absorbing metal complex are helpful in assigning the nature of electrochemically active orbitals or optical transitions.

2. D. b. CYCLIC VOLTAMMETRY

Cyclic voltammetry is a linear sweep technique that gives important information about the frontier orbitals of an analyte. CV often is a technique performed using a three electrode system that changes the redox state of material at the electrode surface. Figure 24 shows a typical three electrode cell setup for CV measurements. This cell consists of a working electrode, counter electrode, reference electrode, and electrolytic solution. The working electrode's potential is varied linearly with time, while the reference electrode maintains a constant potential. The counter electrode conducts electricity from the signal source to the working electrode. The purpose of the electrolytic solution is to provide ions

to the electrodes during oxidation and reduction.

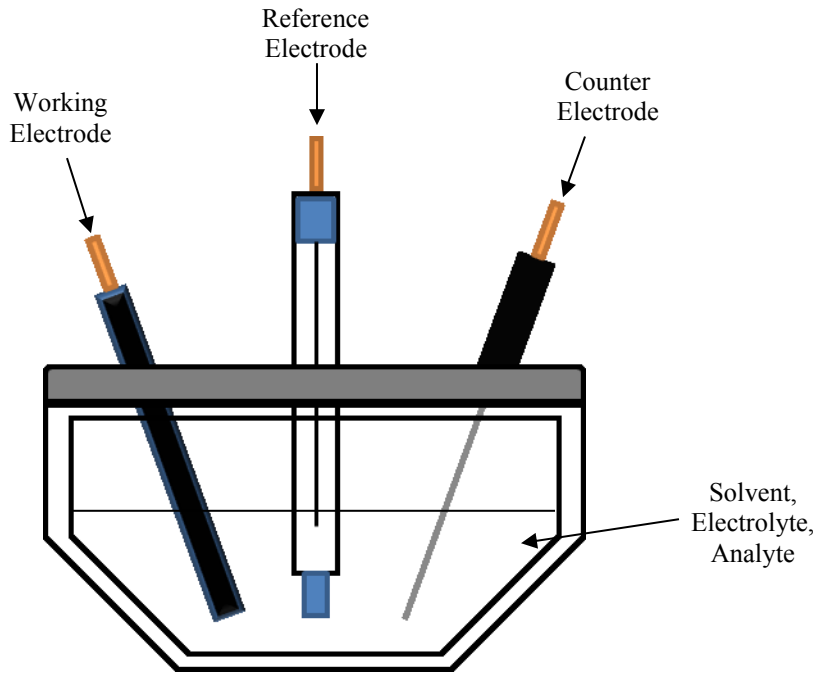

Figure 24. The design of a three electrode, single compartment cell commonly employed in transient electrochemical techniques, including cyclic voltammetry.

The potential of the working electrode is measured against a reference electrode which maintains a constant potential, and the resulting applied potential produces an excitation signal such as that in Figure 25. In the forward scan of figure 25, the potential first scans negatively, starting from a greater potential (a) and ending at a lower potential (d). The potential extreme (d) is call the switching potential, and is the point where the voltage is sufficient enough to have caused an oxidation or reduction of an analyte. The reverse scan occurs from (d) to (g), and is where the potential scans positively. Figure 25 shows a typical reduction occurring from (a) to (d) and an oxidation occurring from (d) to (g). It is important to note that some analytes undergo oxidation first, in which case the

potential would first scan positively. This cycle can be repeated, and the scan rate can be varied. The slope of the excitation signal gives the scan rate used.

In Figure 26, the reduction process occurs from (a) the initial potential to (d) the switching potential. In this region the potential is scanned negatively to cause a reduction. The resulting current is called cathodic current (i_{pc}). The corresponding peak potential occurs at (c), and is called the cathodic peak potential (E_{pc}). The E_{pc} is reached when all of the analyte at the surface of the electrode has been reduced. After the switching potential has been reached (d), the potential scans positively from (d) to (g). This results in anodic current (i_{pa}) and oxidation to occur. The peak potential at (f) is called the anodic peak potential (E_{pa}), and is reached when all of the analyte at the surface of the electrode has been oxidized.

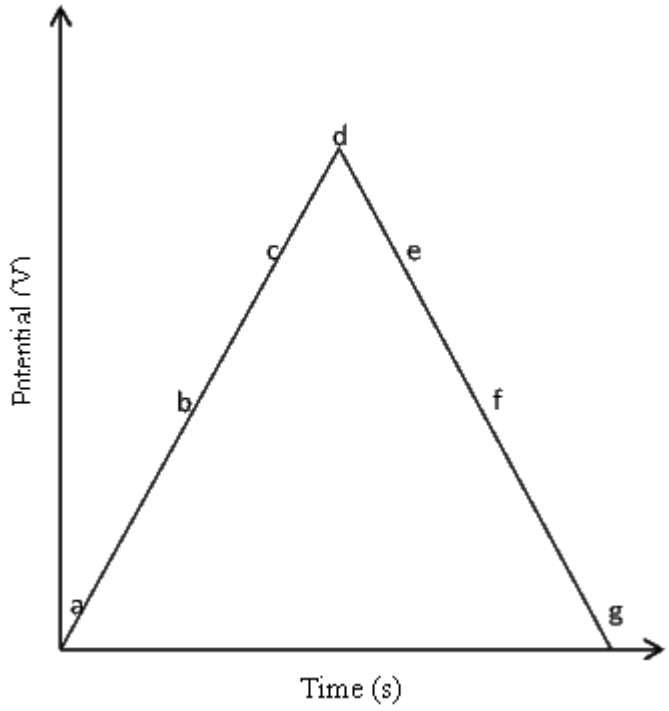

Figure 25. Triangular potential sweep function applied in a two segmented cyclic voltammetry experiment like Figure 26 at a scan rate (*v*) of 100 mV/s.

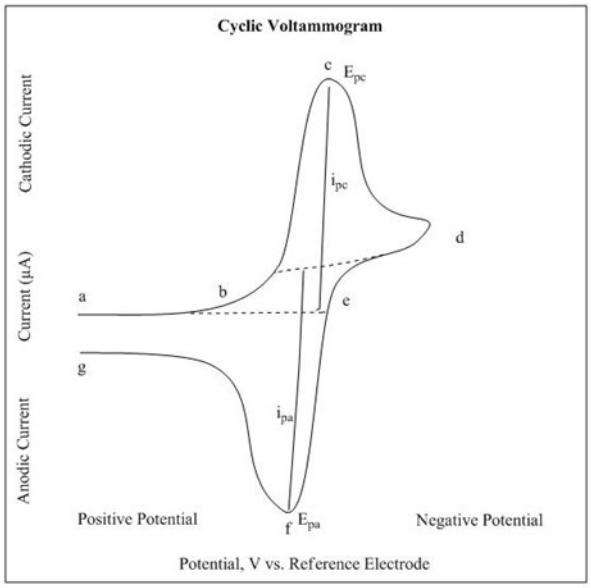

Figure 26. Cyclic voltammogram of an $n = 1$ redox couple that follows reversible Nernstian behavior, where cathodic and anodic peak potentials are denoted by E_{pc} and E_{pa} respectively and the analogous peak currents are i_{pc} and i_{pa}.

For a reversible system, the ratio of the anodic peak current to the cathodic peak current is ideally equal to unity ($i_{pa}/i_{pc} = 1$). Potentials for a reversible system are often reported as the formal reduction potential (E^o) which is the average of the cathodic and anodic peak potentials (E_{pc} and E_{pa}) for a specific couple (24).

$$M^+ + e^- \leftrightarrow M \quad (24)$$

Irreversible electrochemical processes perturb the cyclic voltammogram giving a characteristic current vs. potential curve that is unlike the one shown in Figure 26. In an irreversible cyclic voltammogram point (f) is missing. Chemical reactions following the electron transfer step compete with back electron transfer (25), and for such reactions the ratio i_{pa}/i_{pc} is always less than unity.

$$M^+ + e^- \leftrightarrow M \rightarrow \text{Products} \quad (25)$$

2. D. c. METHOD DEVELOPMENT

All electrochemistry was performed using a CH Instruments 760C electrochemical analyzer employing three-electrode, single chamber cell, Figure 24. Solutions of the rhodium(III)polypyridyl complexes were made by using 0.1 M tetrabutylammonium hexafluorophosphate (Bu_4NPF_6) as the supporting electrolyte in spectrophotometric grade acetonitrile. Solutions of the chromium(III)polypyridyl complexes were made by using 0.1 M potassium chloride (KCl) as the supporting electrolyte in distilled water. The working electrode was a Pt disk, the auxiliary electrode was a Pt wire and potentials were measured against a Ag/AgCl (3M NaCl) reference electrode. Cyclic voltammetry (CV) was typically performed at a scan rate of 100 mV/s. The scan rate dependent electrochemical behavior of some redox processes were examined by changing the potential scan rate (varied from 10 mV/s to 6250 mV/s).

2. E. QUANTUM YIELD DETERMINATIONS

2. E. a. THEORY

Absolute quantum yield determinations require accounting for the total emission from a sample in all directions as compared to the known amount of irradiation. Determining the total amount of emitted photons in a spherical emission is a challenging process requiring specialized equipment and techniques. However, this process can be simplified by comparing a sample of unknown quantum yield to one of known quantum yield.

For determining relative quantum yields, it is important to note that two solutions with the same absorbance at a given wavelength can be expected to absorb the same number

of photons, thus the ratio of their integrated emission spectrum (which is proportional to the total number of emitted photons), is the same as the ratio of their quantum yields, assuming that concentration effects such as self-quenching[13] and inner filter effects[8] are kept to a minimum. If the solutions are in different solvents, the solvent refractive indices must be accounted for. Thus, the selection of the standard is extremely important. The standard and unknown both need to absorb at a common excitation wavelength sufficient to populate the emitting state, and both need to have similar emission profiles with similar emission maxima. This comparative method described by Williams *et al.*[55], is time consuming but it provides high accuracy by comparing the integrated fluorescence intensity and the absorption for unknown sample and standard.

The integrated emission is determined for a series of samples with varying absorption values at the excitation wavelength, such as 0.02, 0.04, 0.06, 0.08, and 0.1. By keeping all absorption values no greater than 0.1, inner filter effects are kept to a minimum. The quantum yield of the unknown, $\Phi_{unknown}$ can be calculated from the following equation:

$$\Phi_{unknown} = \Phi_{standard} \left[\frac{\nabla^2_{unknown}}{\nabla^2_{standard}} \right] \left[\frac{\eta^2_{unknown}}{\eta^2_{standard}} \right] \quad (26)$$

$\Phi_{standard}$ is the quantum yield of the standard, $\nabla_{unknown}$ and $\nabla_{standard}$ are the gradients (slopes) of integrated emission intensity vs. absorbance, and $\eta^2_{unknown}$ and $\eta^2_{standard}$ are the squares of the refractive indices of the respective solvents used at room temperature. The integrated emission intensity vs. absorbance should produce a linear graph with intercept at zero and a slope equal to the gradient.

To determine the quantum yield of Rhodium (III) complex a slightly different method was used. This method was developed by Demas and Crosby.[28] The integrated emission of the $[Rh(bpy)_2dpp]^{3+}$ complex was compared relative to that of the standard $[Rh(bpy)_2Cl_2]^{+}$ according to the eq.27. Both measurements were made back to back.

$$\Phi_{unknown} = \Phi_{standard} (I_{unknown} / A_{unknown}) (A_{standard} / I_{standard}) (\eta_{unknown} / \eta_{standard})^2 \qquad (27)$$

In this expression, $\Phi_{unknown}$ and $\Phi_{standard}$ are the emission quantum yields of the unknown and standard, respectively, under the conditions of the measurement. The quantities $I_{unknown}$ and $I_{standard}$ are the integrated emission intensities of the unknown and the standard, respectively. The quantities $A_{unknown}$ and $A_{standard}$ are the absorbances of the unknown and the standard, respectively, at the excitation wavelength. Care was taken to ensure that these are both close to 0.1. Finally $\eta_{unknown}$ and $\eta_{standard}$ are the indices of refraction of the unknown and the standard solution, respectively. Since the same solvent was used in both measurements, the last term in eq. 27 can be ignored. For these measurements, absorption spectra were recorded before and after the emission measurements to ensure that the measurements were not biased by a photo induced change in the complex.

2. E. b. METHOD DEVELOPMENT

$[Cr(phen)_3](CF_3SO_3)_3$ and $[Cr(phen)_2dpp](CF_3SO_3)_3$ were dissolved in distilled water, to varying concentrations leading to absorptions at the excitation wavelengths ranging from 0.02 to 0.10 in order to avoid inner-filter effects. All solutions were deareated by bubbling with Argon gas for 5 minutes. Since $[Rh(bpy)_2Cl_2](PF_6)$ is not emissive at room

temperature, both $[Rh(bpy)_2Cl_2](PF_6)$ and $[Rh(bpy)_2dpp](PF_6)_3$ were dissolved in ethanol/methanol mixture (4:1 by volume) and their emissions were recorded at 77K. The steady-state emission spectra were recorded on the FluoroMax-3 spectrometer, while absorption spectra were obtained using the Varian-Cary 5000. The excitation wavelength for the Rhodium complexes was set to 319 nm, whereas for the Chromium complexes the excitation wavelength was set to 400 nm. The areas under the steady state emission curves were calculated using the built-in area calculator functions in the software program of the instrument. Relative quantum yields $[Cr(phen)_2dpp](CF_3SO_3)_3$ were obtained by direct comparison of the gradients (slopes) of the emission vs. absorption plots (*vide infra*).

2. F. BUFFER TITRATIONS

Stock solutions of $[Cr(phen)_2(dpp)]^{3+}$, $[Cr(bpy)_2(dpp)]^{3+}$ and $[Rh(bpy)_2(dpp)]^{3+}$ in water were prepared to an approximate concentration of 10^{-5} M. Solution were made by diluting the stock solutions of each complex using 5 mL volumetric flasks with buffers solutions ranging from pH 1 to pH14. The ratio of buffer solution to complex stock solution was 4:1 by volume. Argon gas was bubbled through all solutions for 5 minutes. The ICCD camera was used to obtain time-resolved (355 nm excitation wavelength) emission spectra and the steady-state emission data were obtained by the FluoroMax-3 emission spectrometer using various excitation wavelengths (*vide infra*). In the case of steady state emissions, any emission from blank buffer solutions was obtained and subtracted.

CHAPTER 3

3. RESULTS

3. A. Characterization of [Cr(phen)$_2$(dpp)](PF$_6$)$_3$ and [Cr(bpy)$_2$(dpp)](PF$_6$)$_3$

3. A.1. Electronic Spectroscopy of [Cr(phen)$_2$(dpp)](PF$_6$)$_3$

The electronic spectrum of $[Cr(phen)_2(dpp)]^{3+}$ appear in Figures 27 and 28. Figure 28 displays the absorption spectrum of the chromium(III) complex only between wavelengths 370-500 nm using a more concentrated sample in order to enhance the Laporte forbidden but spin-allowed metal-centered d-d transitions. The UV-Vis spectra of $[Cr(phen)_2(dpp)]^{3+}$ show the characteristic absorption features previously observed for tris(polypyridyl)chromium(III) complexes.[28]

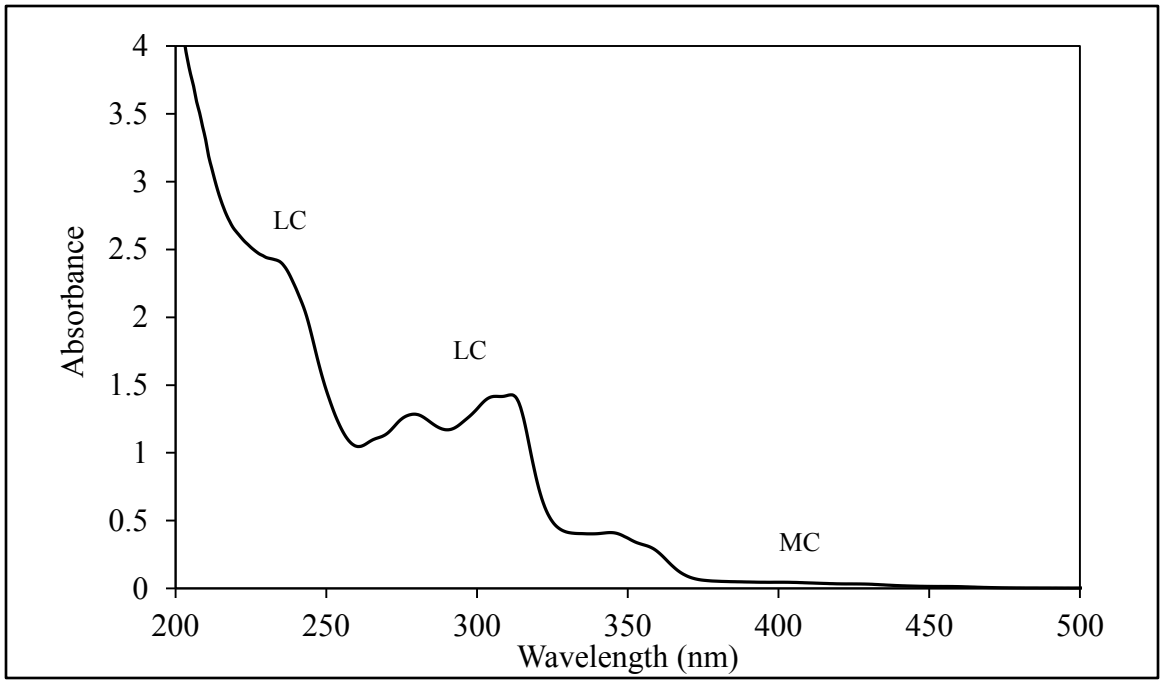

Figure 27. Absorption spectrum of 7.76 x 10^{-5} M $[Cr(phen)_2(dpp)]^{3+}$ in Water (r.t.).

Assuming an octahedral microsymmetry for $[Cr(phen)_2(dpp)]^{3+}$, the absorption spectrum consists of three spin-allowed quartet bands: $^4A_{2g} \rightarrow {}^4T_{1g}$, $^4A_{2g} \rightarrow {}^4T_{1g}$ and $^4A_{2g} \rightarrow {}^4T_{2g}$ (refer to Figure 28). The molar extinction coefficients of these three d-d transitions are 1370, 995, 386 $M^{-1}cm^{-1}$ respectively. The lowest energy band ($^4A_{2g} \rightarrow {}^4T_{2g}$) gives the value of the ligand field parameter Δ. Another feature of the absorption spectra shown in Figure 27 are the intense ligand-centered π→π* transitions observed in the UV range; the lowest energy absorption transition at ~363 nm has a molar extinction coefficient of 3230 $M^{-1}cm^{-1}$, which is at the lower range for a symmetry allowed electronic transition.

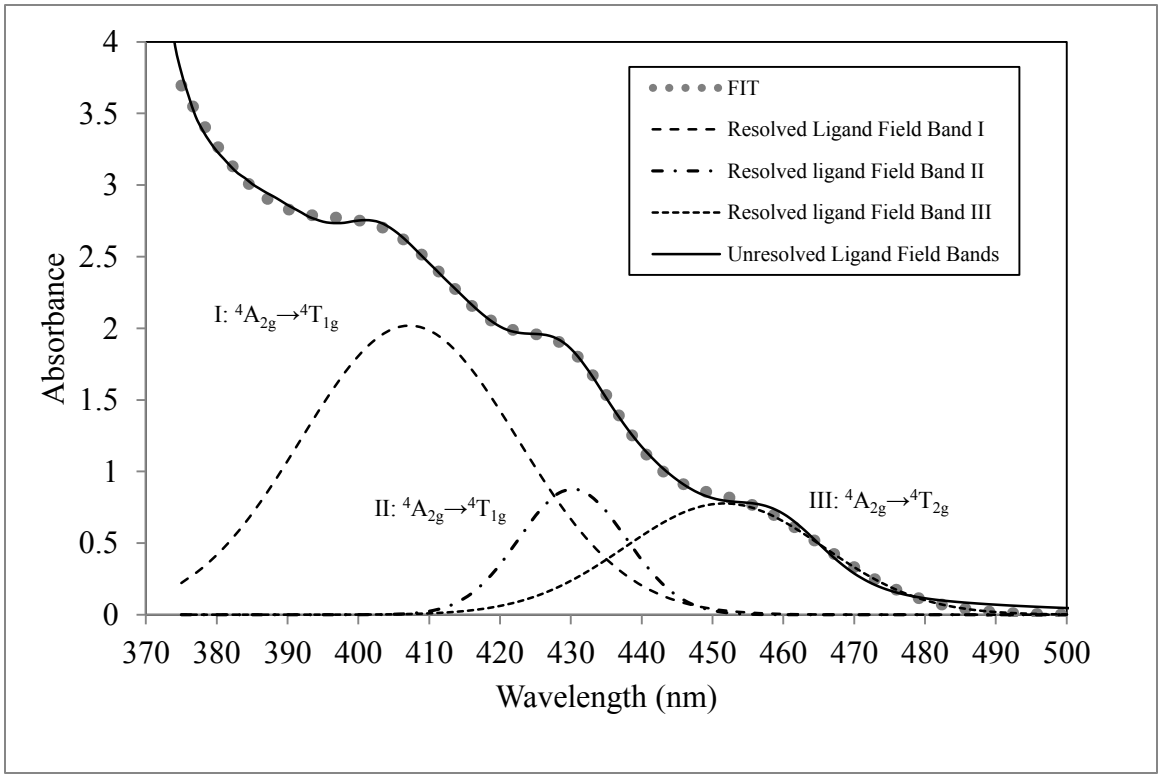

Figure 28. Absorption spectrum of 2.01x 10^{-3} M $[Cr(phen)_2(dpp)]^{3+}$ in Water (r.t.).

The Cr(III) complex yields a narrow phosphorescence emission ($^2E_g \rightarrow {}^4A_{2g}$) and a weak shoulder fluorescence ($^4T_{2g} \rightarrow {}^4A_{2g}$) , with a wavelength maxima at 728 nm and 696 nm, respectively, in water at room temperature (Figure 30). Both the dominant phosphorescence and the weak fluorescence are not wavelength dependent: excitation throughout the d-d region consistently results in the 728 nm and 696 nm emissions. The excitation spectrum shown in Figure 29 confirms that the emissions arise solely from the lower energy d-d transitions, with maximal excitation occurring at 400 nm, which corresponds to the $^4A_{2g} \rightarrow {}^4T_{2g}$ ligand field transition. Its assignment is thus metal centered d-d. Another prominent feature shown in the excitation spectrum of Figure 29 is the overtone at 364 nm of the 728 nm excitation wavelength.

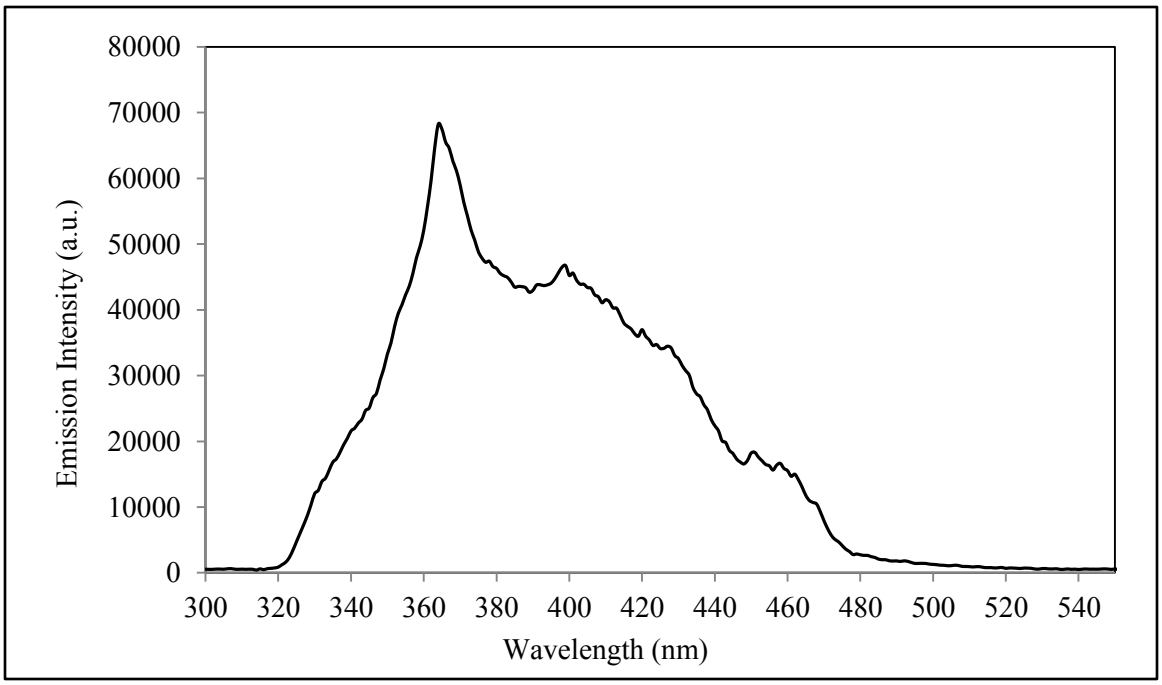

Figure 29. Excitation spectrum $[Cr(phen)_2(dpp)]^{3+}$ in Water (r.t.), monitored at 728 nm shows at maximum at 400 nm.

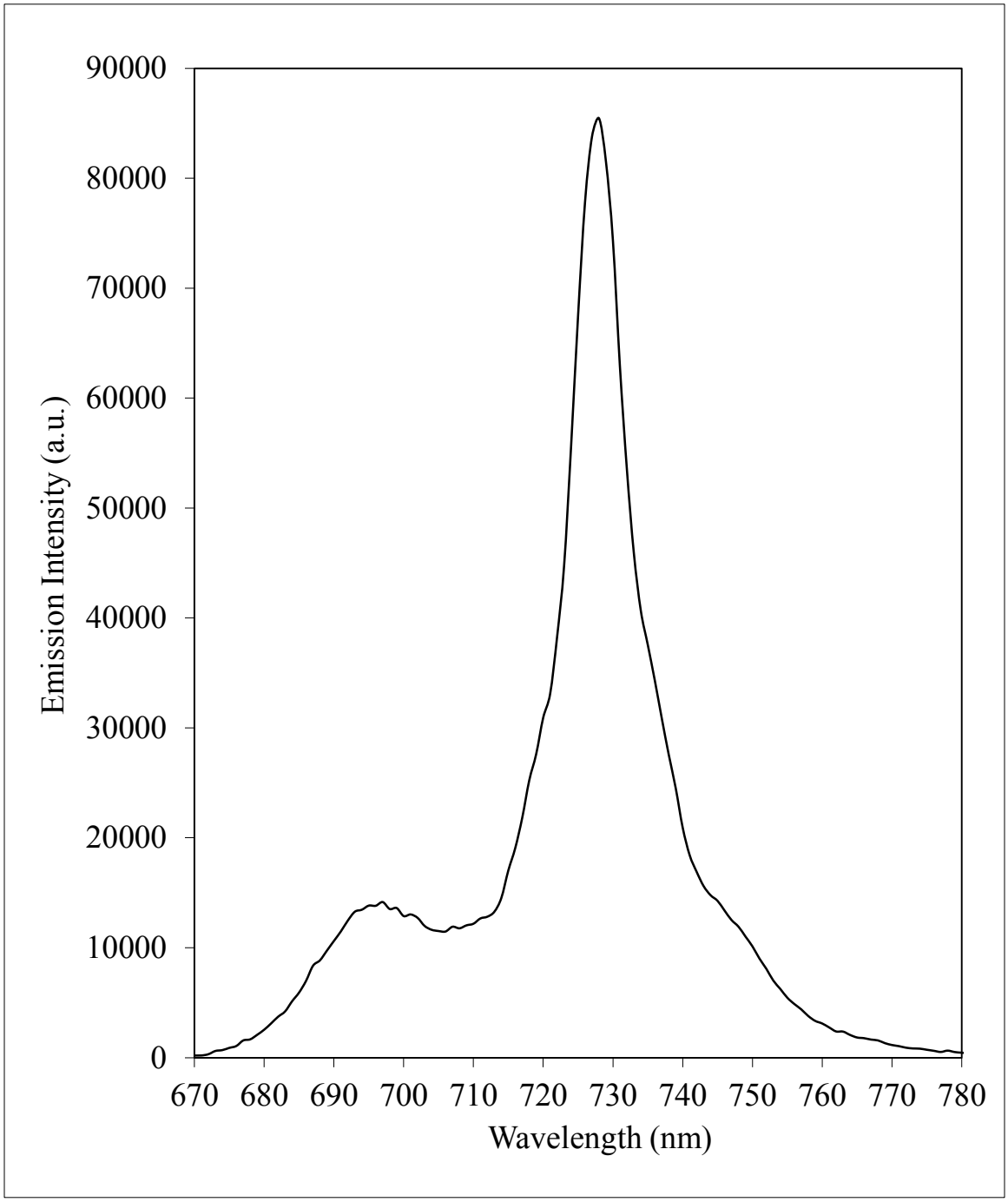

Figure 30. Emission of 7.76 x 10^{-5} M $[Cr(phen)_2(dpp)]^{3+}$ in Water (r.t.). Excitation wavelength 400 nm.

3. A.2. Time Resolved emission Spectroscopy of [Cr(phen)$_2$dpp](PF$_6$)$_3$

The time-resolved spectrum of $[Cr(phen)_2(dpp)]^{3+}$ was examined using the ICCD camera system described above. The full time-resolved three-dimensional spectrum is shown in Figure 31. The trace at the maximum emission intensity (728 nm) going from time zero (T_o) onwards is shown in Figure 32, which includes the grow-in of the emission. This grow-in is arguably only a function of the pulse profile, which has a finite rise and decay profile. Fitting just the decay portion, using IGOR software and the Equation (28), led to a single exponential decay with a lifetime of 87 ± 1 μs.

$$y = y_0 + A \exp[-(x-x_0)/\tau] \quad (28)$$

In equation 28, A is the pre-exponential factor at a specific wavelength and τ is the lifetime. Within overall experimental error, these lifetimes are essentially independent of wavelength. Fitting the decay of the phosphorescence at various wavelengths (710 nm – 750 nm) leads to the same lifetime.

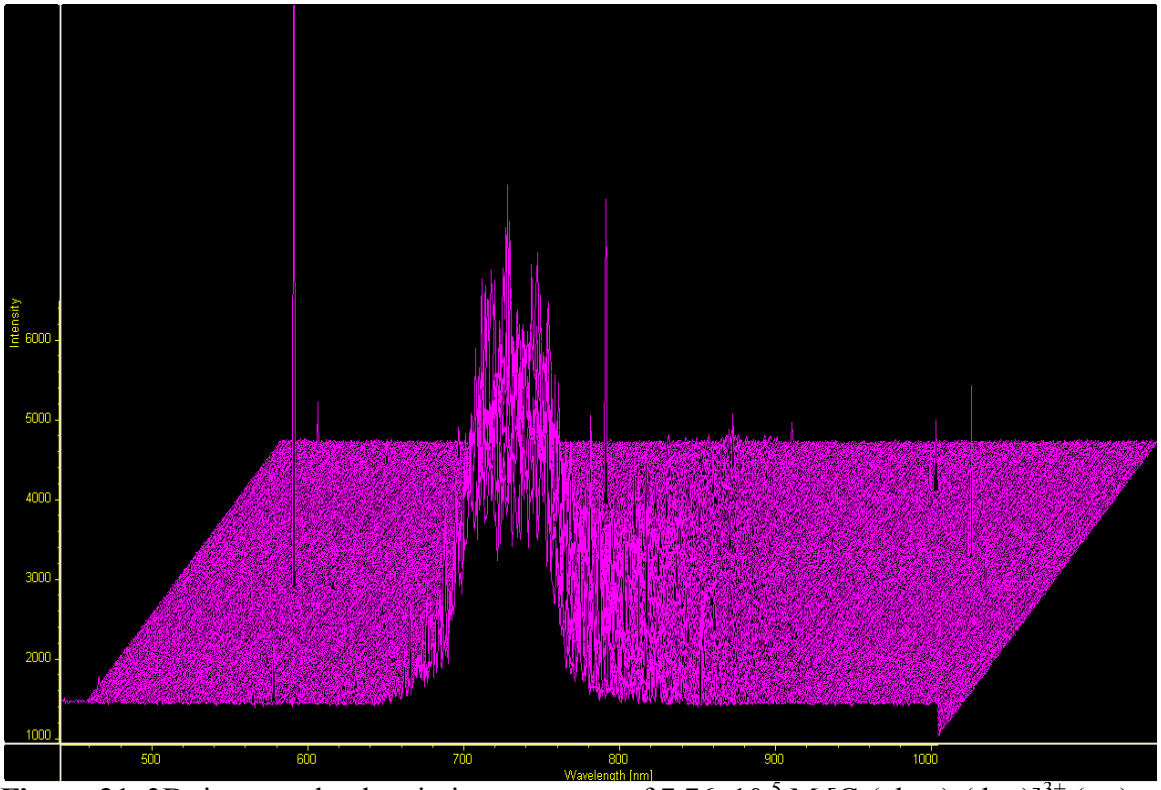

Figure 31. 3D time-resolved emission spectrum of 7.76×10^{-5} M $[Cr(phen)_2(dpp)]^{3+}$ (r.t.).

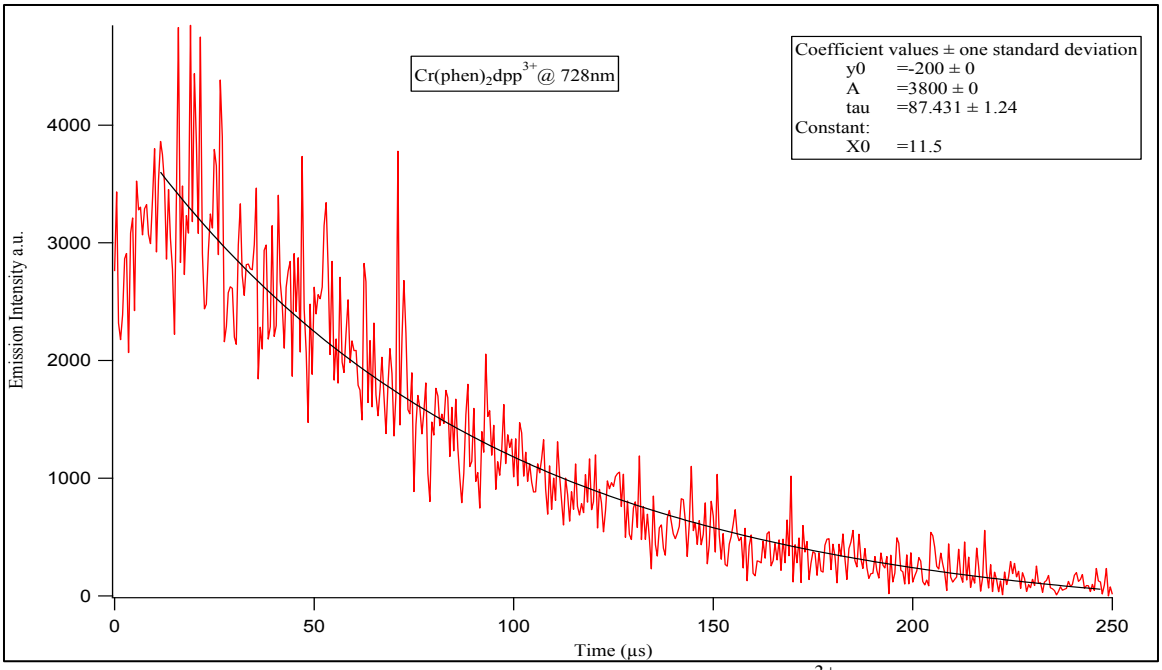

Figure 32. Time-resolved emission spectra of $[Cr(phen)_2(dpp)]^{3+}$ showing full trace with fit at 728 nm.

3. A.3. Electronic Spectroscopy of [Cr(bpy)$_2$(dpp)](PF$_6$)$_3$

The electronic spectrum of $[Cr(bpy)_2(dpp)]^{3+}$ appears in Figures 33 and 34. The UV–Vis absorption spectra (Figure 33) in aqueous solution of the $[Cr(bpy)_2(dpp)]^{3+}$ complex are strongly reminiscent of those observed for related tris(homoleptic) and tris(heteroleptic) Cr(III) complexes.[28] Similar to $[Cr(phen)_2(dpp)]^{3+}$, the UV-Vis spectra of $[Cr(bpy)_2(dpp)]^{3+}$ show the intense ligand-centered $\pi \rightarrow \pi^*$ absorptions in the UV range. The Laporte forbidden metal-centered d-d transitions above 380 nm are barely visible. The $[Cr(bpy)_2(dpp)]^{3+}$ complex yields the characteristic narrow phosphorescence emission ($^2E_g \rightarrow {}^4A_{2g}$) at 726 nm with the weak shoulder fluorescence ($^4T_{2g} \rightarrow {}^4A_{2g}$) at 694 nm (Figure 34).

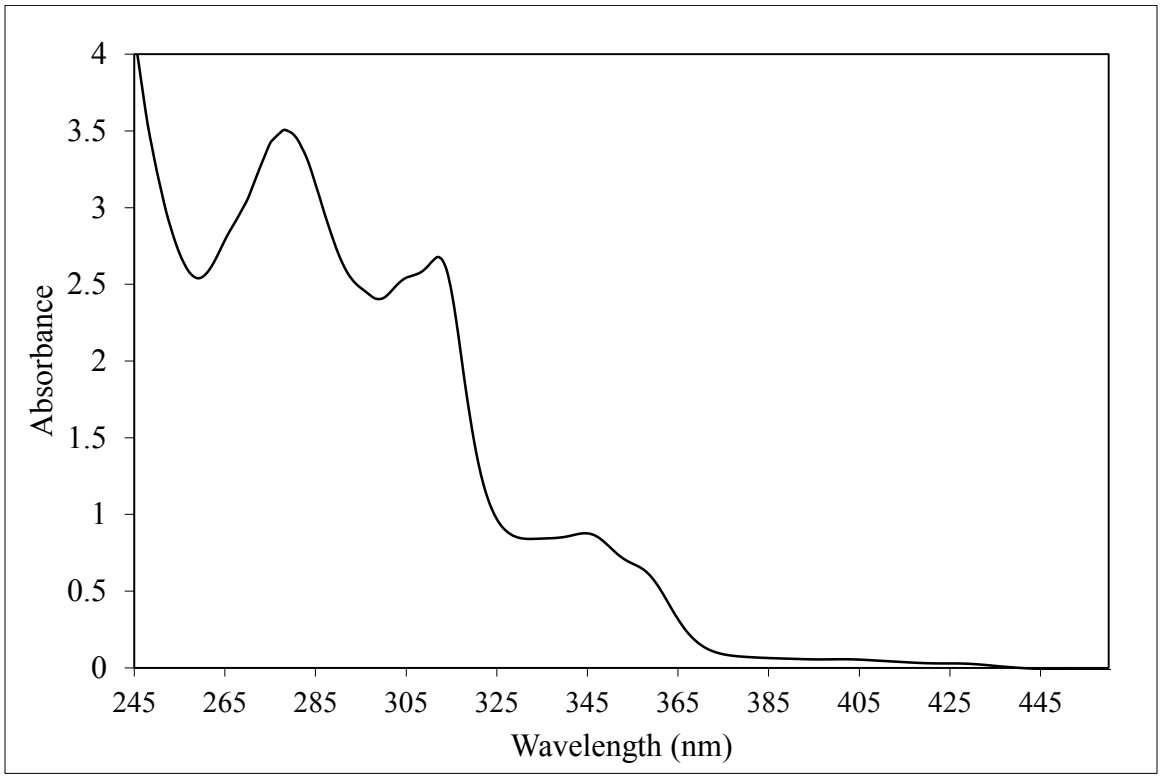

Figure 33. Absorption spectrum of 5.32 x 10^{-5} M $[Cr(bpy)_2(dpp)]^{3+}$ in Water (r.t.).

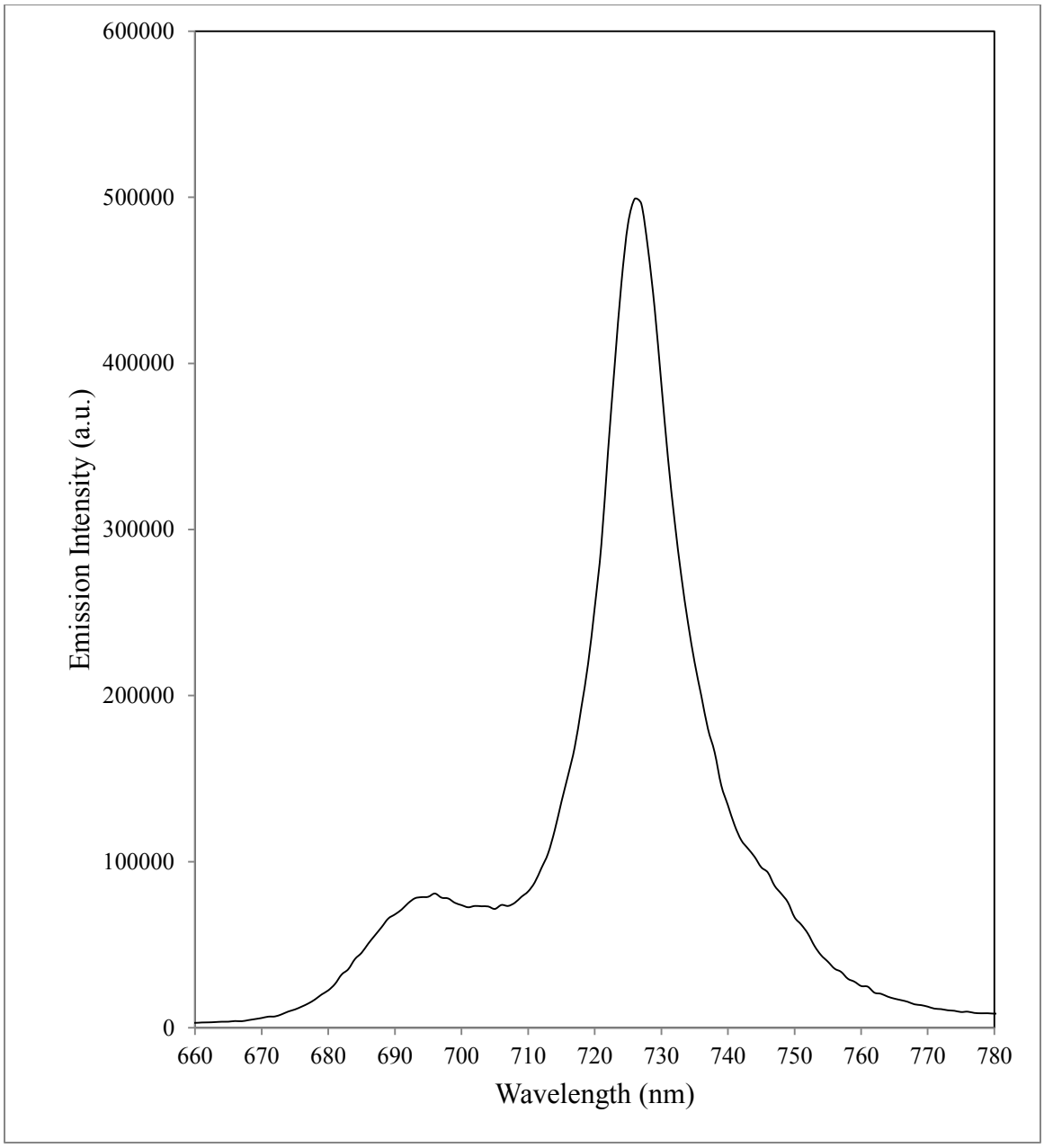

Figure 34. Emission of 4.62 x 10^{-4} M $[Cr(bpy)_2(dpp)]^{3+}$ in Water (r.t.). Excitation wavelength 400 nm.

The time-resolved spectrum of $[Cr(bpy)_2(dpp)]^{3+}$ was examined using the ICCD camera system. The full time-resolved three-dimensional spectrum is shown in Figure 35. The trace at the maximum emission intensity (726 nm) going from time zero (T_o) onwards is shown in Figure 37, which includes the grow-in of the emission. Fitting just the decay portion using IGOR led to a single exponential decay with a lifetime of 327 ± 7 μs (Figure 37). Measuring the lifetime at various wavelengths yields exactly the same lifetime as the 726 nm wavelength, suggesting that the lifetime of the $[Cr(bpy)_2(dpp)]^{3+}$ complex is wavelength independent. Another prominent feature in Figure 35 is the fluorescence at 694 nm, which appears only in the first frame and disappears thereafter due to its short lifetime (Figure 36).

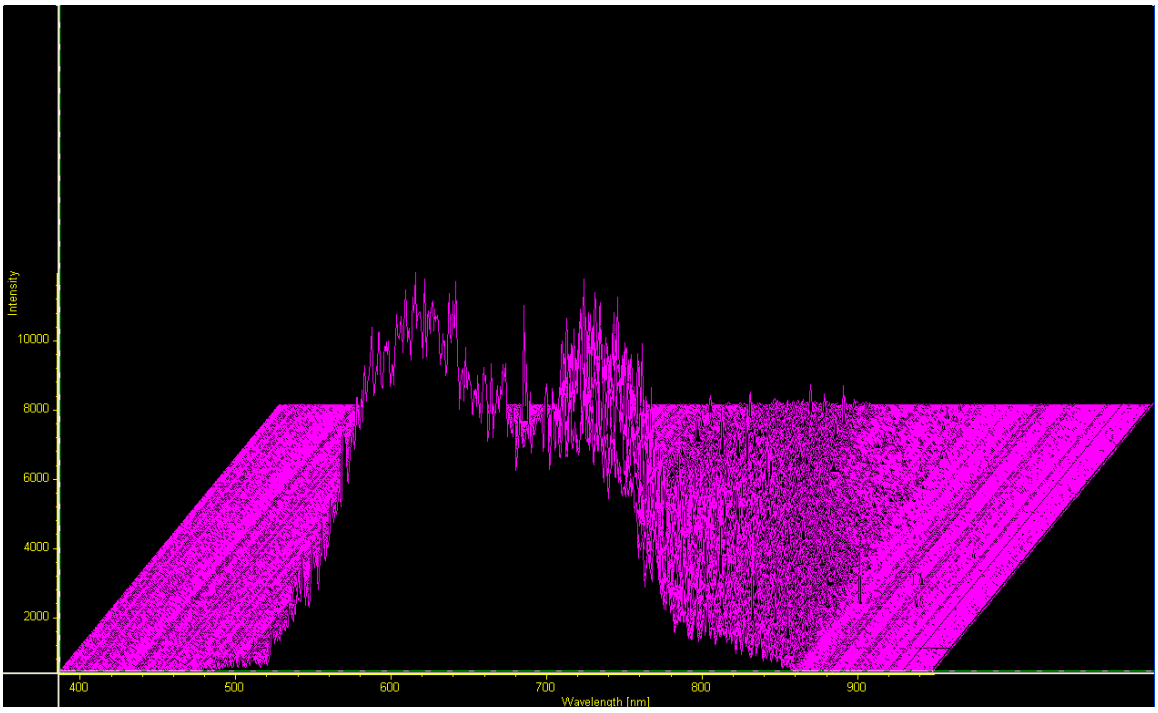

Figure 35. 3D time-resolved emission spectrum of 4.62×10^{-4} M $[Cr(bpy)_2(dpp)]^{3+}$ (r.t.).

A.

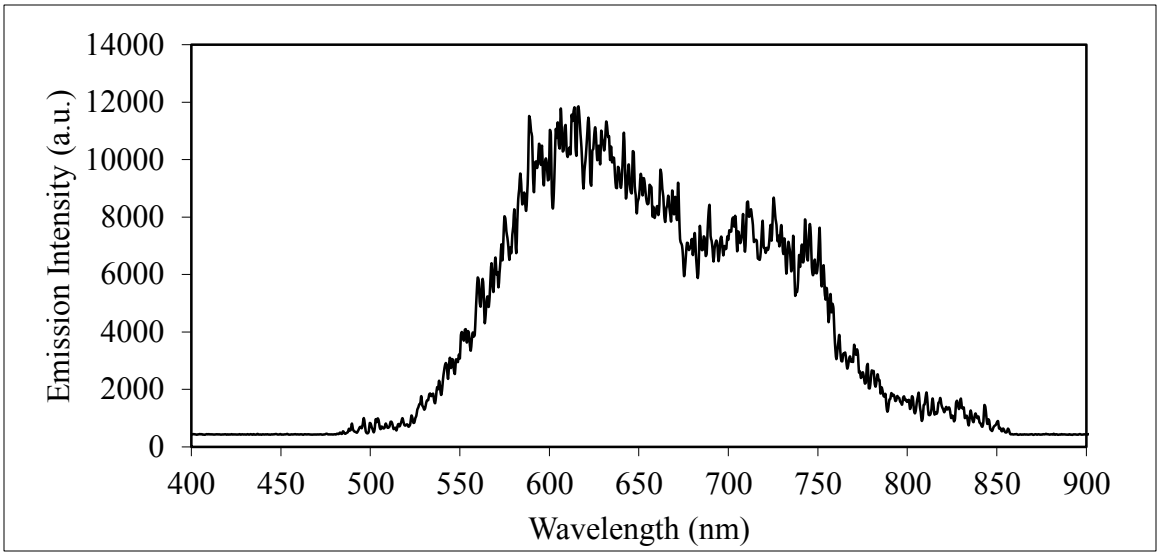

B.

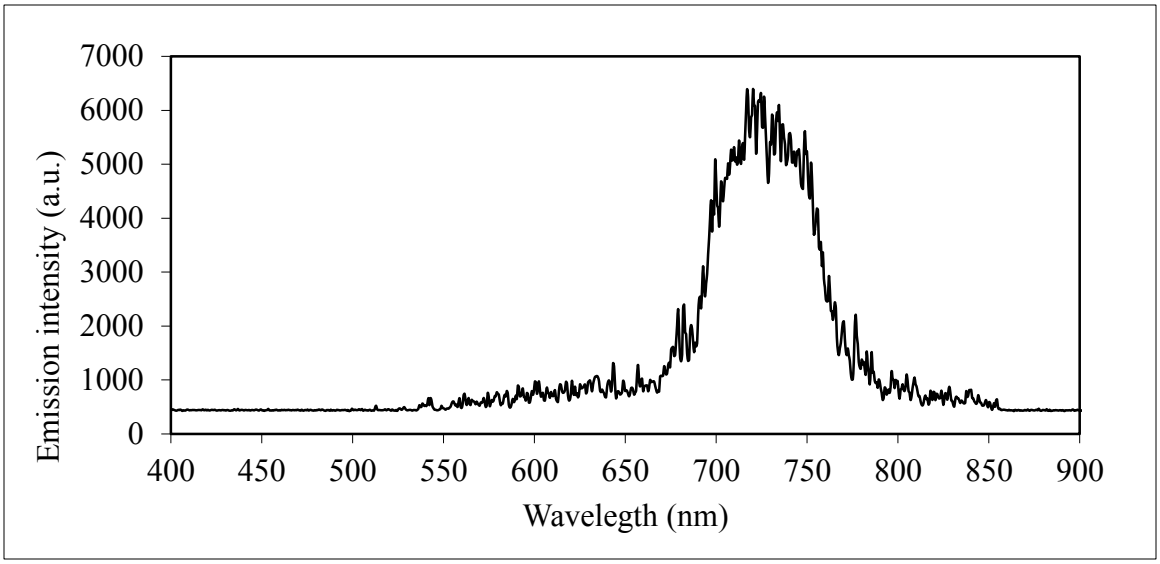

Figure 36. Time-resolved emission spectrum of 4.62×10^{-4} M $[Cr(bpy)_2(dpp)]^{3+}$ (r.t.).
A. at frame 1 and **B.** at frame 2.

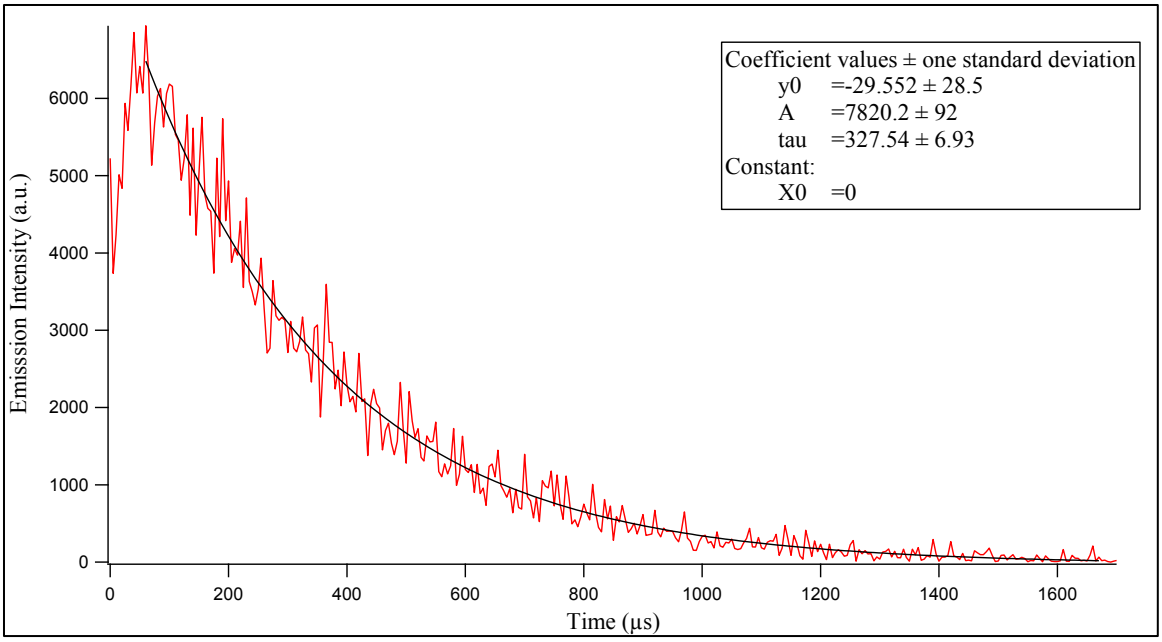

Figure 37. Time-resolved emission spectra of $[Cr(bpy)_2(dpp)]^{3+}$ showing full trace with fit at 726 nm.

3. B. Characterization of $[Rh(bpy)_3](PF_6)_3$ and $[Rh(bpy)_2(dpp)](PF_6)_3$

3. B.1. Electronic Spectroscopy of $[Rh(bpy)_3](PF_6)_3$

The electronic absorption and emission spectra of $[Rh(bpy)_3]^{3+}$ appear in Figures 38, 39a and 39b. They are in perfect agreement with literature sources [1,29]. The $[Rh(bpy)_3]^{3+}$ complex can be used to exemplify the typical photophysical behavior of this class of Rhodium(III) polypyridine complexes. The complex absorbs strongly in UV region, with prominent absorptions at 242, 306 and 319 nm, and molar extinction coefficients of 59,091 $M^{-1}cm^{-1}$, 54,927 $M^{-1}cm^{-1}$ and 59,818 $M^{-1}cm^{-1}$ respectively. After the 319 nm peak the absorption spectrum sharply terminates. Transitions in the UV region of the spectrum can be assigned to bpy ($\pi \rightarrow \pi^*$) transitions. $[Rh(bpy)_3]^{3+}$ exhibits in 77 K ethanol/methanol (4:1, v/v) glass an intense, long-lived (τ_o, ca. 62 ms), highly structured

emission (λ = 447, 479, 504, 543 nm) assigned as ligand-centered phosphorescence; emission from a $\pi \rightarrow \pi*$ triplet state ($^3T_1 \rightarrow {}^1A_1$) essentially localized on the bpy ligands. In room-temperature fluid acetonitrile or ethanol/methanol (4:1, v/v) solutions, $[Rh(bpy)_3]^{3+}$ is practically non-emitting (Figure 39b). [1,29]

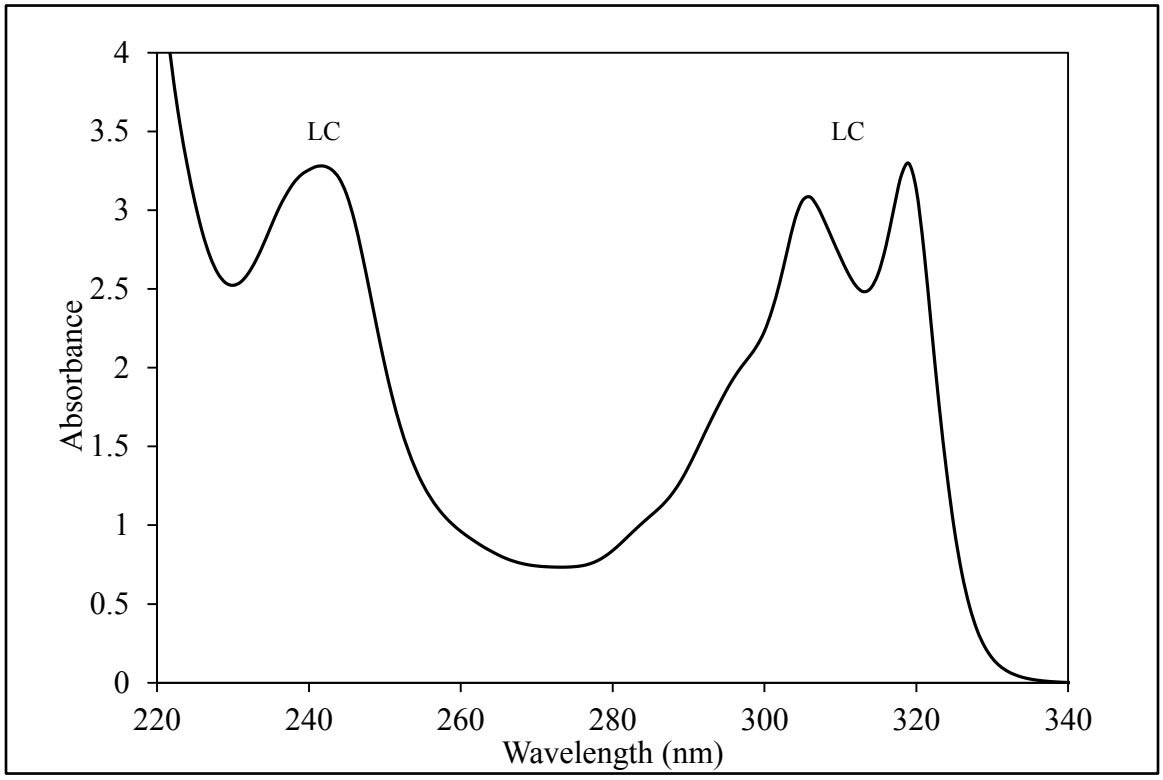

Figure 38. Absorption spectra of 5.5×10^{-5}M $[Rh(bpy)_3]^{3+}$ in Water (r.t.).

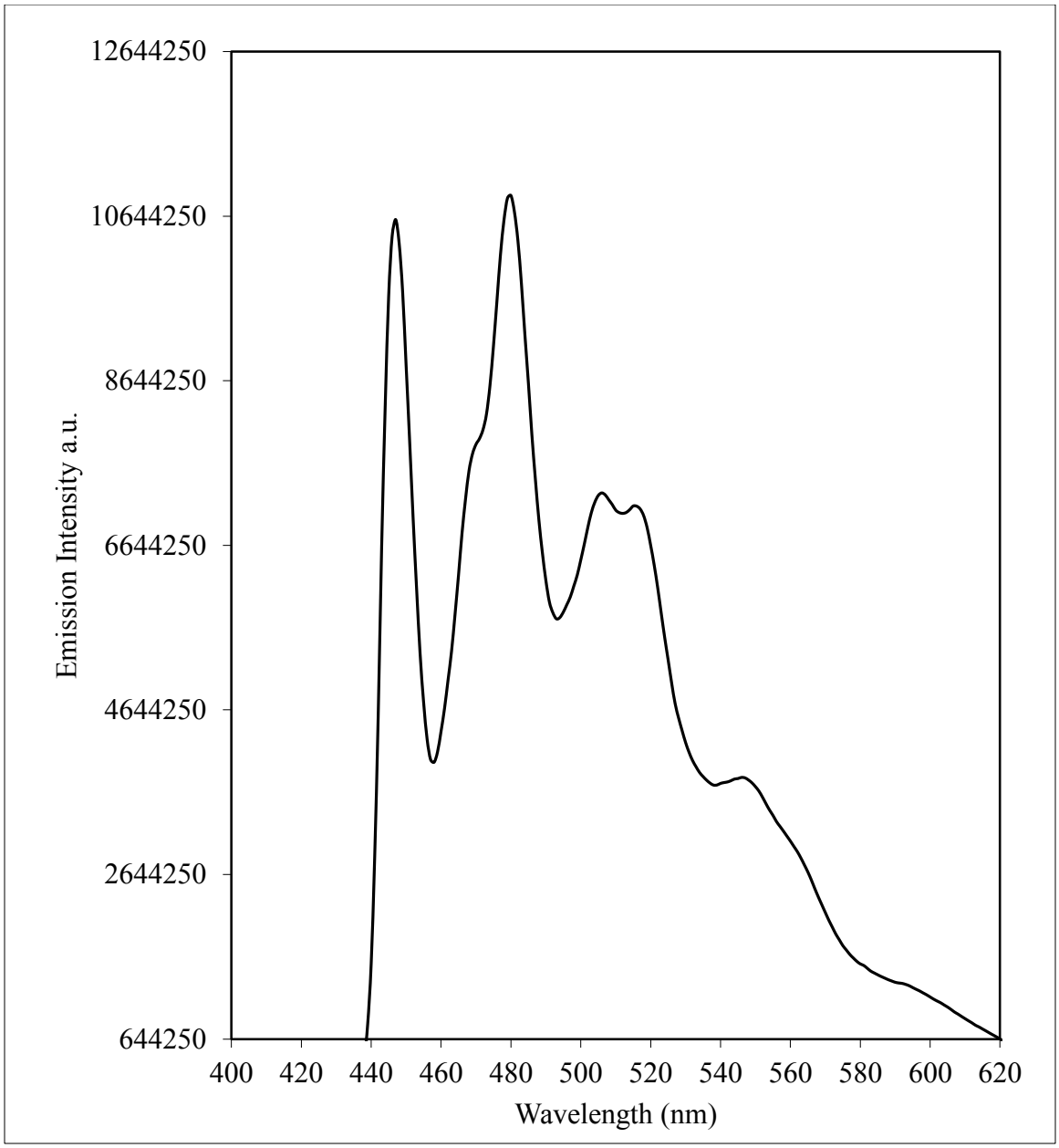

Figure 39a. Emission spectra of $4.5x10^{-4}$M $[Rh(bpy)_3]^{3+}$ in clear ethanol-methanol (4:1**,** v/v) glass at **77** K. Excitation wavelength 319 nm.

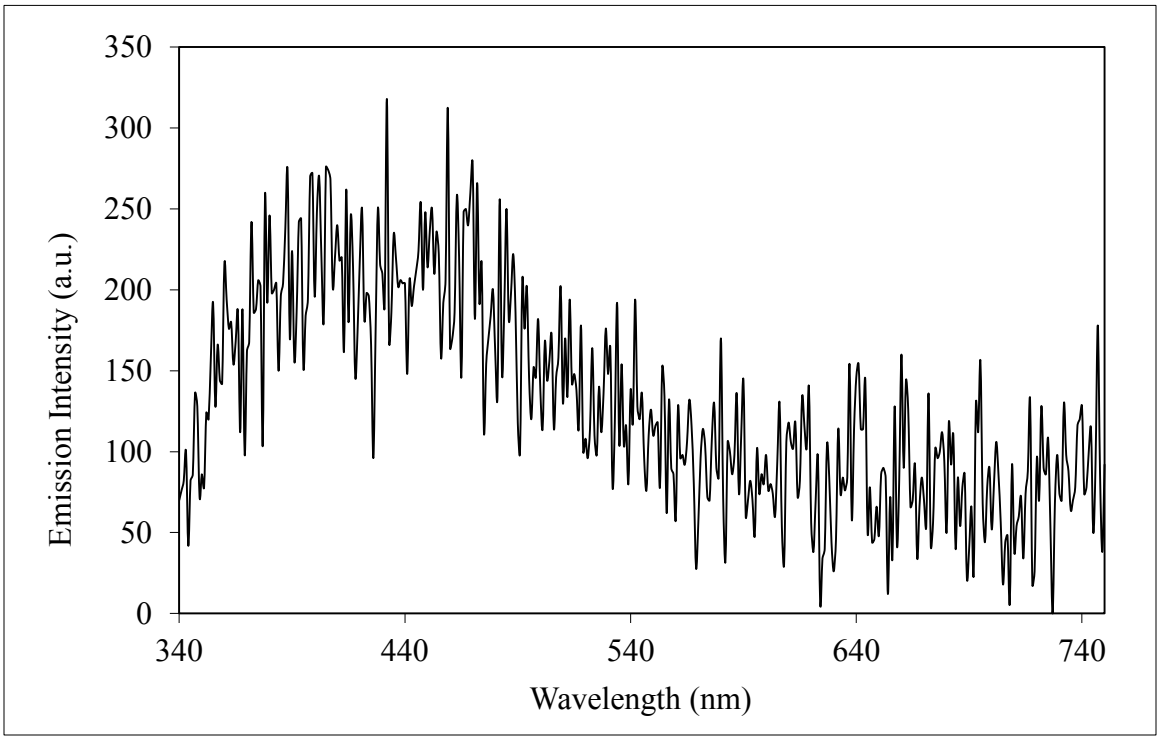

Figure 39b. Emission spectra of $4.5x10^{-4}$M $[Rh(bpy)_3]^{3+}$ in clear ethanol-methanol (4:1**,** v/v) glass at room temperature. Excitation wavelength 319 nm.

3. B.3. Electronic Spectroscopy of $[Rh(bpy)_2(dpp)](PF_6)_3$

The electronic absorption spectrum of $[Rh(bpy)_2dpp]^{3+}$ in water at room temperature appears in Figure 40. Similarly to the $[Rh(bpy)_3]^{3+}$ analogue, the $[Rh(bpy)_2dpp]^{3+}$ complex absorbs strongly in UV region, with prominent absorptions at 314, 241, 284, 295, 307 and 320 nm. After the 320 nm peak, the absorption spectrum sharply ends. These absorptions are the ligand centered $\pi \rightarrow \pi^*$ transitions; the lowest intensity absorption at 295 nm has a molar extinction coefficient of 41,695 $M^{-1}cm^{-1}$. By comparing Figures 38 and 40, the transitions at 284 nm and 295nm can be assigned to the dpp ligand, whereas the 307 nm and 320 nm can be assigned to the bpy ligand.

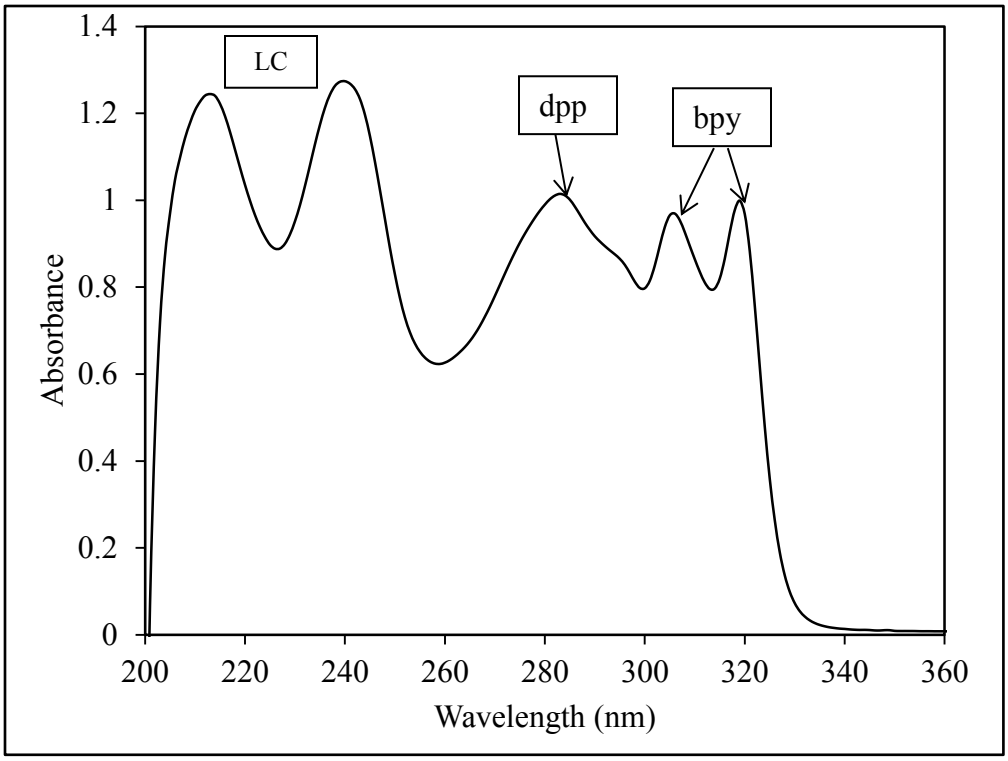

Figure 40. Absorption spectrum of 2.1 x 10^{-5} M $[Rh(bpy)_2(dpp)]^{3+}$ in Water (r.t.).

The $[Rh(bpy)_2dpp]^{3+}$ complex exhibits in 77 K ethanol/methanol (4:1, v/v) glass an intense emission (Figure 41, λ_{max} = 570 nm). This emission was examined using the Nd: YAG laser with an excitation pulse of 355 nm and gave a lifetime of 75 μs. However, in contrast to the $[Rh(bpy)_3]^{3+}$ complex, which does not show an emission in room temperature aqueous solution, $[Rh(bpy)_2dpp]^{3+}$ exhibits an intense, broad emission with a wavelength maximum at 443 nm in aqueous solution at room temperature (Figure 42). The location of this emission corresponds with a $\pi \rightarrow \pi^*$ ($^3T_1 \rightarrow {}^1A_1$) transition localized on the ligands. This emission is short lived with a lifetime of 17±3 ns; the time-resolved spectrum is shown in Figure 43A. The trace at the maximum emission intensity (448 nm) going from time zero (T_o) onwards is shown in Figure 43B. Curiously though, the

excitation spectrum for emission does not mirror the absorption spectrum. Shown in smaller graph in Figure 42, the excitation was monitored at 443 nm shows a maximum at 377 nm, in water (r.t.).

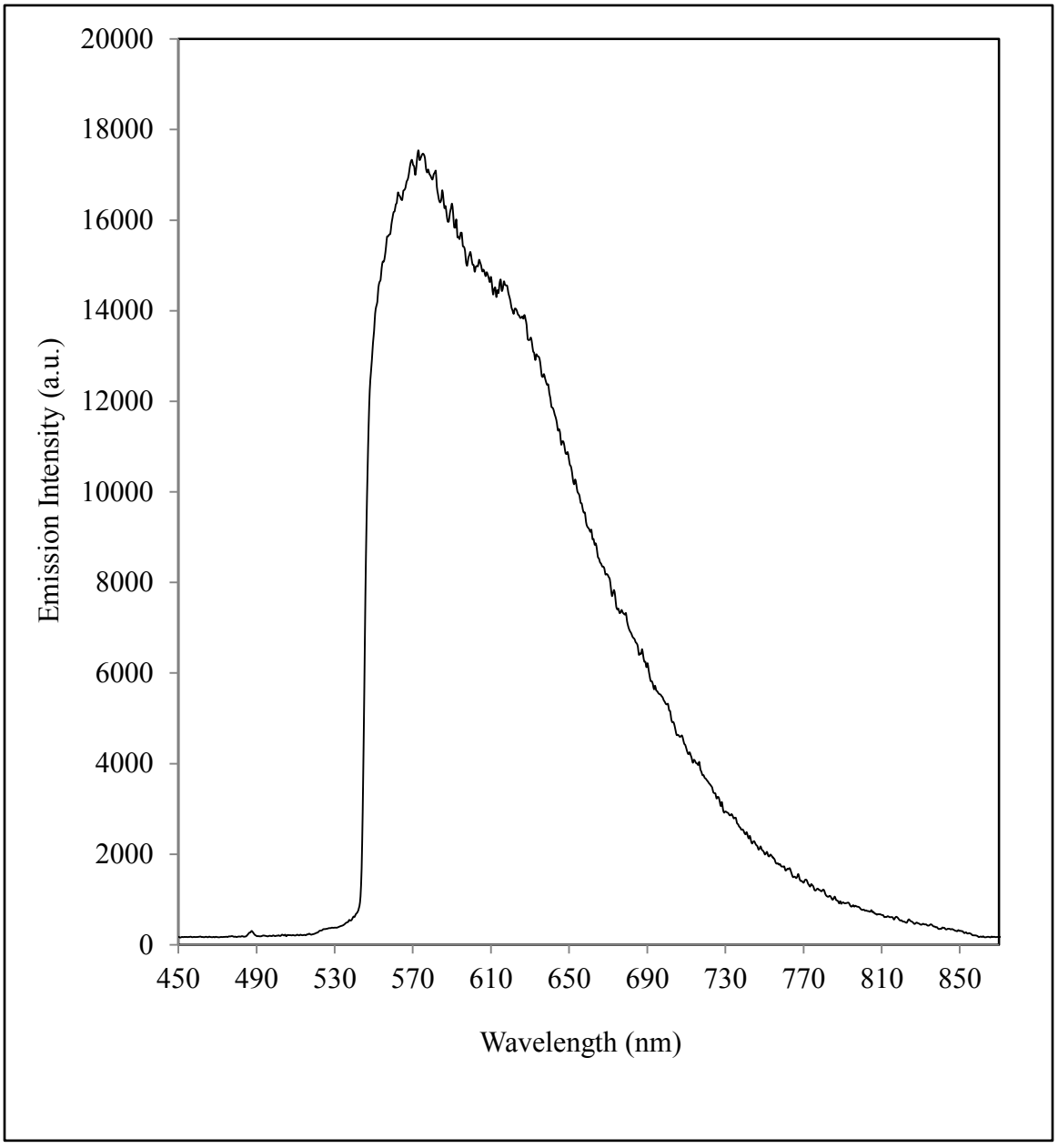

Figure 41. Emission spectra of 4.5×10^{-4}M $[Rh(bpy)_2dpp]^{3+}$ in clear ethanol-methanol (4:1, v/v) glass at 77 K. Excitation wavelength 319 nm.

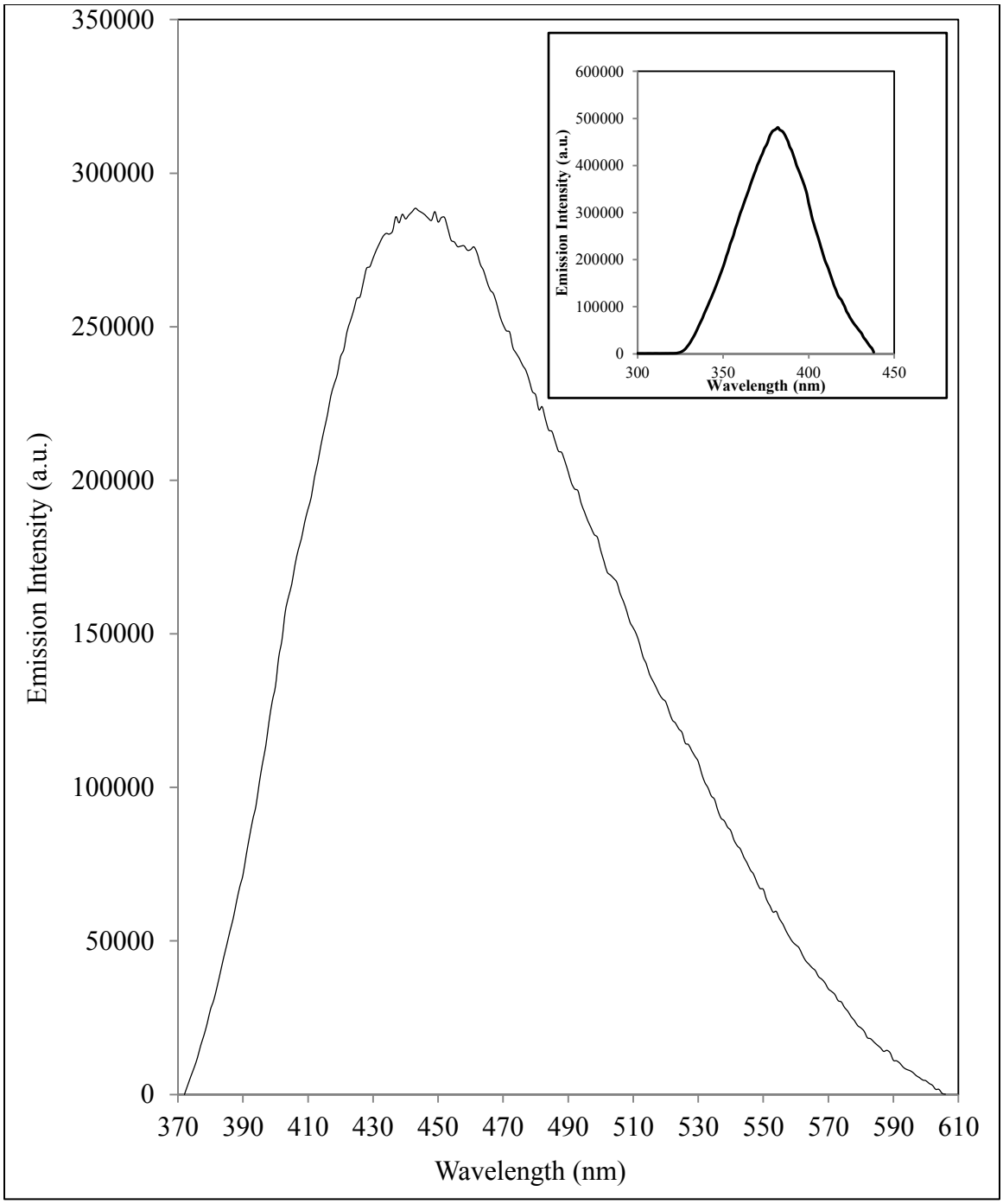

Figure 42. Emission of 4.25 x 10^{-5} M $[Rh(bpy)_2(dpp)]^{3+}$ in Water (r.t.).
Excitation wavelength 319 nm. Excitation spectrum of $Rh(bpy)_2(dpp)]^{3+}$ shown in smaller figure monitored at 443 nm with a maximum at 377 nm, in water (r.t.) .

A.

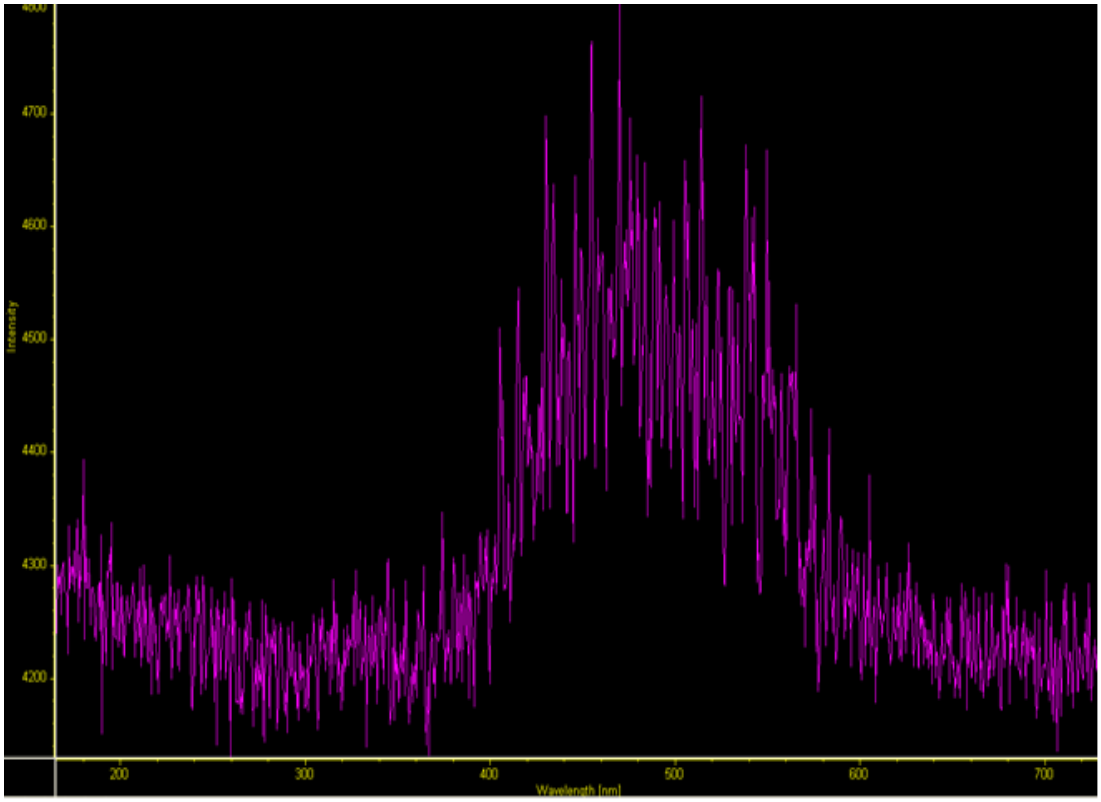

B.

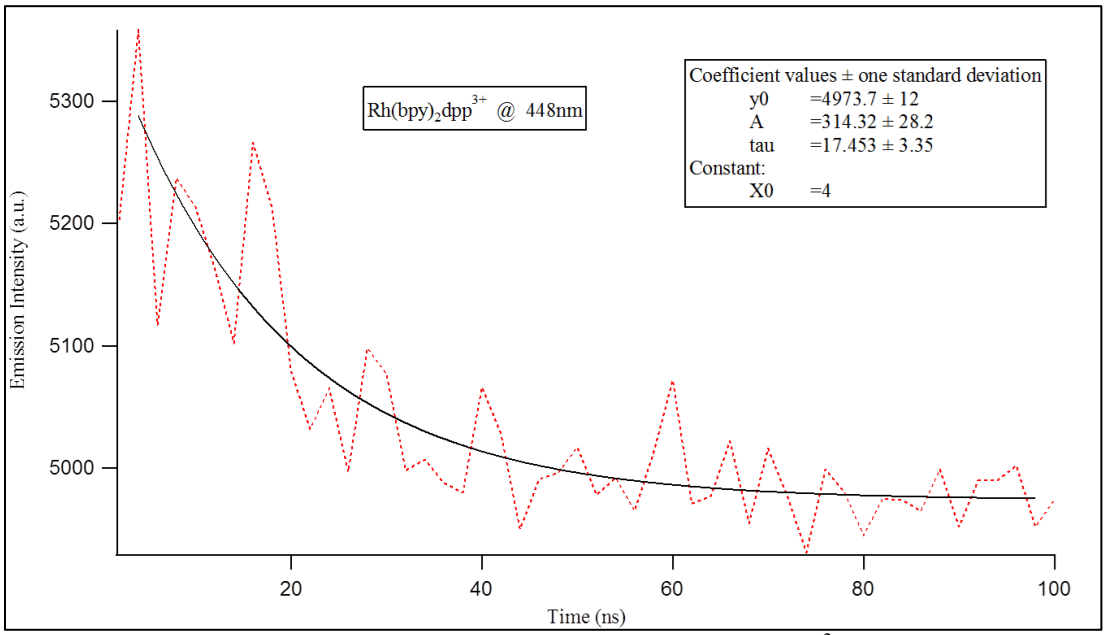

Figure 43. Time-resolved emission spectra of $[Rh(bpy)_2(dpp)]^{3+}$ (A),showing full trace with fit at 448 nm (B).

3. C. Quantum Yield Determinations

3. C.1. Quantum Yield Determination of $[Cr(phen)_2dpp]^{3+}$

$[Cr(bpy)_3]^{3+}$ is more thoroughly characterized in the literature than $[Cr(phen)_3]^{3+}$; thus, it was used as a standard to determine the quantum yield of $[Cr(phen)_2dpp]^{3+}$. Sriram *et al*. [57] experimentally calculated the quantum yield of $[Cr(bpy)_3]^{3+}$ to be 0.081. This value was reported in deareated aqueous solution at pH=5 and temperature of 22°C. Figure 45 shows the emission data for $[Cr(bpy)_3]^{3+}$ and $[Cr(phen)_2dpp]^{3+}$ at various concentrations in buffer solution of pH=5 and at approximately 22°C. The side-by-side comparison of absorbance vs. emission area and the gradients are shown in Figure 44. Using Equation 26 and the ratio of the gradients from Figure 44 the quantum yield of emission for $[Cr(phen)_2dpp]^{3+}$ was determined to be 0.0911 ± 0.0002.

According to equation 14, the quantum yields of radiative and non-radiative decay, Φ_{em} and Φ_{nr} respectively, are

$$\Phi_{em} = \frac{k_r}{k_r + k_{nr}} \tag{27}$$

and

$$\Phi_{nr} = \frac{k_{nr}}{k_r + k_{nr}} \tag{28}$$

Quantum yield can be thought of as the probability that absorption of one photon will lead to a particular radiative or non-radiative event. Since all possible events must be accounted for, it is clear that

$$\Phi_{em} + \Phi_{nr} = 1 \quad (29)$$

Applying Equation18 and the experimentally obtained values of Φ_{em} and τ_{obs} (or simply designated τ), the radiative and non-radiative rate constants can be determined from

$$k_r = \frac{\Phi_{em}}{\tau} \quad (30)$$

$$k_{nr} = \frac{1-\Phi_{em}}{\tau} \quad (31)$$

With the quantum yield available, the radiative and non-radiative rate constants, k_r and k_{nr}, are calculated from equations (30) and (31). For $[Cr(phen)_2(dpp)]^{3+}$, $k_r = 1.05 \times 10^3\ s^{-1}$ and $k_{nr} = 1.04 \times 10^4 s^{-1}$.

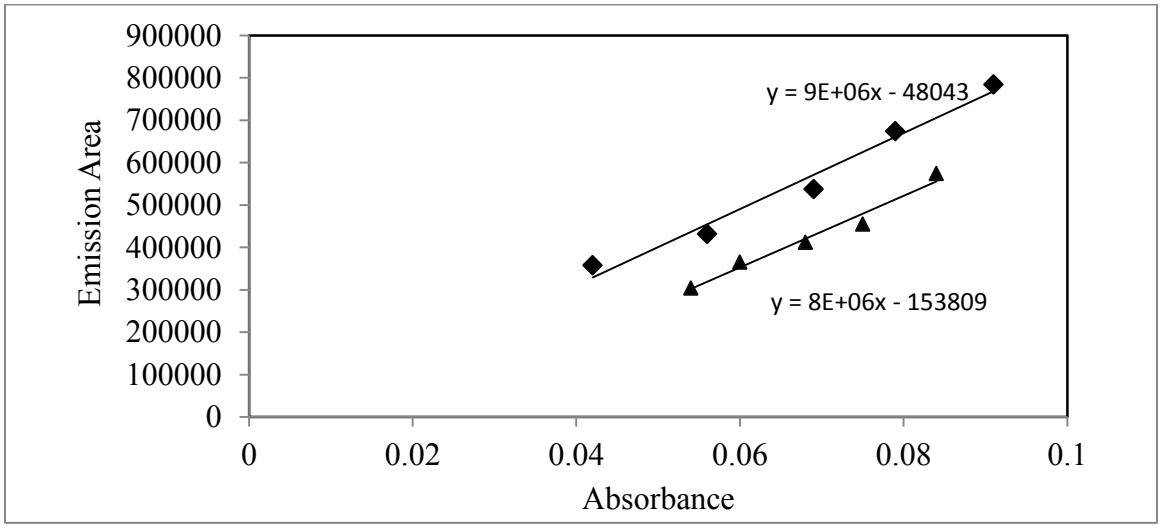

Figure 44. Plots of emission area vs. absorbance at 400 nm for $[Cr(phen)_2(dpp)]^{3+}$ (♦) and for $[Cr(bpy)_3)]^{3+}$ (▲): Gradients.

A.

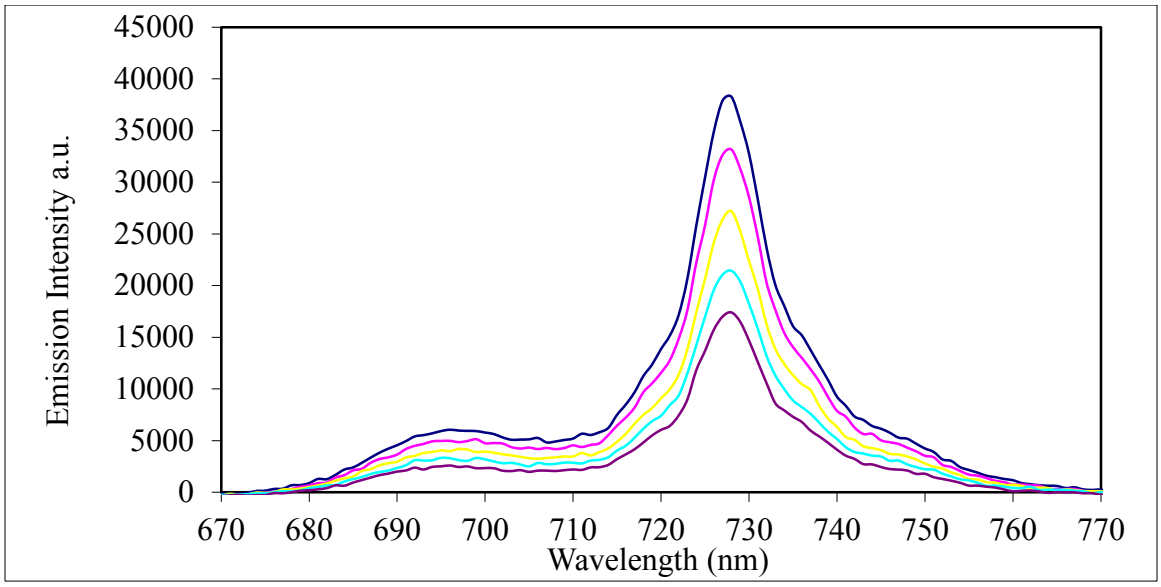

B.

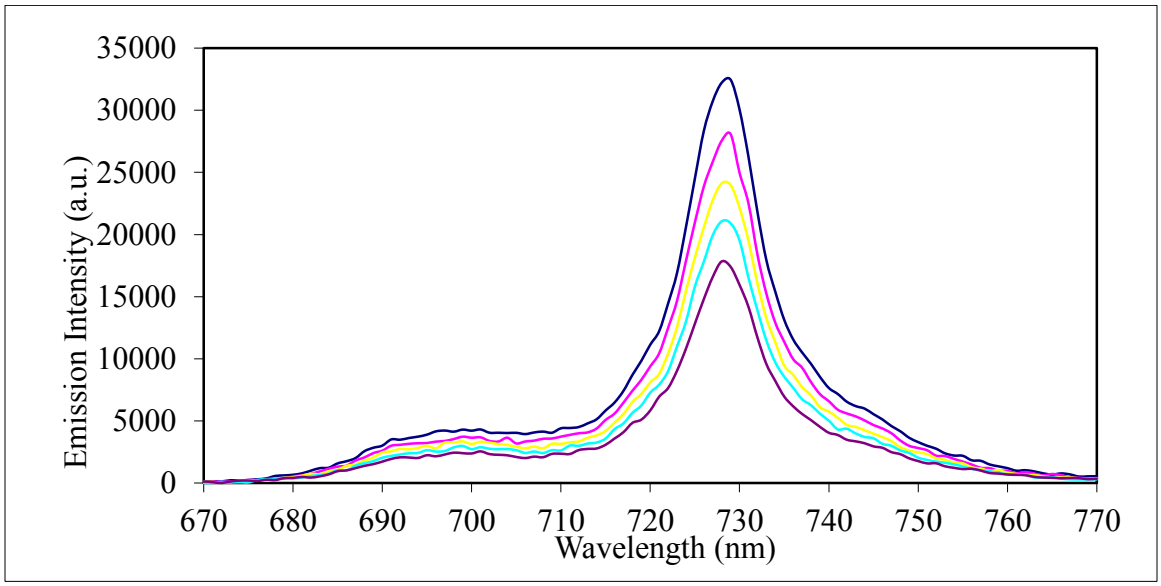

Figure 45. Emission spectra of (A) $[Cr(phen)_2dpp]^{3+}$ and (B) $[Cr(bpy)_3]^{3+}$ as a function of the concentration of each complex. All solutions were excited at 400 nm which corresponds to $^4A_{2g} \rightarrow {}^4T_{1g}$.

3. C.2. Quantum Yield Determination of $[Rh(bpy)_2dpp]^{3+}$

Since *cis*-$[Rh(bpy)_2Cl_2]^+$ is more thoroughly characterized in the literature than $[Rh(bpy)_3]^{3+}$, it was used as a standard to determine the quantum yield of emission for $[Rh(bpy)_2dpp]^{3+}$. Demas *et al.* [84] experimentally calculated the quantum yield of *cis*-$[Rh(bpy)_2Cl_2]^+$ to be 0.037; results were reported for an ethanol-methanol glass (4:1; v/v) at 77°K. Representative absorption and emission spectra of $[Rh(bpy)_2dpp]^{3+}$ and $[Rh(bpy)_2Cl_2]^+$ are shown in Figures 46 and 47. For $[Rh(bpy)_2dpp]^{3+}$ the excitation wavelength was chosen to be 319 nm and for $[Rh(bpy)_2Cl_2]^+$ was 314 nm wavelength. The emission of the $[Rh(bpy)_2Cl_2]^+$ is very weak with a wavelength maximum at 685 nm and it is a d-d transition[95]. Using the data from Tables 2.1 and 2.2 and Equation 27 the quantum yield of $[Rh(bpy)_2dpp]^{3+}$ is determined to be 0.0760.

TABLE 2.1. *$[Rh(bpy)_2Cl_2]^+$ data.*

Sample	Absorbance at 314nm	Integrated Emission, $\lambda_{ex.}$=314nm
1	0.11	128,402
2	0.087	101,549
3	0.056	64,901
4	0.025	29,181

TABLE2.2. *$[Rh(bpy)_2dpp]^{3+}$ data.*

Sample	Absorbance at 320nm	Integrated Emission, $\lambda_{ex.}$=320nm
1	0.037	548,458
2	0.022	359,258
3	0.014	235,145
4	0.005	120,145

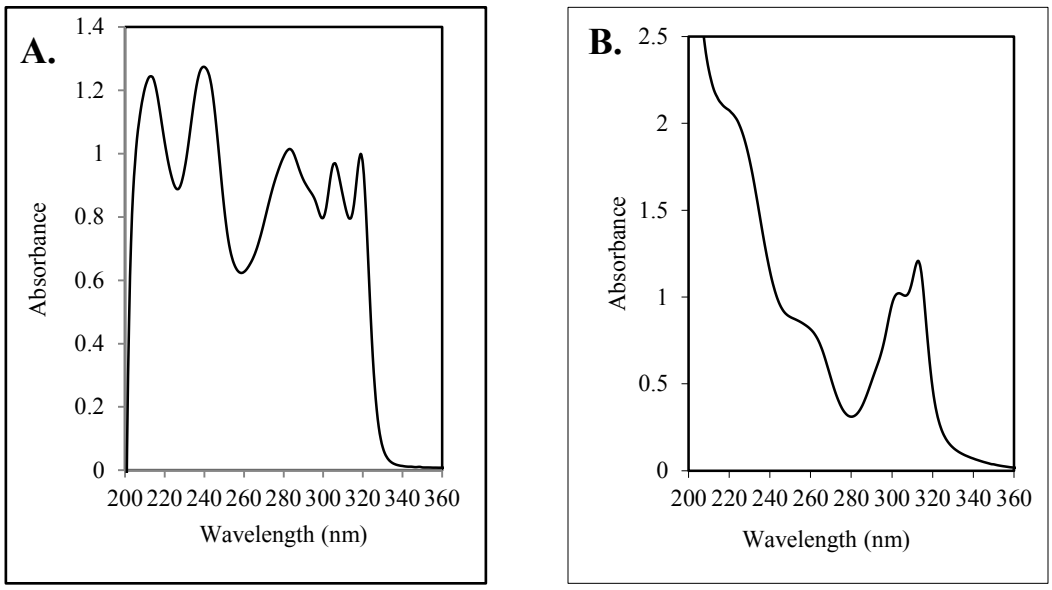

Figure 46. (**A**)Absorption spectrum of $4.5x10^{-4}$M $[Rh(bpy)_2dpp]^{3+}$ in ethanol-methanol (4:1**,** v/v) **(B)** Absorption spectrum of $6.7x10^{-4}$M $[Rh(bpy)_2Cl_2]^{+}$ in ethanol-methanol (4:1**,** v/v).

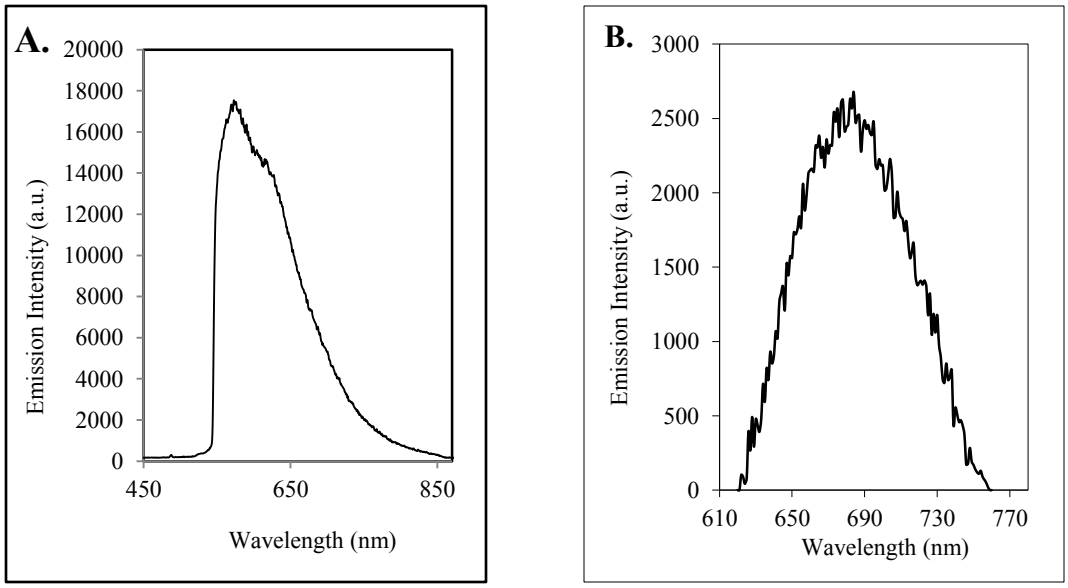

Figure 47. (**A**)Emission spectrum of $4.5x10^{-4}$M $[Rh(bpy)_2dpp]^{3+}$ in clear ethanol-methanol (4:1**,** v/v) glass at **77** K, excitation wavelength 319 nm. **(B)**Emission spectrum of $6.7x10^{-4}$M $[Rh(bpy)_2Cl_2]^{+}$ in clear ethanol-methanol (4:1**,** v/v) glass at **77** K, excitation wavelength 314 nm.

3. D. Electrochemical Measurements

3. D.1. Electrochemical Behavior of [Cr(diimine)$_3$]$^{3+}$ Complexes

The electrochemical properties of [Cr(bpy)$_2$(dpp)]$^{3+}$, [Cr(phen)$_2$(dpp)]$^{3+}$, [Cr(phen)$_3$]$^{3+}$ and [Cr(bpy)$_3$]$^{3+}$ were investigated by cyclic voltammetry. The cyclic voltammograms of [Cr(phen)$_2$(dpp)]$^{3+}$ and [Cr(bpy)$_2$(dpp)]$^{3+}$ are shown in Figures 48 and 49 respectively, and a complete listing of the Cr^{3+}/Cr^{2+} reduction potentials obtained are presented in table 3. All Cr(diimine)$_3^{3+}$ complexes exhibit a reversible Cr^{3+}/Cr^{2+} couple, from which values for the standard reduction potentials, $E°(Cr^{3+}/Cr^{2+})$, were determined. For the homoleptics Cr(bpy)$_3^{3+}$ and Cr(phen)$_3^{3+}$, the reduction potentials are slightly less negative than those reported by Brunschwig and Sutin under somewhat different conditions (1M LiCl solution).[52] A clear dependence of $E°(Cr^{3+}/Cr^{2+})$ on diimine ligand type is evident from the data in Table 3, with the ease of Cr^{3+} reduction most favored by the presence of bpy/dpp and least favored when phen/dpp are ligands.

TABLE 3.
Electrochemical data of polypyridine Chromium (III) complexes (Cr(diimine)$_3^{3+}$) in aqueous solution (r.t.).

Complex	$E°/V(Cr^{3+}/Cr^{2+})$
Cr(bpy)$_3^{3+}$	-0.24
Cr(phen)$_3^{3+}$	-0.26
Cr(phen)$_2$(dpp)$^{3+}$	-0.52
Cr(bpy)$_2$(dpp)$^{3+}$	-0.23

3. D.2. Electrochemical Behavior of [Rh(diimine)$_3$]$^{3+}$ Complexes

The electrochemical properties of [Rh(bpy)$_2$(dpp)]$^{3+}$, and [Rh(bpy)$_3$]$^{3+}$ were also investigated by cyclic voltammetry. The cyclic voltammograms of [Rh(bpy)$_2$(dpp)]$^{3+}$ and [Rh(bpy)$_3$]$^{3+}$ are shown in Figures 50 and 51 respectively. Both Rh(diimine)$_3^{3+}$

complexes undergo a chemically irreversible two-electron reduction from Rh(III) to Rh(I) with a concomitant change in coordination number and geometry from octahedral (CN=6) to square planar (CN= 4). The chemical irreversibility of the initial reduction wave arises from ejection of a ligand after electrochemical reduction of the parent compound. This reduction is followed by two reversible one-electron reductions of the remaining diimine ligands.[66,67] Electrochemical potentials for both Rhodium(III) complexes are given in Table 4, The $Rh(bpy)_3^{3+}$ data are in agreement with data of DeArmond *et al.*[79] Both $[Rh(bpy)_2(dpp)]^{3+}$ and $[Rh(bpy)_3]^{3+}$ complexes show a chemically irreversible two-electron wave at approximately -0.83V followed by two chemically reversible, one-electron bpy and dpp waves. The chemically irreversible two-electron wave corresponds to the Rh(III) to Rh(I) reduction and the simultaneous loss of a ligand as a result of the preference of Rh(I) d^8 complexes for the four-coordinate square-planar geometry. According to DeArmond *et al.*[79] the Rh(III) complex accepts one electron to form the Rh(II) complex, which rapidly loses a bpy ligand and picks up a solvent molecule to achieve an 18-electron, five-coordinate complex. This complex then picks up the second electron, making it Rh(I), which rapidly loses the solvent molecule to form the four-coordinate, 16-electron, square-planar geometry preferred by a d^8 metal.

TABLE 4.
Electrochemical data of polypyridine Rhodium (III) complexes ($Rh(diimine)_3^{3+}$) in acetonitrile solution (r.t.).

Complex	$E_{pc}/V(Rh^{3+}/Rh^{+})$
$Rh(bpy)_2(dpp)^{3+}$	-0.85
$Rh(bpy)_3^{3+}$	-0.79

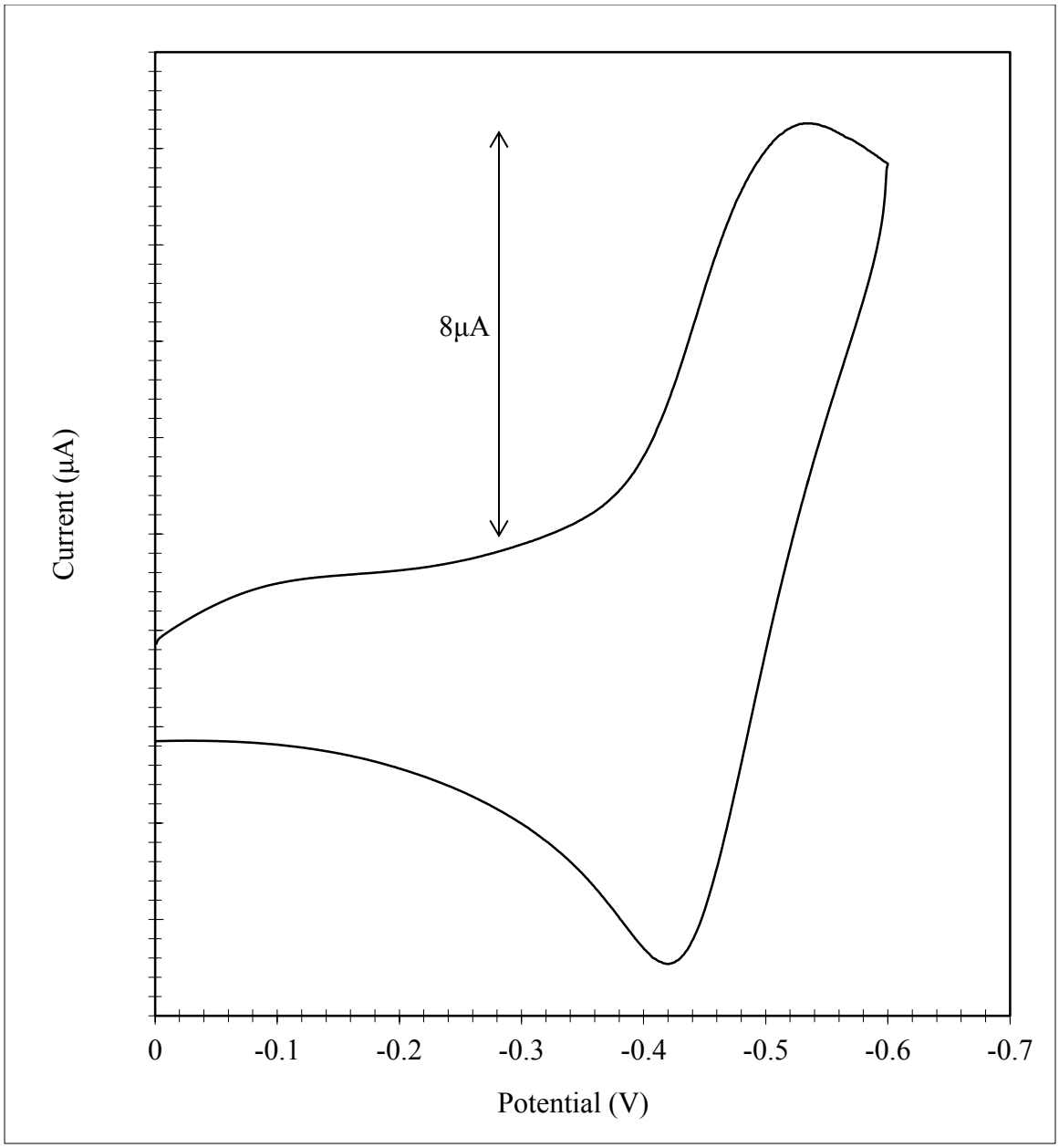

Figure 48. Cyclic voltammogram of $[Cr(phen)_2dpp](CF_3SO_3)_3$ in 0.1 M KCl aqueous solution at a platinum disc working electrode versus Ag/AgCl (3M NaCl) and with platinum wire counter electrode. Scan rate (v) = 100mV/s.

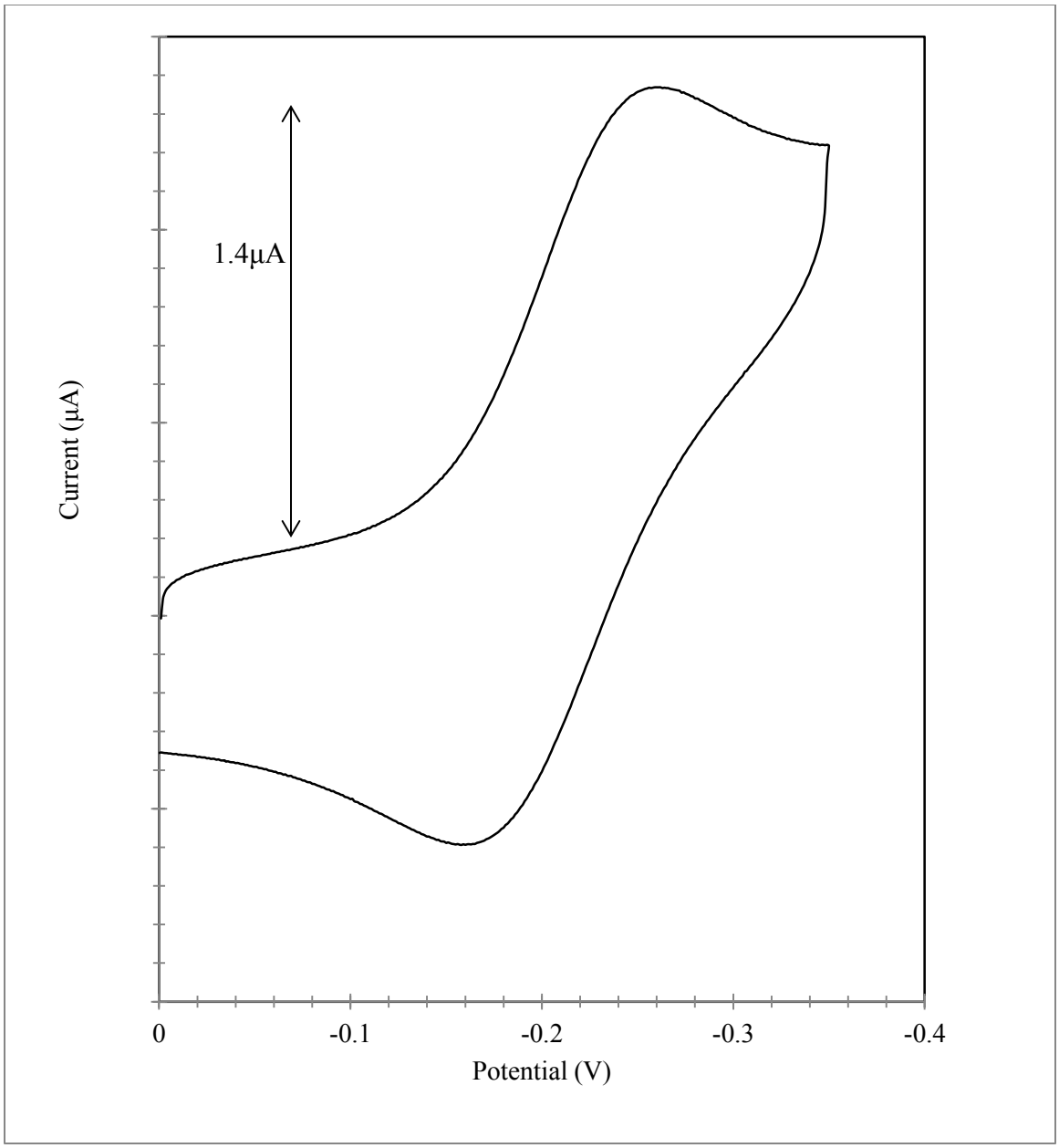

Figure 49. Cyclic voltammogram of $[Cr(bpy)_2dpp](CF_3SO_3)_3$ in 0.1 M KCl aqueous solution at a platinum disc working electrode versus Ag/AgCl (3M NaCl) and with platinum wire counter electrode. Scan rate (v) = 100mV/s.

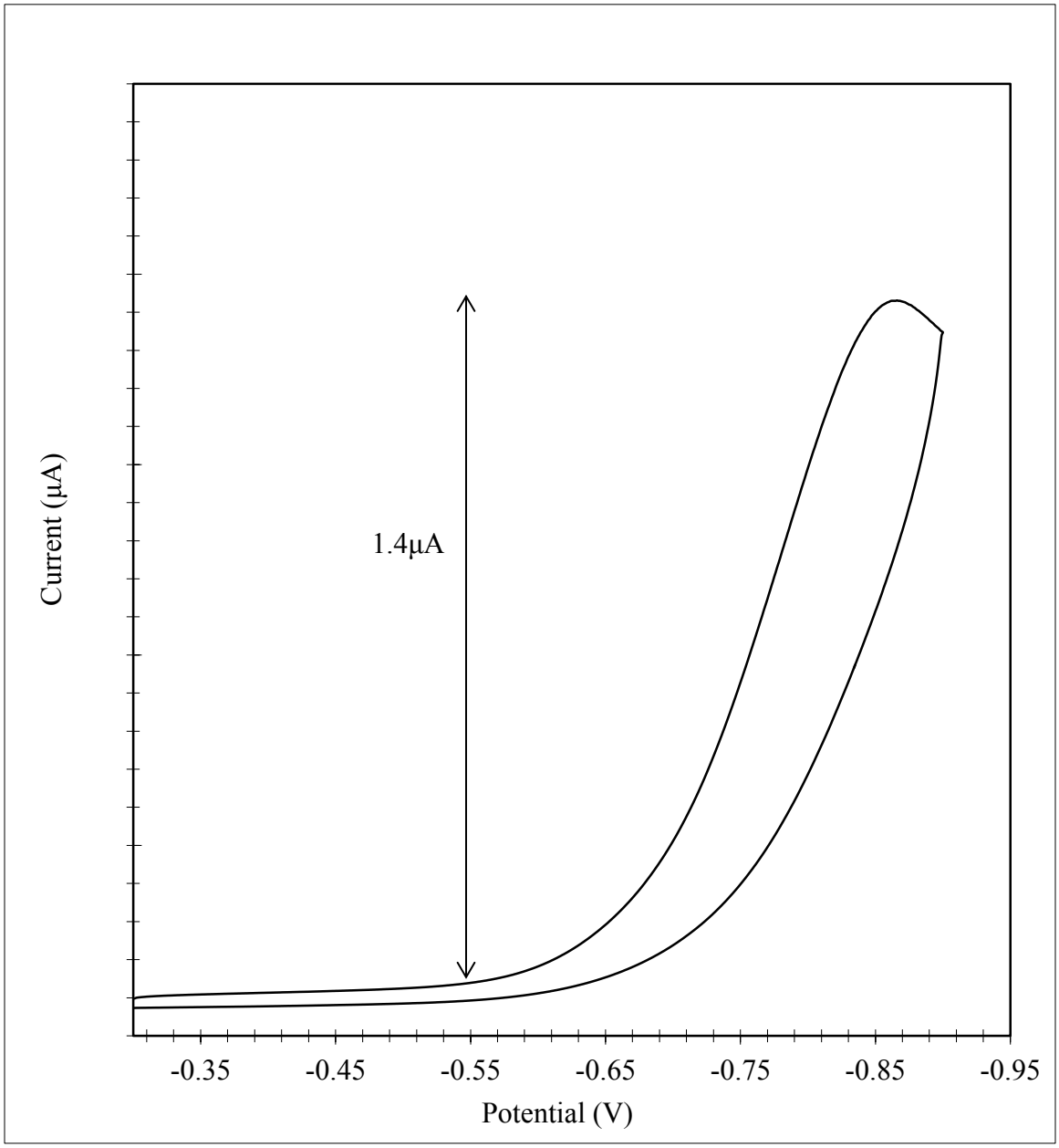

Figure 50. Cyclic voltammogram of $[Rh(bpy)_2(dpp)](PF_6)_3$ in 0.1 M Bu_4NPF_6 acetonitrile at a platinum disc working electrode versus Ag/AgCl (3M NaCl) and with platinum wire counter electrode. Scan rate (v) = 100 mV/s.

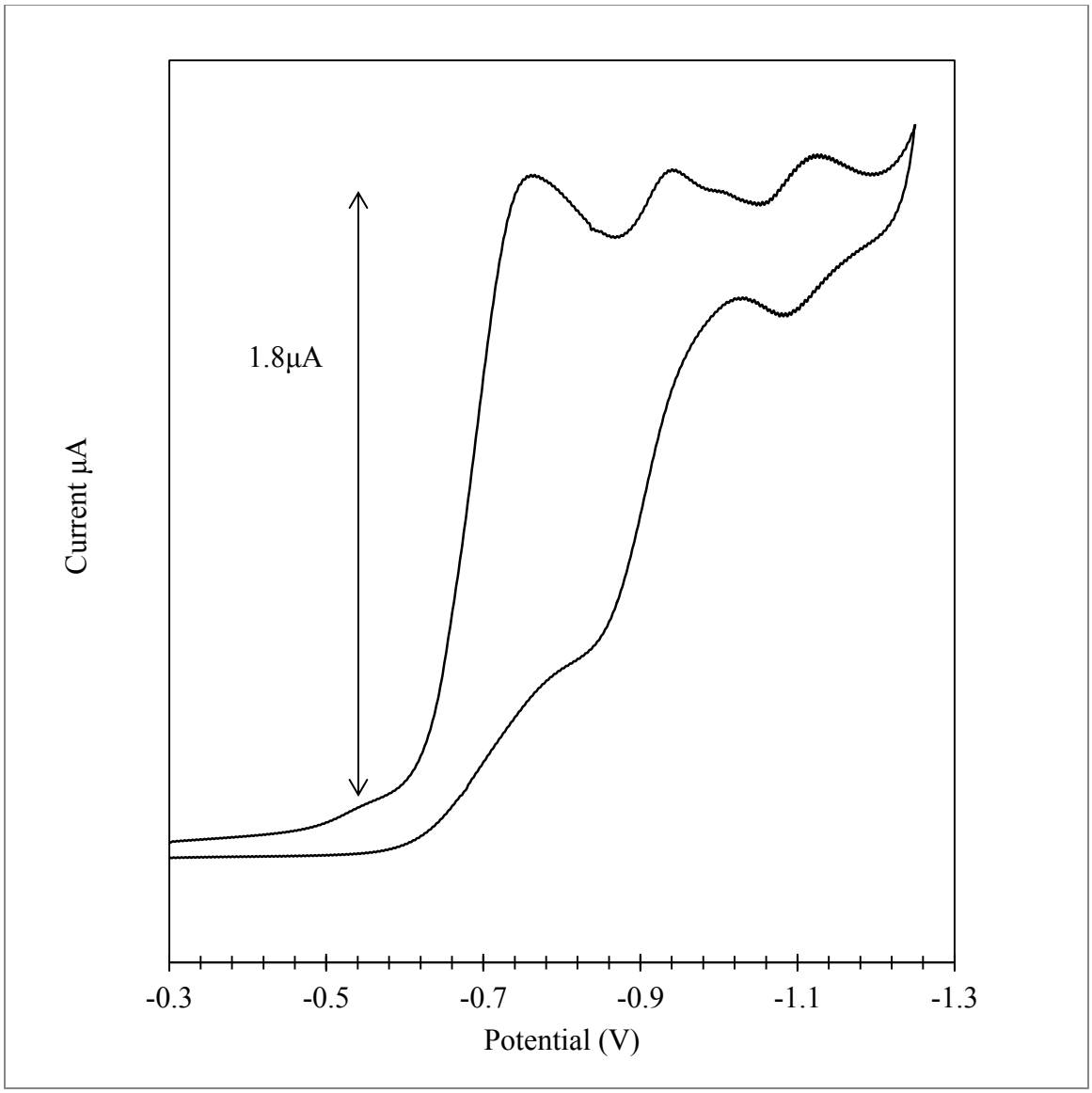

Figure 51. Cyclic voltammogram of $[Rh(bpy)_3](PF_6)_3$ in 0.1 M Bu_4NPF_6 acetonitrile at a platinum disc working electrode versus Ag/AgCl (3M NaCl) and with platinum wire counter electrode. Scan rate (v) = 100 mV/s.

3. E. TITRATIONS

3. E.1. Absorption and Emission Spectra of [Cr(phen)$_2$(dpp)]$^{3+}$

The emission of [Cr(phen)$_2$(dpp)]$^{3+}$ monitored in buffer solutions ranging from pH1 to pH10 is shown in Figure 52. Both the phosphorescence and fluorescence are gradually decreasing with increasing pH, with a dramatic decrease in intensity at pH9 and with complete quenching occurring at pH10. The pH titration plots of the phosphorescence at 728 nm and fluorescence at 696 nm show an inflection point at 8.7 (Figures 53 and 54). For each solution the lifetime was recorded. The lifetime remained relatively constant at 87±3 μs, suggesting that static quenching is occurring (Figure 55).

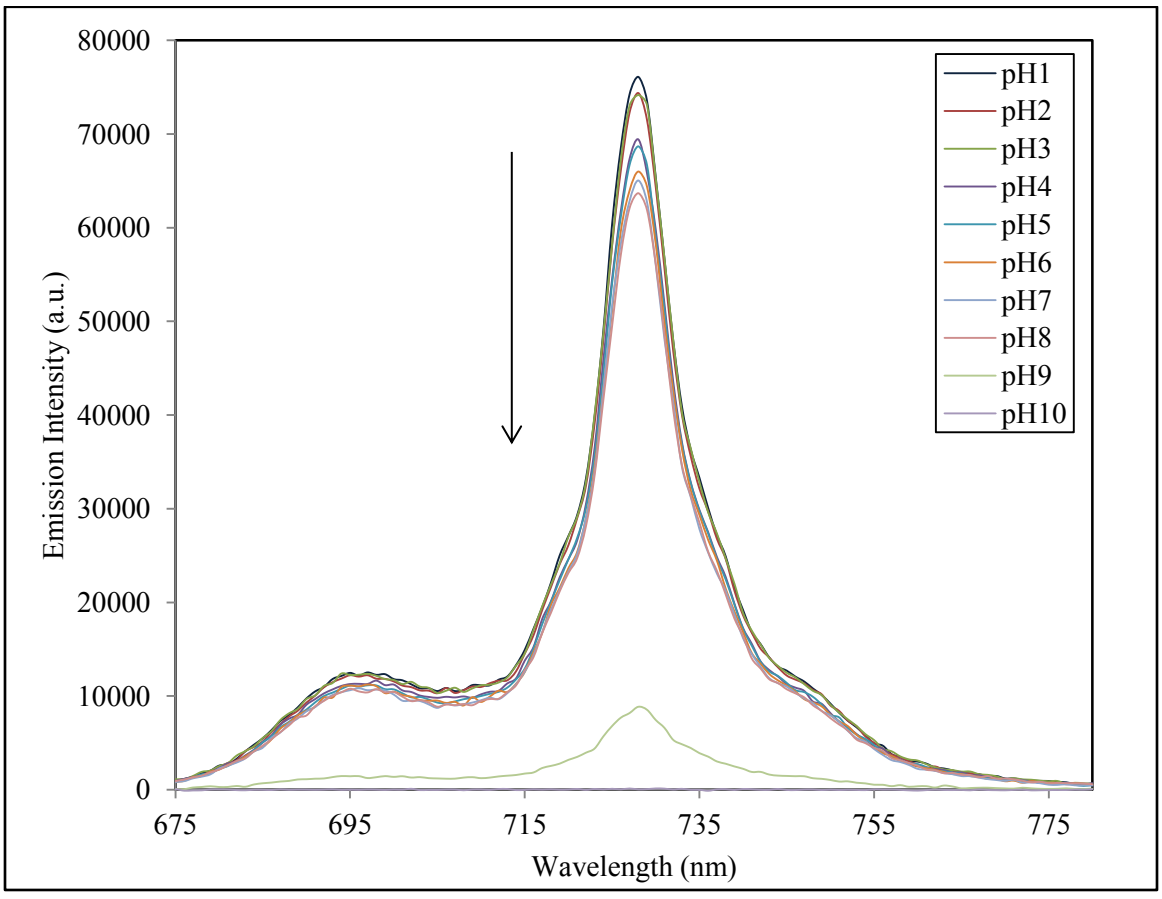

Figure 52. Emission spectra of pH titration of [Cr(phen)$_2$(dpp)]$^{3+}$, λ_{ex}=400nm.

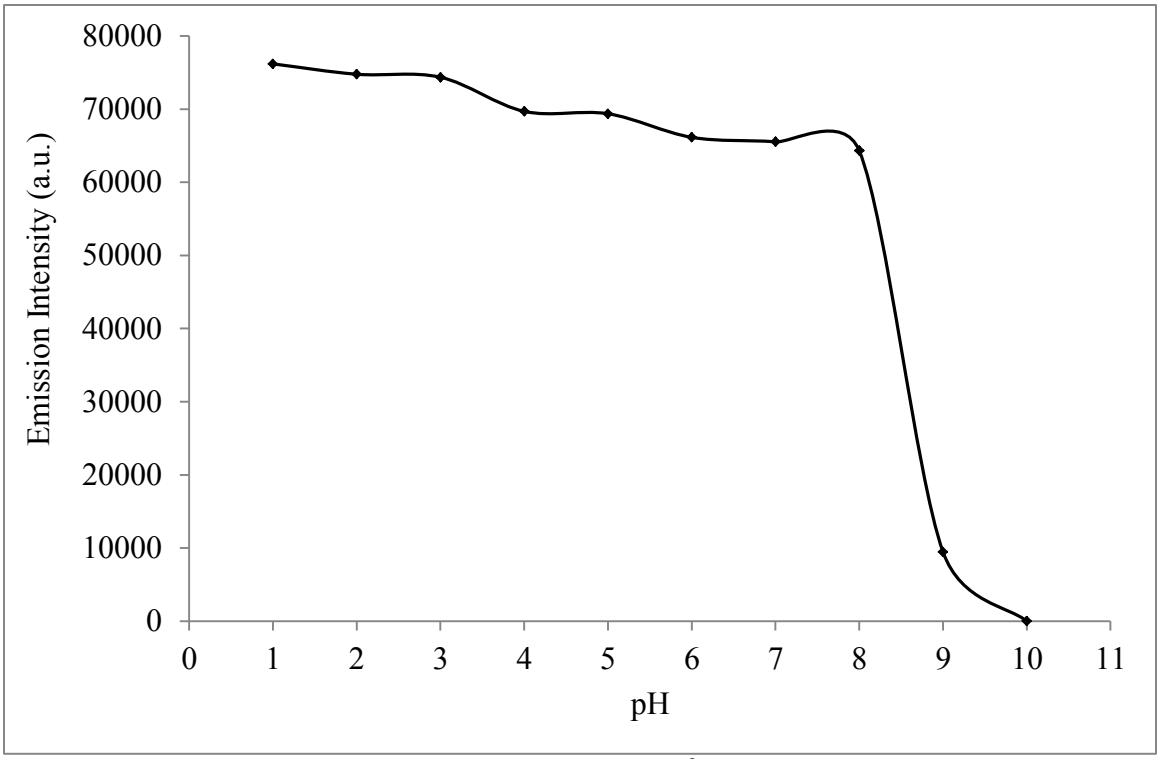

Figure 53. Emission titration plot of $[Cr(phen)_2dpp]^{3+}$ monitored at 728nm.

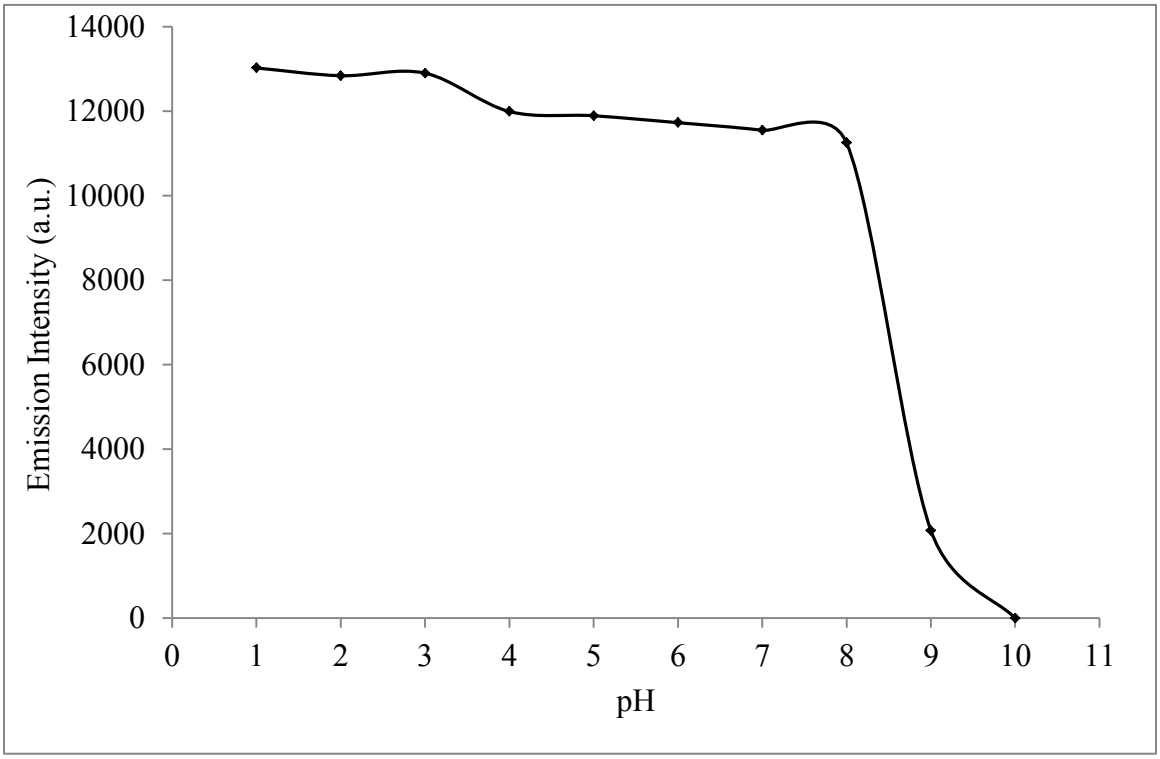

Figure 54. Emission titration plot of $[Cr(phen)_2dpp]^{3+}$ monitored at 695nm.

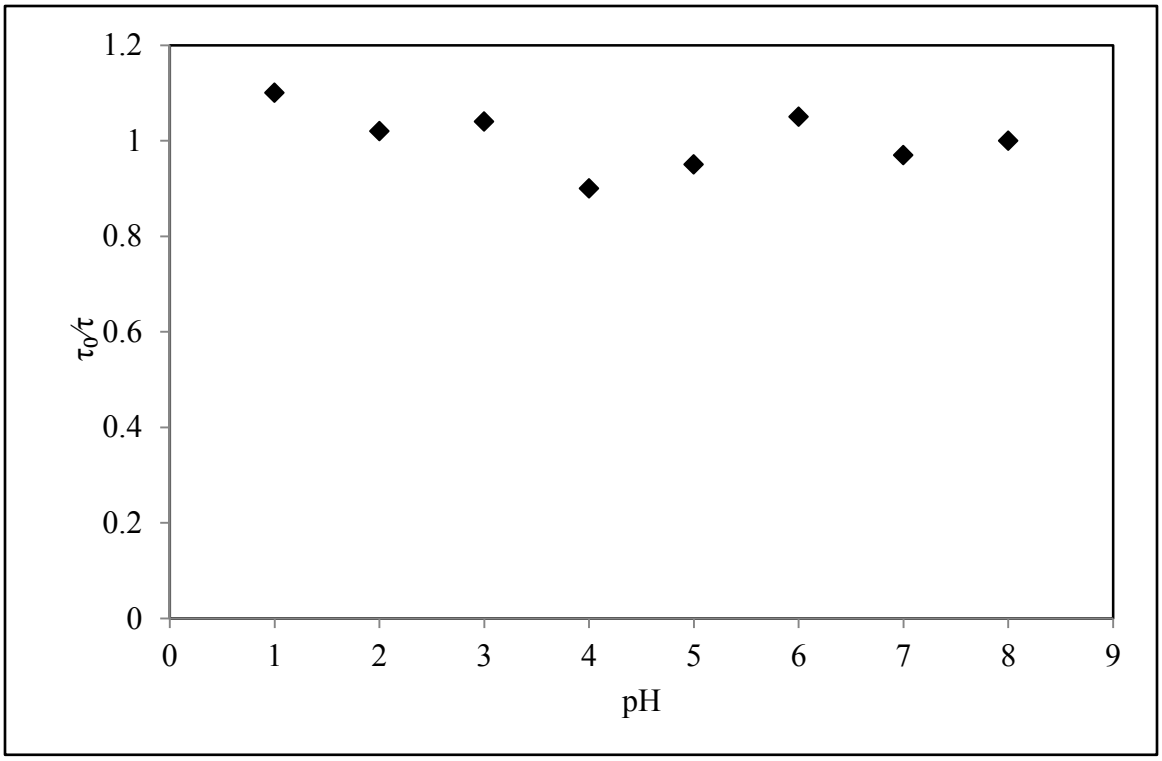

Figure 55. Emission lifetime data, (τ_o/τ), vs. pH for $[Cr(phen)_2dpp]^{3+}$.

The absorption spectra of $[Cr(phen)_2(dpp)]^{3+}$ going from pH1 to pH10 is shown in Figures 56 and 57. At wavelengths 307 and 311 nm, a gradual decrease in absorbance occurs, while at the 281 nm, an increase in absorbance occurs, showing the presence of an isosbestic point at approximately 290 nm. Titration curve plots with absorbances monitored at 307nm and 281nm are shown in figures 58 and 59 respectively. Both of them show at inflection point occurring roughly at pH=5. In Figure 57 the absorption spectra of the chromium(III) complex is shown between wavelengths 370nm and 500 nm, these absorptions correspond to the d-d transitions; there is a noticeable increase in the absorbance at wavelengths 400 nm and 430 nm between pH1- pH2 and pH3- pH10.

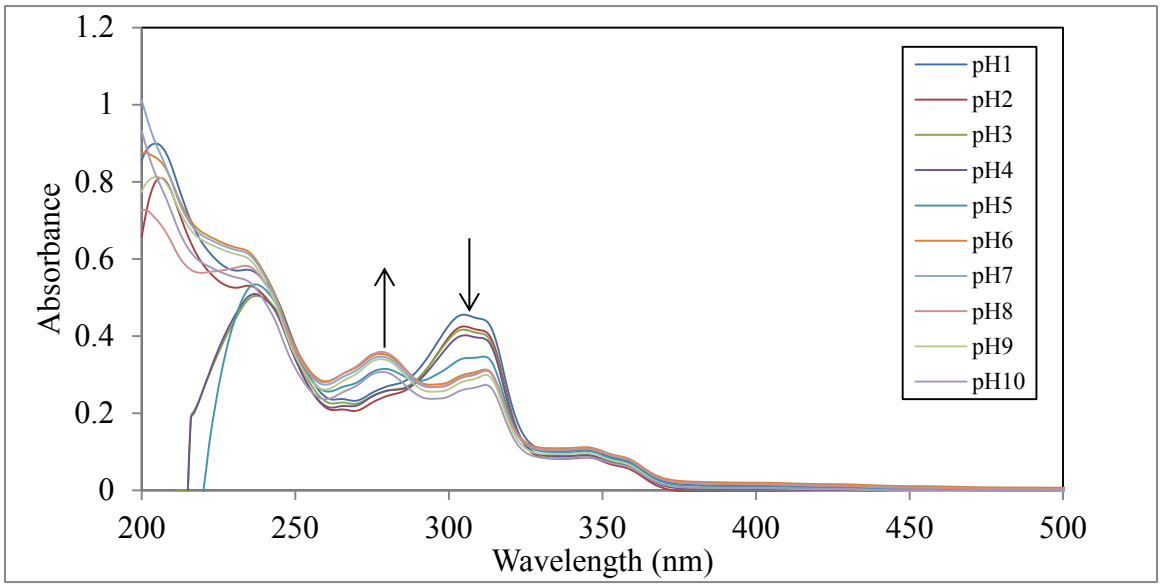

Figure 56. Absorption spectra of pH titration for $[Cr(phen)_2(dpp)]^{3+}$.

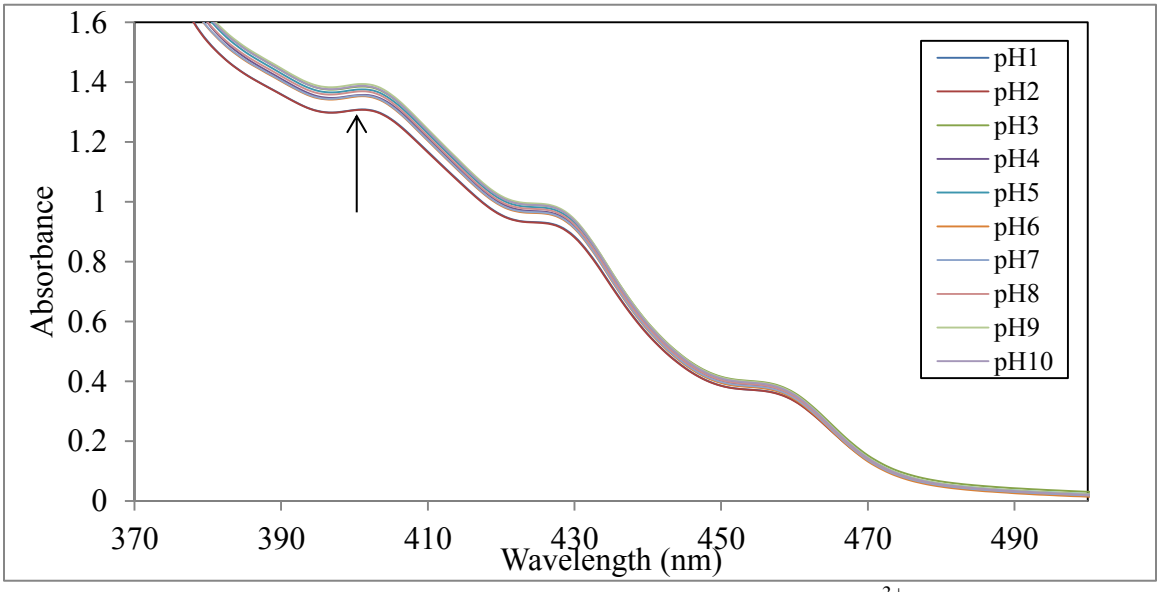

Figure 57. Absorption spectra of pH titration of $[Cr(phen)_2(dpp)]^{3+}$using concentrated samples between wavelengths 370 and 500nm.

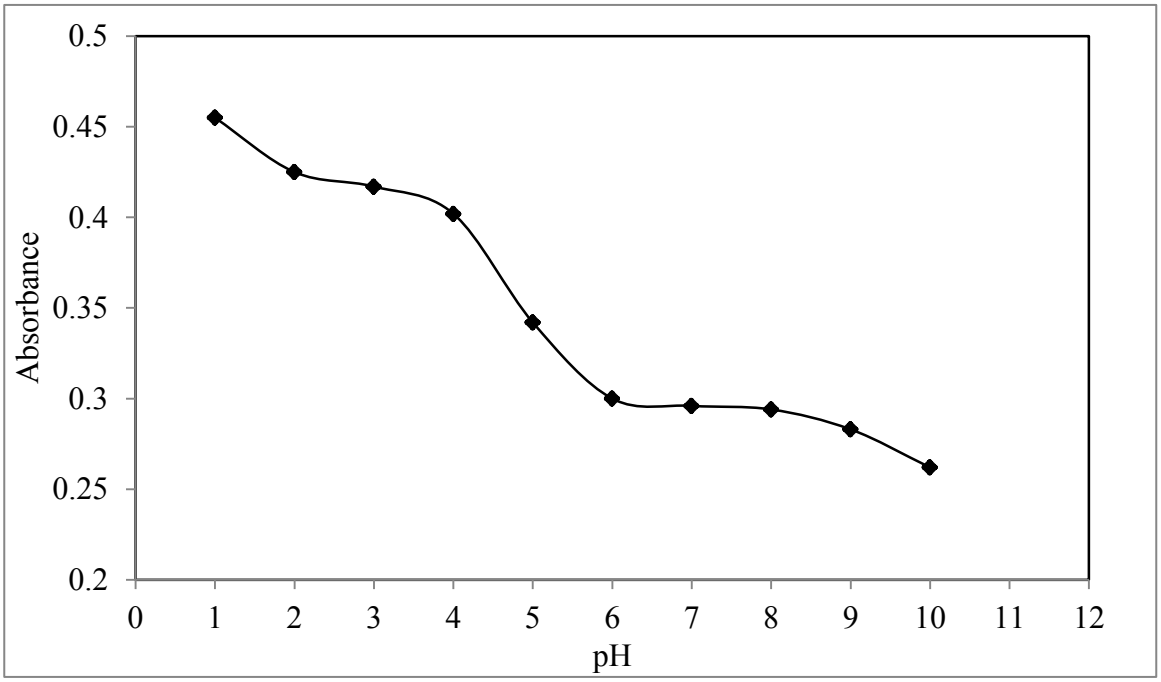

Figure 58. Absorption titration curve for $[Cr(phen)_2(dpp)]^{3+}$ with absorbance monitored at 307 nm.

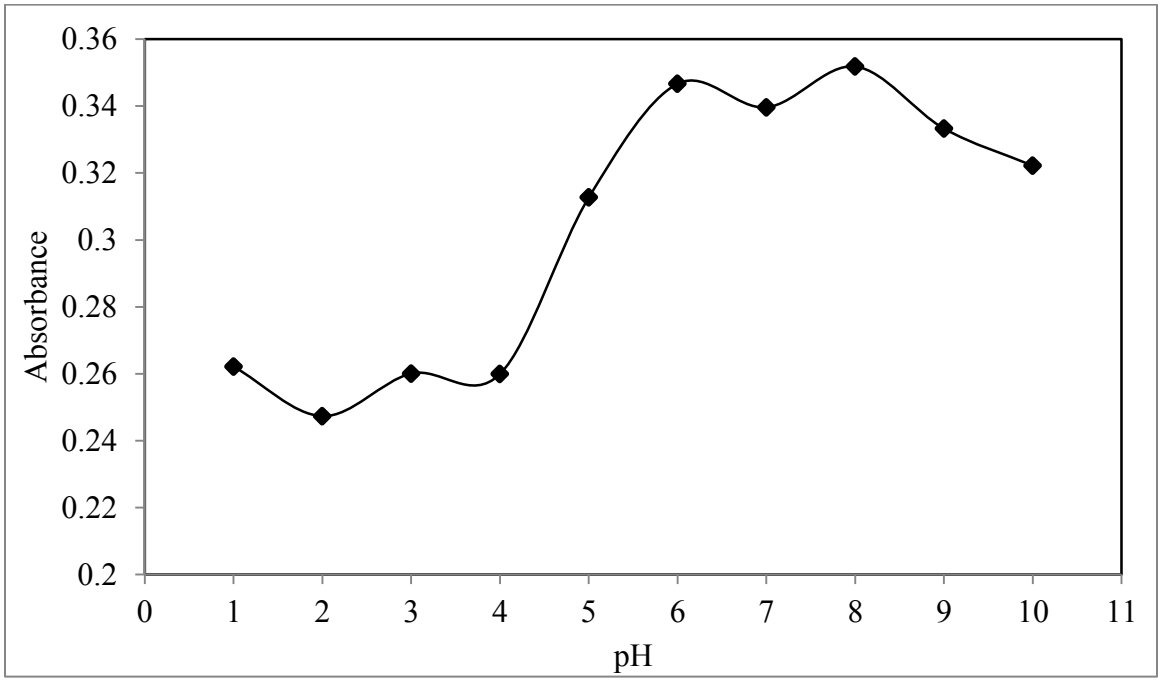

Figure 59. Absorption titration curve for $[Cr(phen)_2(dpp)]^{3+}$ with absorbance monitored at 281 nm.

3. E.2. Emission Spectra of $[Cr(bpy)_2(dpp)]^{3+}$

The emission of $[Cr(bpy)_2(dpp)]^{3+}$ monitored in buffer solutions ranging from pH1 to pH11 is shown in Figure 60. Both the phosphorescence and fluorescence are gradually decreasing with increasing pH, with a dramatic decrease in intensity at pH10 and with complete quenching occurring at pH11. A pH titration plot of the phosphorescence at 726 nm and fluorescence at 695nm show an inflection point at approximately pH9.5 (Figures 61 and 62). For each solution the lifetime of phosphorescence was recorded. The lifetime remained relatively constant at 327±11 μs, suggesting that static quenching is occurring (Figure 63).

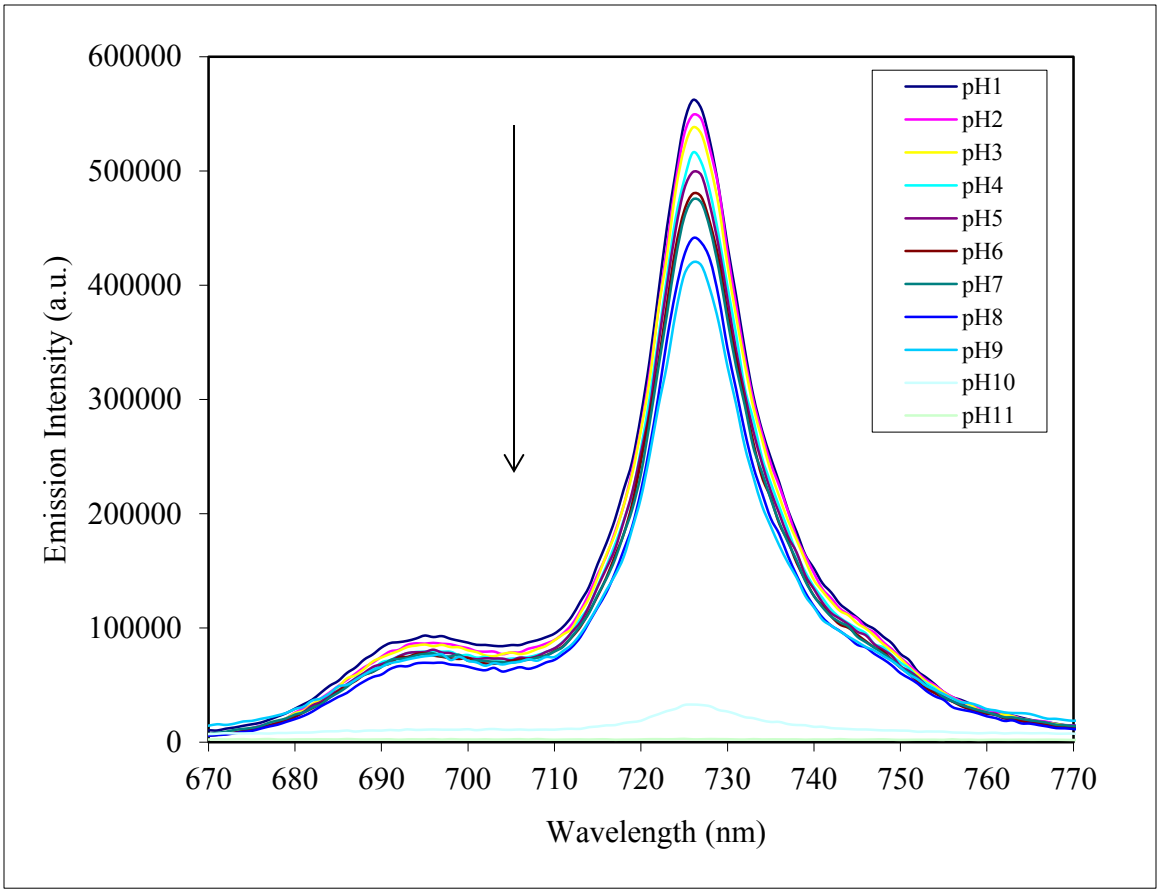

Figure 60. Emission spectra of pH titration of $[Cr(bpy)_2(dpp)]^{3+}$, λ_{ex}=400nm (r.t.).

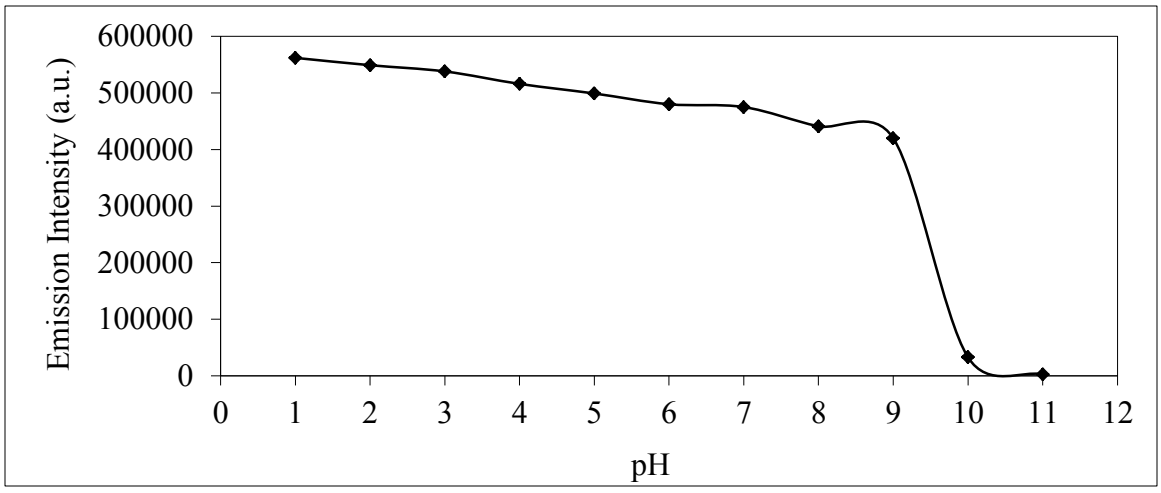

Figure 61. Emission titration plot of $[Cr(bpy)_2dpp]^{3+}$ monitored at 726nm.

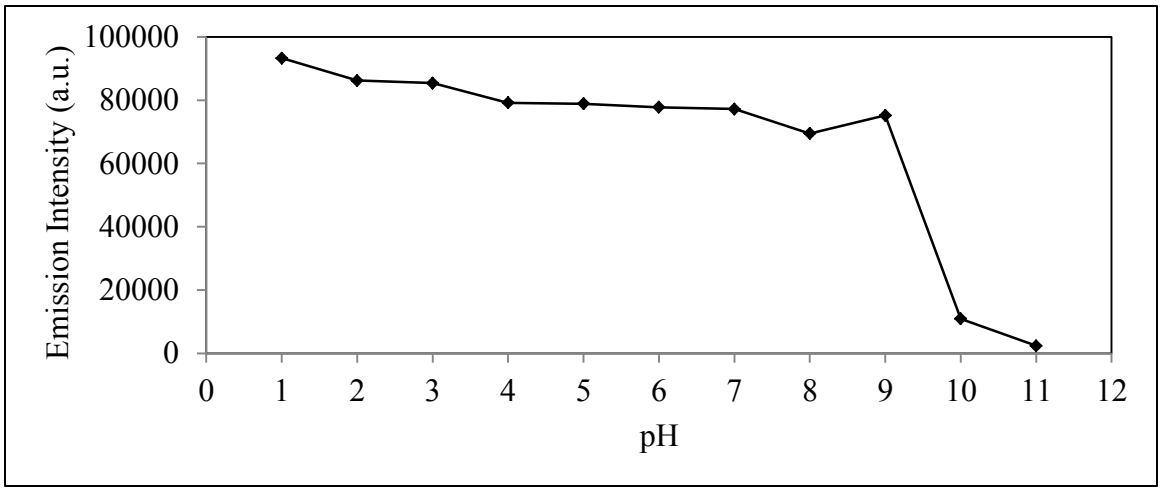

Figure 62. Emission titration plot of $[Cr(bpy)_2dpp]^{3+}$ monitored at 695nm.

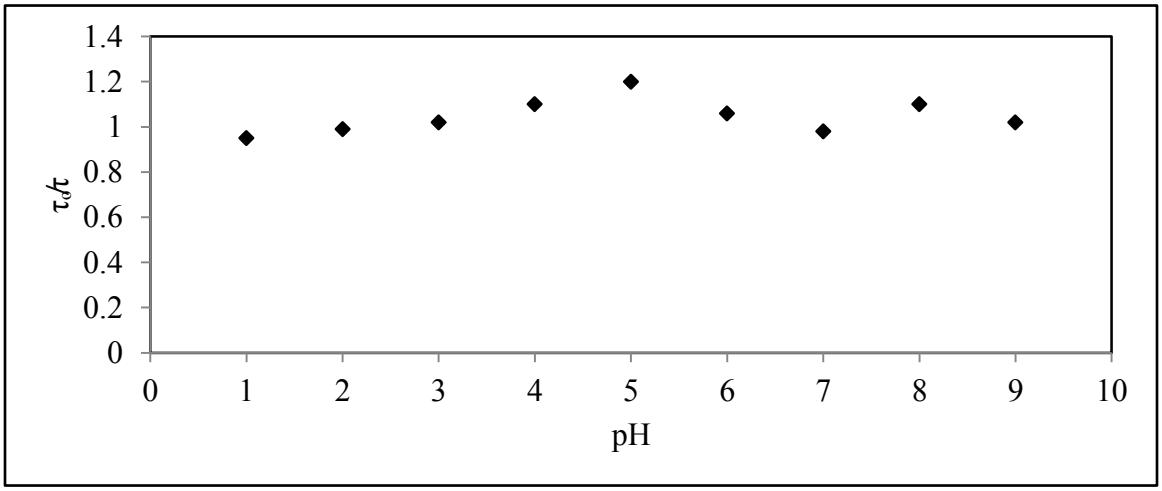

Figure 63. Emission lifetime data, (τ_o/τ), vs. pH for $[Cr(bpy)_2dpp]^{3+}$.

3. E.3. Emission Spectra of $[Cr(phen)_2(dpp)]^{3+}$ with NaOH titration

The emission quenching of the d-d phosphorescence of $[Cr(phen)_2(dpp)]^{3+}$ was further investigated with a sodium hydroxide titration. Six solutions of $5.2x10^{-5}$M $[Cr(phen)_2(dpp)]^{3+}$ were made and in each a small amount of sodium hydroxide was added (1μL) ranging from 0.01M to 0.1M . For each deareated sample the lifetime was measured. As seen in Figure 64 the both the phosphorescent and fluorescent emissions are being quenched by the hydroxide ion. Stern-Volmer plots are presented in Figure 65.

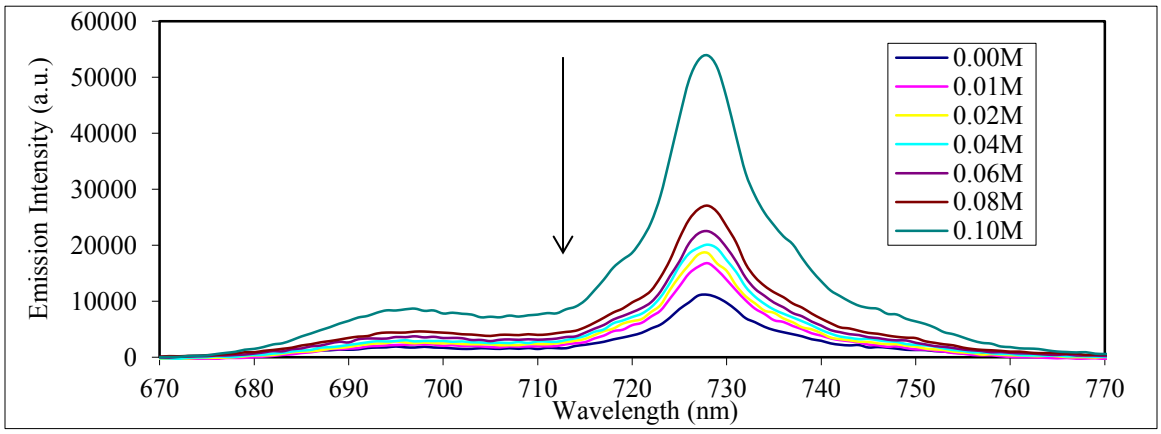

Figure 64. Emission spectra of $[OH^-]$ titration of $[Cr(phen)_2(dpp)]^{3+}$, λ_{ex}=400nm (r.t.).

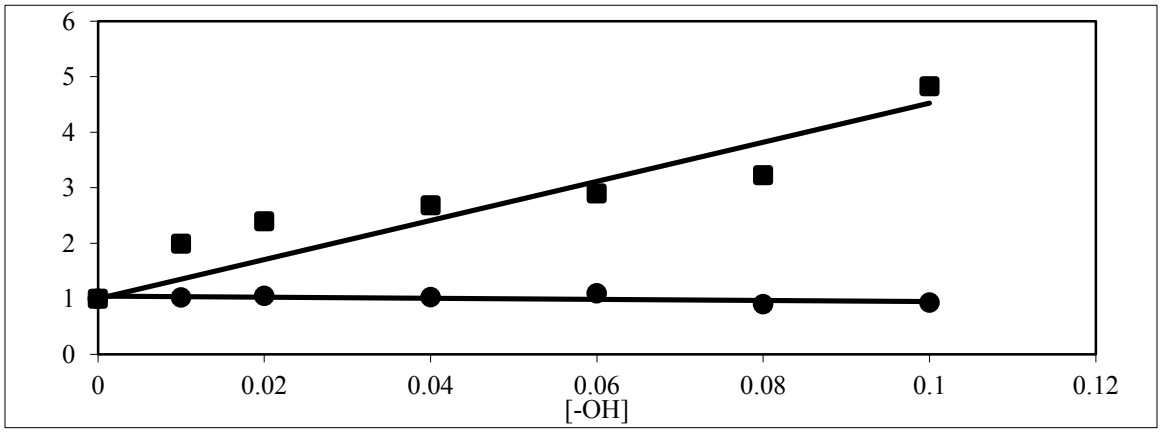

Figure 65. Stern–Volmer plots for emission quenching of a deareated 2.5×10^{-4} M solution of $Cr(phen)_2(dpp)^{3+}$ by hydroxide ions (λ_{ex} = 400nm): (■) steady-state emission intensity data, (Φ_o/Φ); (●) emission lifetime data, (τ_o/τ). Temperature = 25 °C.

3. E.4. Absorption and Emission Spectra of [Rh(bpy)$_2$(dpp)]$^{3+}$

The emission of [Rh(bpy)$_2$(dpp)]$^{3+}$ monitored in buffer solutions ranging from pH of one to pH of twelve is shown in Figure 67. The emission intensity decreases with decreasing pH. A careful look at the emission in the 2 to 7 pH range shows a slight blue-shift of the emission maximum. At pH = 2 the emission maximum occurs at 438 nm, and at pH8-9 it shifts to longer wavelengths with a maximum close to 448 nm. A dramatic increase in intensity with a concomitant slight red-shift of the emission maximum is occurring at pH10 though pH12. A pH titration plot of the emission at 448 nm shows an inflection point at approximately pH9.5 (Figures 68).

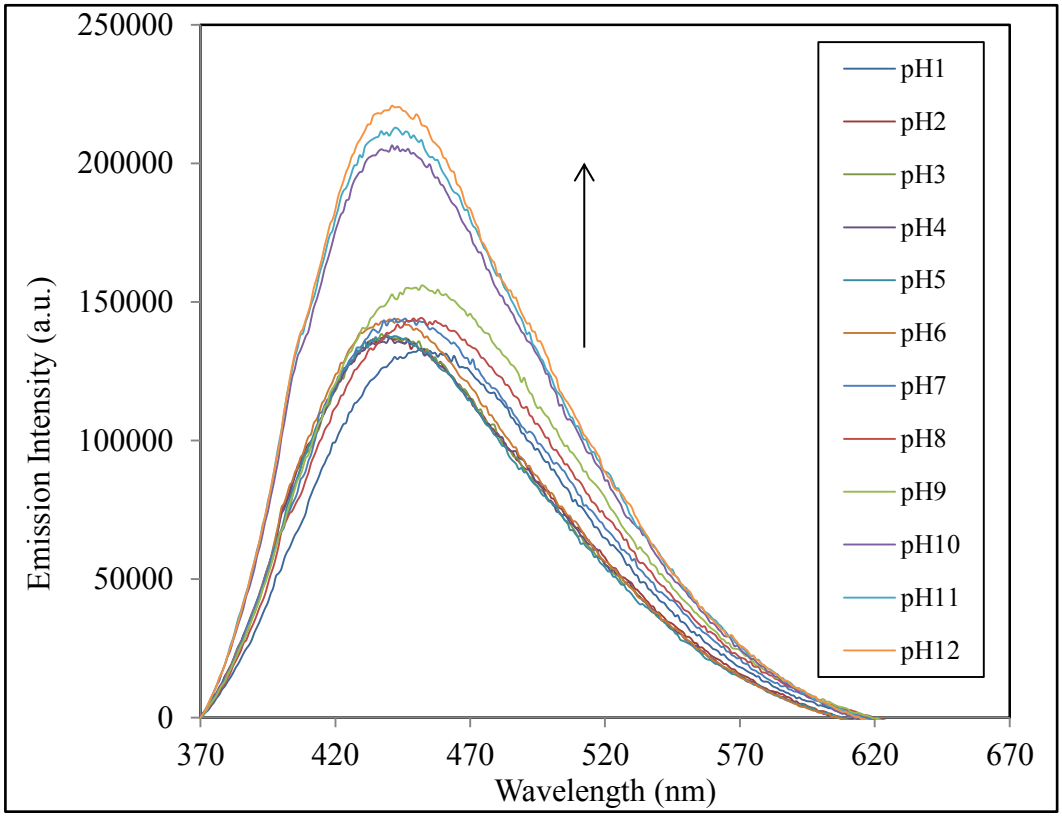

Figure 67. Emission spectra of pH titration of [Rh(bpy)$_2$(dpp)]$^{3+}$ (r.t.).

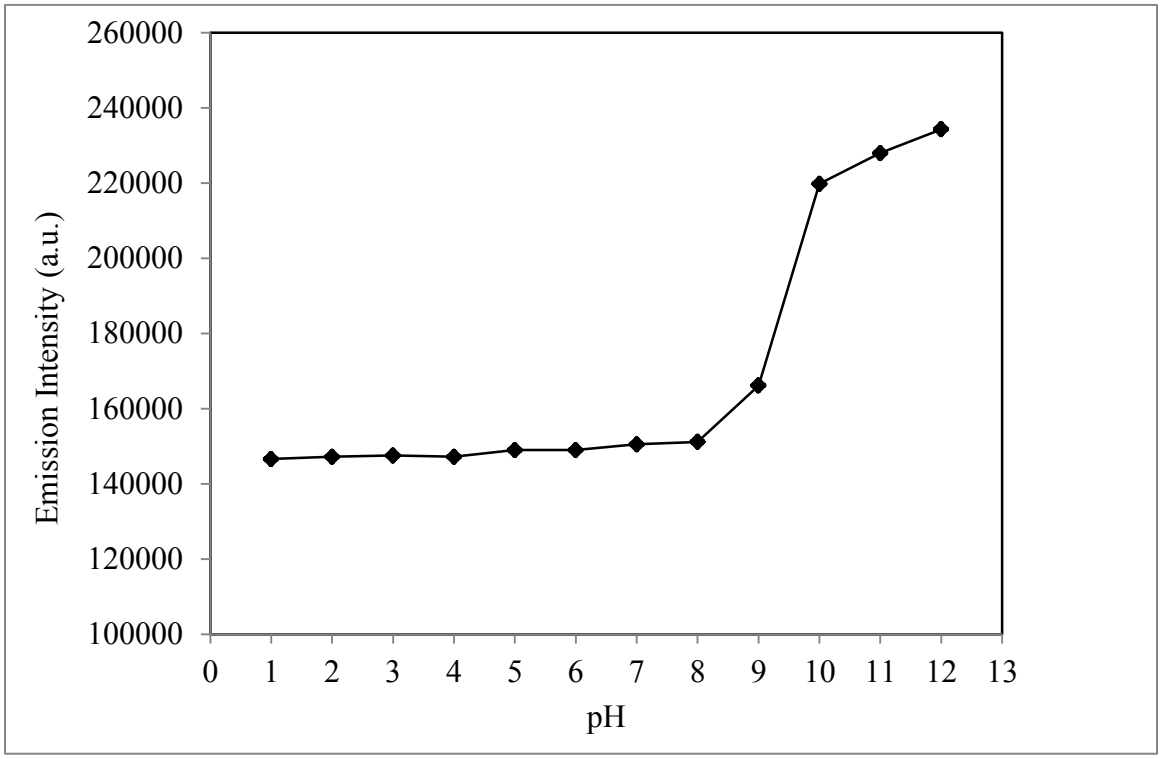

Figure 68. Emission titration curve for $[Rh(bpy)_2(dpp)]^{3+}$ with emission monitored at 448 nm.

The absorption spectra of $[Rh(bpy)_2(dpp)]^{3+}$ going from pH1 to pH12 is shown in Figure 69. At wavelengths 306 and 320 nm, a gradual increase in absorbance in occurring, while at wavelength 284 nm a decrease is occurring. Titration curve plots with absorbances monitored at 306nm and 284nm are shown in figures 70 and 71 respectively. Both show an inflection point occurring roughly at pH8.5.

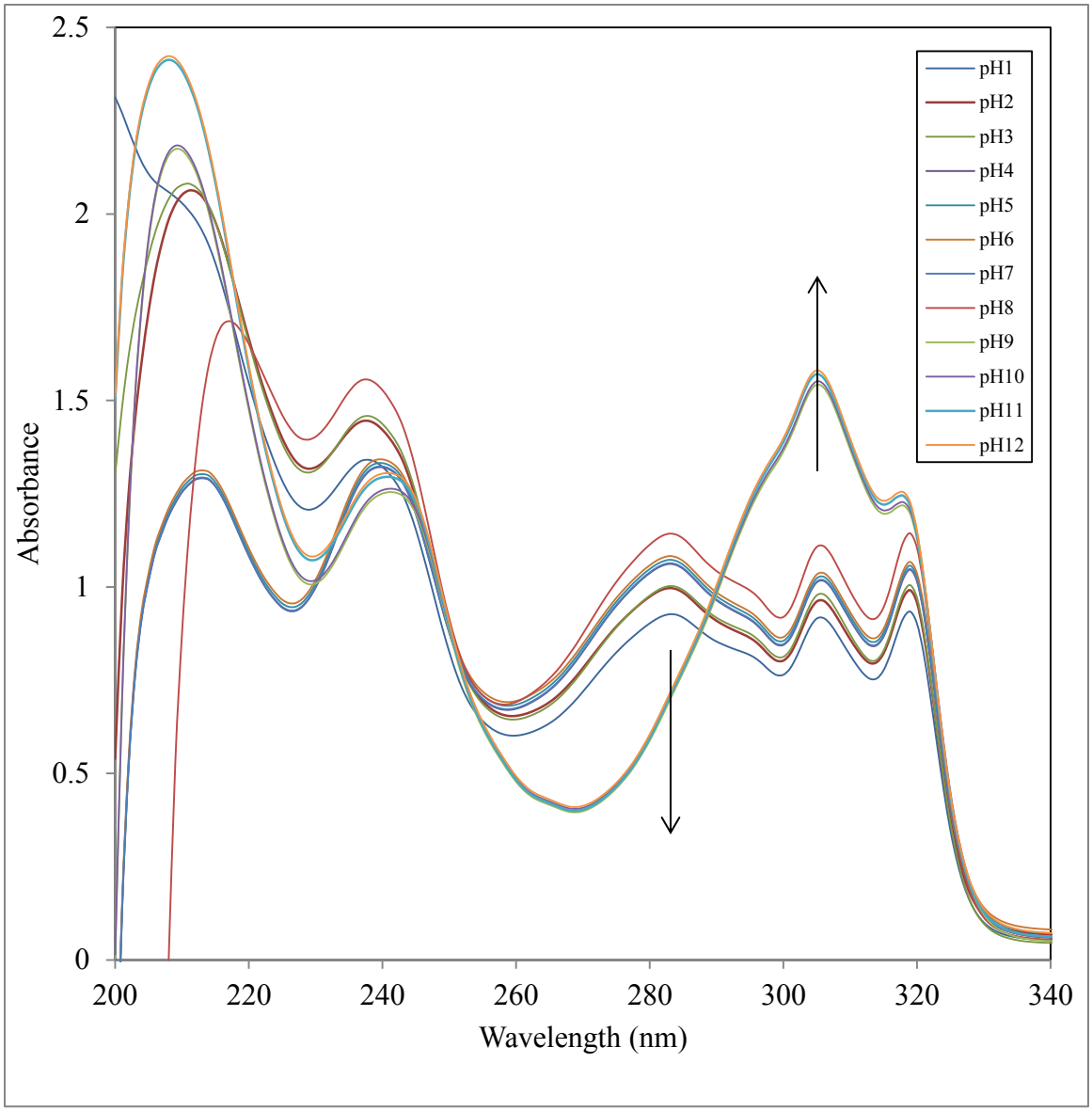

Figure 69. Absorption spectra of pH titration of $[Rh(bpy)_2(dpp)]^{3+}$ (r.t.).

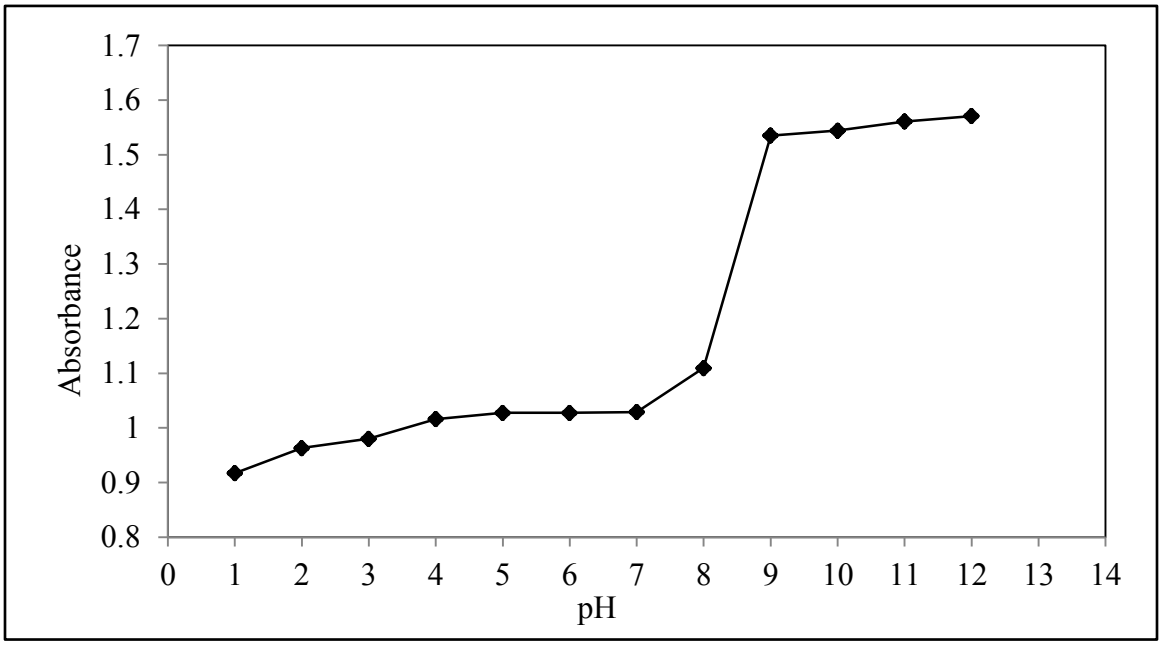

Figure 70. Absorption titration curve for $[Rh(bpy)_2(dpp)]^{3+}$ with absorbance monitored at 306 nm.

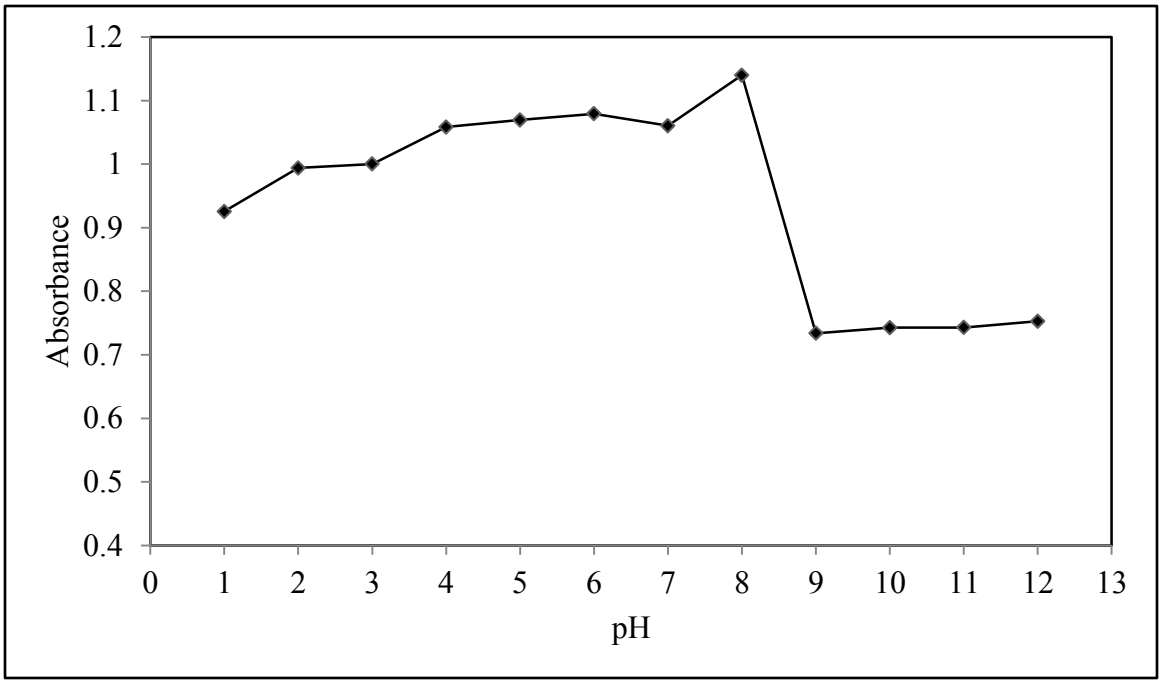

Figure 71. Absorption titration curve for $[Rh(bpy)_2(dpp)]^{3+}$ with absorbance monitored at 284 nm.

3. F. Electronic Spectroscopy of $[Ru(bpy)_2(dpp)](NO_3)_3$

The absorption and emission spectra of $[Ru(bpy)_2(dpp)]^{2+}$ appear in Figures 72 and 73. Similar to the original published report,[103] two clear MLCT transitions are evident in the 400-500 nm range of the absorption spectrum at 426 nm and 484 nm with molar extinction coefficients of 11452 M^{-1} cm^{-1} and 10990 $M^{-1}cm^{-1}$ respectively. The transition at 426 nm is assigned to the bpy localized MLCT ligand, whereas the 484 nm is assigned to the dpp localized MLCT ligand. Several more intense, $\pi \rightarrow \pi^*$ transitions are also evident in the UV range.

The complex yields a broad emission, with a wavelength maximum at 683 nm in water (Figure 73). The emission is not wavelength dependent: excitation throughout the MLCT transition region consistently results in the 683 nm emission. The excitation spectrum, shown in Figure 74, confirms that the emission arises solely from the lower energy transition, with maximum excitation occurring at 468 nm. Its assignment is thus $d \rightarrow \pi^*$ charge transfer the dpp ligand.

The time-resolved spectrum of $[Ru(bpy)_2(dpp)]^{2+}$ was examined using the ICCD camera system. The full time-resolved three-dimensional spectrum is shown in Figure 75. The trace at the maximum emission intensity (683 nm) going from time zero (T_o) onwards, Figure 76, includes the grow-in of the emission. Fitting just the decay portion using IGOR led to a single exponential decay with a lifetime of 203 ± 4 ns (Figure 76). Measuring the lifetime at various wavelengths yields exactly the same lifetime as the 683 nm wavelength, establishing that the lifetime of the $[Ru(bpy)_2(dpp)]^{2+}$ complex is wavelength independent.

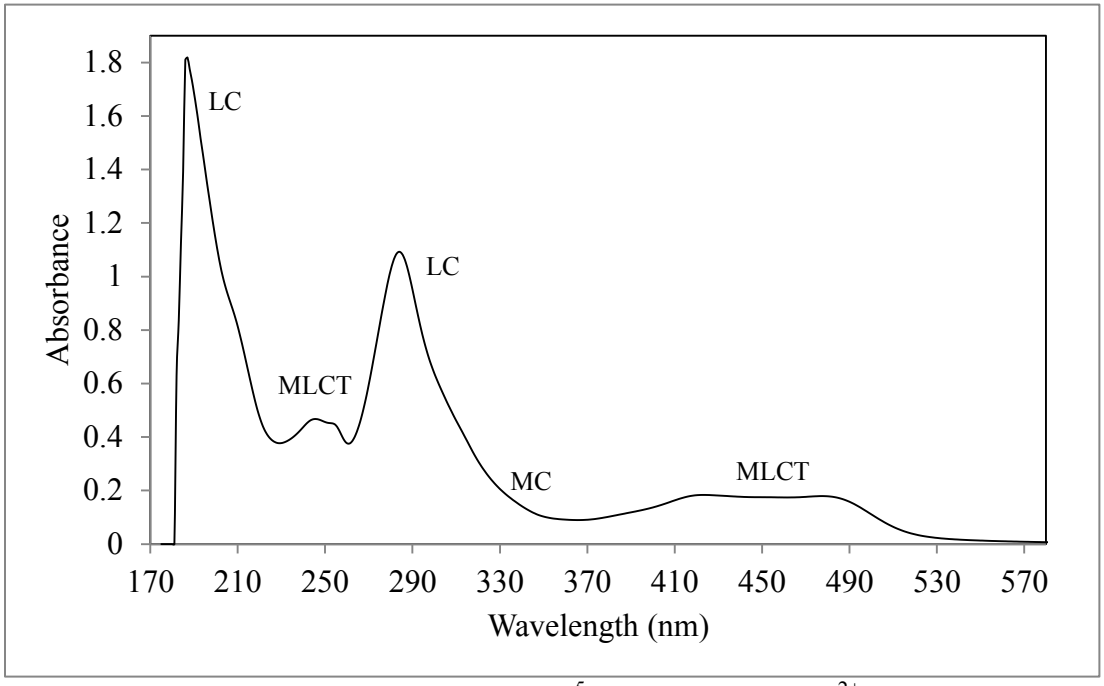

Figure 72. Absorption spectrum of 1.6 x 10^{-5} M $[Ru(bpy)_2(dpp)]^{2+}$ (r.t.).

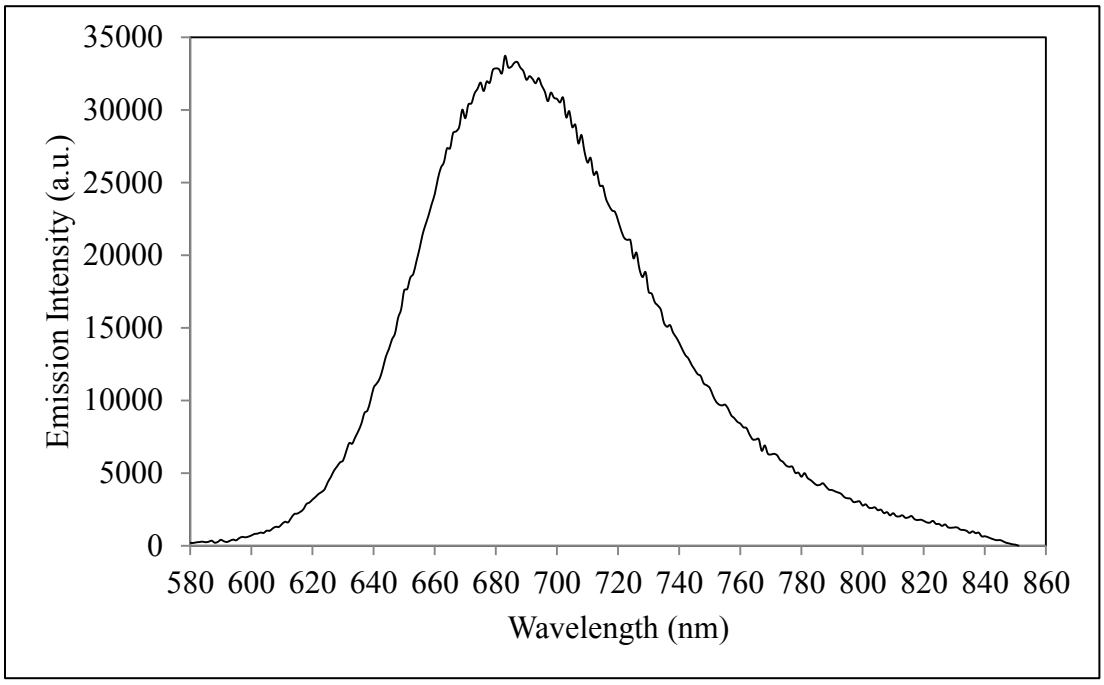

Figure 73. Emission spectrum of 1.6 x 10^{-5} M $[Ru(bpy)_2(dpp)]^{2+}$ (r.t.).

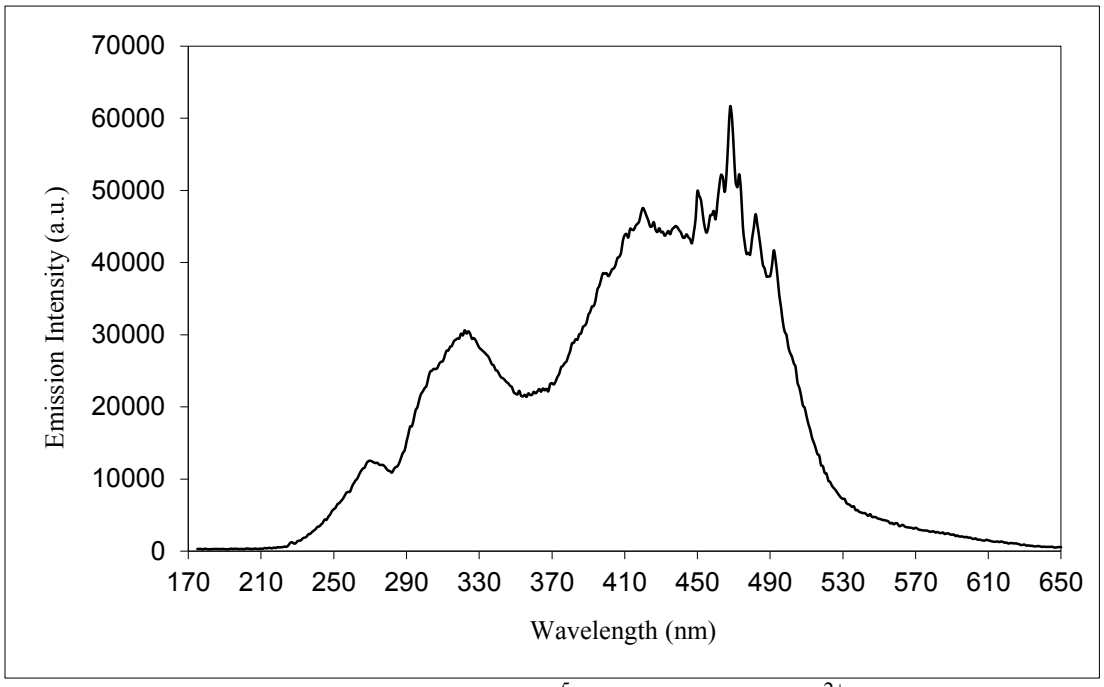

Figure 74. Excitation spectrum of 1.6 x 10^{-5} M $[Ru(bpy)_2(dpp)]^{2+}$, $\lambda_{ex.}$=683nm (r.t.).

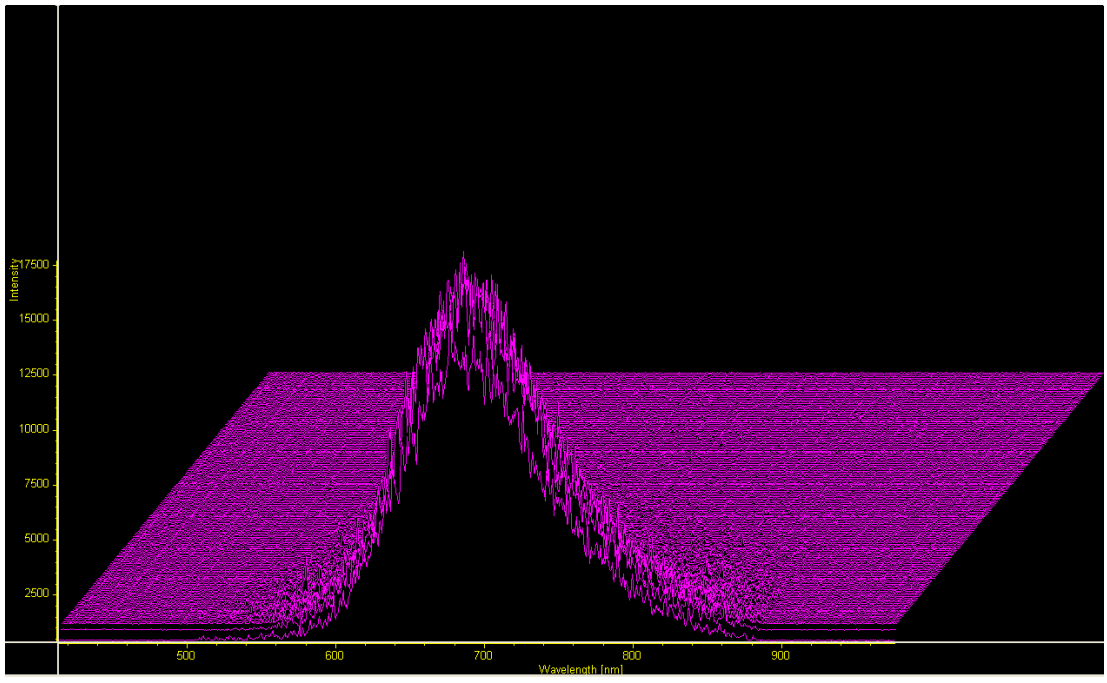

Figure 75. 3D time-resolved emission spectrum of 1.6 x 10-5 M $[Ru(bpy)_2(dpp)]^{2+}$(r.t.).

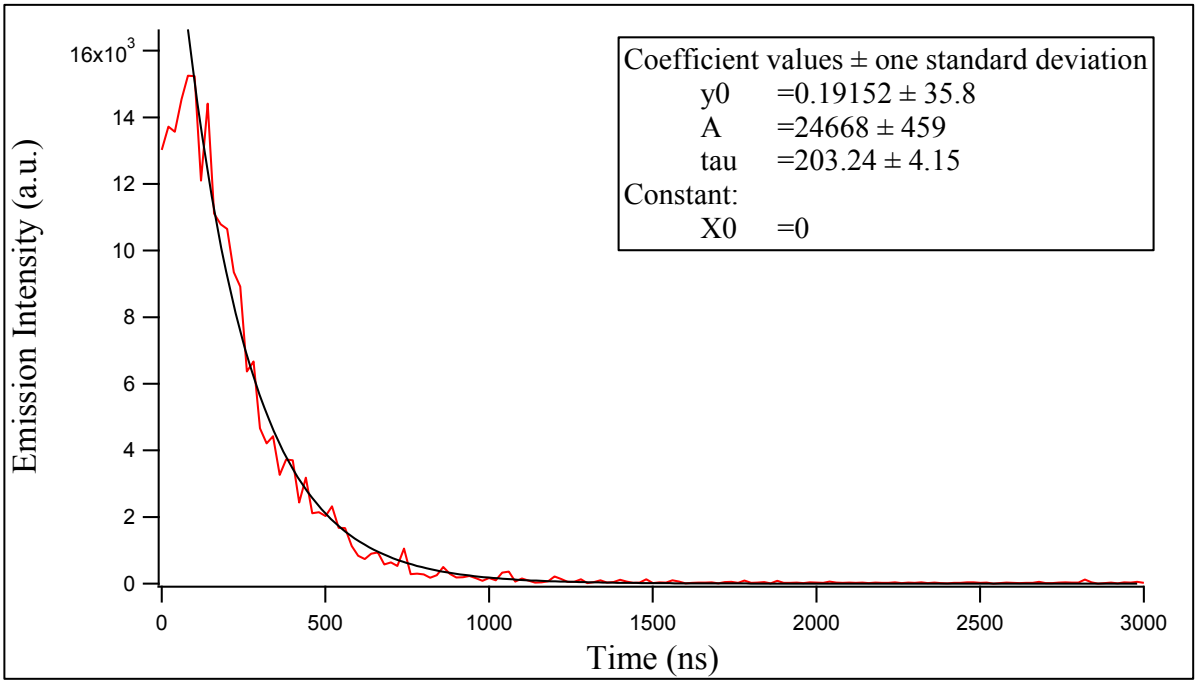

Figure 76. Time-resolved emission spectra of $[Ru(bpy)_2(dpp)]^{2+}$ showing full trace with fit at 683 nm.

CHAPTER 4

4. DISCUSSION

4. A. SYNTHESIS OF CHROMIUM (III) AND RHODIUM (III) POLYPYRIDINE COMPLEXES

A significant amount of time was invested in understanding and mastering synthetic and purification procedures and techniques. Trying to adopt existing synthetic preparations available in literature to synthesize analogous complexes is challenging to say the least. When things do not go as expected trying to understand and to decipher what went wrong and how to make things right is a time consuming and tedious process.

Synthesis of the $[Cr(bpy)_2dpp]^{3+}$ proved difficult and problematic due to the tendency of chromium-bpy complexes to undergo ligand scrambling reactions; a fact that was discovered later on by reading Basolo and Pearson[9]. In order to avoid ligand scrambling, phen was used instead of bpy since it appears to have a much higher formation constant[9].

One of the most invaluable and important synthetic tools employed in the synthesis of the chromium (III) complexes was the usage of trifluoromethanesulfonic acid (Figure 77). Trifluoromethanesulfonic acid, also known as triflic acid, is a sulfonic acid with the chemical formula CF_3SO_3H. It is one of the strongest acids, with a $K_a = 8.0\times10^{14}$ ($pK_a \sim -15$), which qualifies it as a superacid. Triflic acid is a hygroscopic, colorless liquid at room temperature, and it is soluble in polar solvents such as DMF, and acetonitrile. Triflic acid owes many of its useful properties to its great thermal and chemical stability. The trifluoromethanesulfonyl group (CF_3SO_2), by virtue of the large

inductive effect of the trifluoromethyl group, is one of the strongest electron-withdrawing groups known. Consequently, the trifluoromethanesulfonate anion ($CF_3SO_3^-$) has found use as an excellent leaving group in nucleophilic substitution reactions in organic chemistry and acts as a unidentate ligand in inorganic coordination chemistry.[15]

The synthesis of the rhodium (III) complexes proved to be more straight forward than that of the chromium (III) complexes. However, their synthesis did required longer reflux times and extensive column chromatography to purify them. Chromium and Rhodium complexes were analyzed for carbon, hydrogen and nitrogen composition by Galbraith Laboratories. (Table 5)

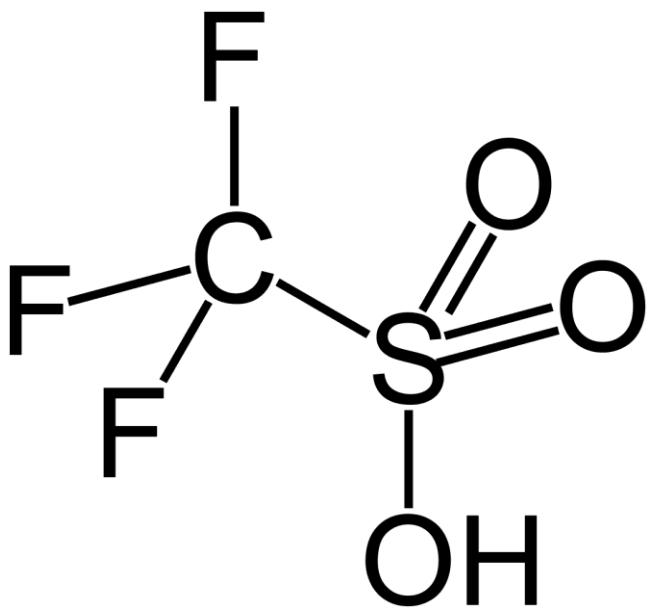

Figure 77. Chemical structure of Trifluoromethanesulfonic acid.

TABLE 5. Elemental analysis of Chromium and Rhodium complexes

Compound	Calculated	Found
$[Cr(phen)_2dpp]\ (CF_3SO_3)_3$ $CrC_{41}H_{26}N_8F_9S_3O_9$	C, 43.55; H, 2.30; N, 9.91	C, 43.23; H, 2.27; N, 9.83%.
$[Cr(bpy)_2dpp](PF_6)_3$ $CrC_{34}H_{26}N_8P_3F_{18}$	C, 39.50; H, 2.52; N, 10.83	C, 39.10; H, 2.61; N, 10.54%.
$[Rh(bpy)_3](PF_6)_3$ $C_{30}H_{24}N_6RhF_{18}P_3$	C, 35.78; H, 2.36; N, 8.35	C, 35.74; H, 2.41; N, 8.28%.
$[Rh(bpy)_2dpp](PF_6)_3$ $C_{34}H_{26}N_8RhF_{18}P_3$	C, 37.62; H, 2.40; N, 10.32	C, 37.59; H, 2.35; N, 10.21%

4. B. 1. ABSORPTION AND EMISSION SPECTRA OF $[Cr(phen)_{2(}dpp)]^{3+}$ and $Cr(bpy)_{2(}dpp)]^{3+}$

The shorthand electronic configuration of the Cr(III) ion is $[Ar]3d^3$. In its octahedral (O_h) complexes, the degeneracy of the chromium *d* orbitals is lifted, resulting in two orbital subsets of t_{2g} and e_g symmetry. The $^4A_{2g}$ ground state has the electronic configuration $(t_{2g})^3$, with the *d* orbitals filled with one electron in each of the t_{2g} orbitals, according to Hund's Rule. Two excited states with $(t_{2g})^2(e_g)^1$ electronic configuration result from promotion of a t_{2g} electron to an e_g orbital while preserving electronic spin. Six such spin-allowed promotions are possible, which in O_h symmetry are divided into two sets differing in the magnitude of the interelectronic repulsion terms. The related quartet excited states generated are labeled $^4T_{2g}$ and $^4T_{1g}$. For almost all octahedral Cr(III) complexes studied, the two lowest-lying excited states are the $^2T_{1g}$ and ^2E_g levels of the $(t_{2g})^3$ electronic configuration, where spin-pairing has occurred within the t_{2g}

subshell. A qualitative orbital energy level diagram depicting the electron occupation of the relevant electronic ground and excited states discussed above is provided in Figure78.

An energy level diagram for octahedral Cr(III) compounds is presented in Figure 80. Consistent with this diagram, for the majority of Cr(III) complexes the ^2E_g state has the lower energy of the two doublet excited states [1,2]. The ground $^4A_{2g}$ level and the three lowest doublet levels, ^2E_g, $^2T_{1g}$, and $^2T_{2g}$, are derived from the $(t_{2g})^3$ electronic configuration. The lowest excited quartet states, $^4T_{2g}$ and $^4T_{1g}$, are derived from $(t_{2g})^2(e_g)^1$ configuration. The $^4A_{2g}$, ^2E_g, and $^2T_{lg}$ states are independent of the octahedral field strength, Δ_o, while the $^4T_{2g}$ and $^4T_{1g}$, energies are proportional to Δ_o. The ^2E_g and $^2T_{1g}$ states are identical, but the degeneracy can be removed through a configuration interaction. Although the variation of the doublet-state energies with Δ_o is small, the ^2E_g energy does depend upon the interelectronic repulsion (Figure 79). The dominant ligand field bands in the UV-visible absorption spectra are associated with the $^4A_{2g} \rightarrow {}^4T_{2g}$ and $^4A_{2g} \rightarrow {}^4T_{1g}$ transitions, since the corresponding absorptions generating the two doublet excited states are both Laporte and spin multiplicity forbidden (Figures 28 and 80). The spin-allowed absorption bands for the $^4A_{2g} \rightarrow {}^4T_{2g}$ and $^4A_{2g} \rightarrow {}^4T_{1g}$ transitions are broad (Figure 28). This is a consequence of the $^4T_{2g}$ and $^4T_{1g}$ excited states both having an electron residing in an e_g antibonding σ^* orbital (Figure 78), which results in a large nuclear displacement relative to the ground state. For excitation into the higher lying $^4T_{1g}$ level, very fast internal conversion occurs to the $^4T_{2g}$ state with near unit efficiency.[45]

Both $[Cr(phen)_2(dpp)]^{3+}$ and $[Cr(bpy)_2(dpp)]^{3+}$complexes exhibit intense, long-lived $^2E_g \rightarrow {}^4A_{2g}$ phosphorescence spectra in aqueous solutions at room temperature (Figures 30

and 34). The $[Cr(phen)_2(dpp)]^{3+}$ complex shows a maximum emission at 728 nm with a corresponding lifetime of 87μs, whereas the $[Cr(bpy)_2(dpp)]^{3+}$ complex shows a maximum emission at 726 nm with a longer lifetime of 327 μs. The phosphorescence spectra display sharp, highly resolved fine structures, due to the small geometric change that is expected between the $^4A_{2g}$ ground state and ^2E_g excited state, due their common $(t_{2g})^3$ orbital parentage. Another feature of the emission spectra is the very weak $^4T_{2g} \rightarrow {}^4A_{2g}$ fluorescence observed at 695 nm (Figures 30 and 34). This fluorescence emission is weak due to $^4T_{2g} \rightarrow {}^2E_g$ intersystem crossing (ISC) being an unusually rapid process [4, 13–15] and often occurring with high efficiency. A noticeable feature with these types of chromium (III) complexes is a relatively large Stoke's shift. The $^2E_g \rightarrow {}^4A_{2g}$ transition is shifted to substantially longer wavelengths. This lowering of the ^2E_g energy, which is ascribed to reduction of the interelectronic repulsion between the d electrons, is called the nephelauxetic effect. Large decreases in ^2E_g are induced by ligands with low-lying π^* antibonding orbitals that decrease electron repulsion by delocalizing the d electrons onto the ligands.

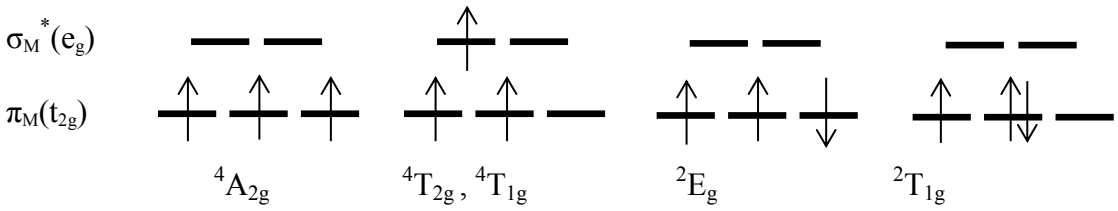

Figure 78. Electronic configurations for d^3 complexes [Cr(III)] in O_h symmetry.

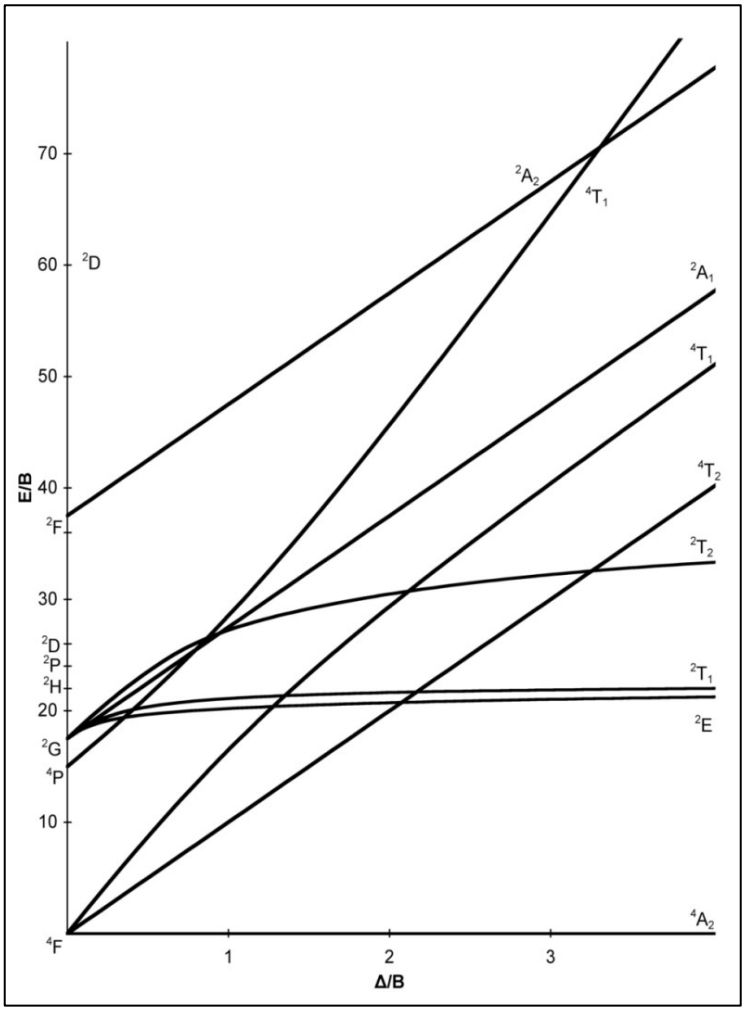

Figure 79. Tanabe-Sugano diagram for d^3 electron configuration.

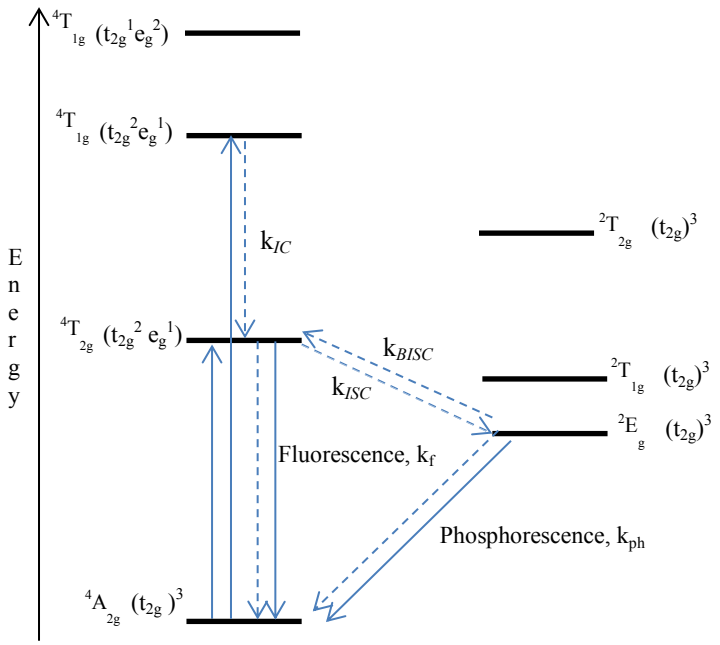

Figure 80. Simplified Jablonski state energy level diagram for O_h Cr(III) complexes, showing the principal processes that may occur subsequent to vertical excitation to a $^4T_{2g}$ or $^4T_{1g}$ Franck–Condon excited state and the rate constants for each of these processes. Full arrows represent radiative processes (absorption or emission), whereas dashed arrows designate radiationless deactivation processes.

4. B. 2. ABSORPTION AND EMISSION SPECTRA OF $[Rh(bpy)_{2(}dpp)]^{3+}$, $Rh(bpy)_3]^{3+}$ and $[Rh(bpy)_2Cl_2]^+$

Although not as popular as other transition metals, e.g., Ruthenium, Rhodium has received considerable attention in the field of inorganic photochemistry. Rhodium (III) polypyridine complexes display photophysical properties of considerable interest, both from a fundamental viewpoint and in terms of the possible applications. In Rhodium (III) polypyridine complexes, the photophysics and photochemistry are determined by the

interplay between LC and MC excited states, with relative energies depending critically on the metal coordination environment. In one the most studied rhodium (III) polypyridine complexes, $[Rh(bpy)_3]^{3+}$, it is generally agreed that the lowest excited state can be classified as a triplet (T_1) being mainly ligand centered (LC) of π-π^* character, while the ground state is a singlet (S_0). However, the metal ion Rh^{3+} with a $4d^6$ electron configuration distinctly influences these states, but its importance is not yet fully clear.

In order to contribute to the understanding of the photophysical behavior of Rh(III) polypyridine complexes, one homoleptic and two heteroleptic complexes of the type cis-$Rh(bpy)_2XY^{n+}$ (X=Y= bpy, n = 3; X=Y= Cl, n = 1; X=Y= dpp, n = 3) were synthesized and studied. The approach is that of using the X and Y ligands to change the energy of the MC states in a predictable way without substantially affecting that of the LC state and to look for qualitative effects of the change in the LC-MC energy difference on the emission properties of these complexes.

The absorption spectrum in aqueous solutions and emission spectrum in 77 K glasses of $[Rh(bpy)_2Cl_2]^+$ are shown in Figure 81 and 82 respectively. The absorption spectrum shows an intense intraligand transition in the ultraviolet region (314 nm) as well as a much lower intensity, longer wavelength shoulder, which suggest ligand field absorption. The emission spectrum shows a broad Gaussian band with maximum at about 675nm. Lifetime measurements gave an exponential decay with relatively short lifetime of 28.3 μs. The spectral properties found for $[Rh(bpy)_2Cl_2]^+$ are in agreement with those previously reported, and these characteristics are consistent with the assignment of this emission to a metal-centered ^{3}d-d phosphorescence.[84]

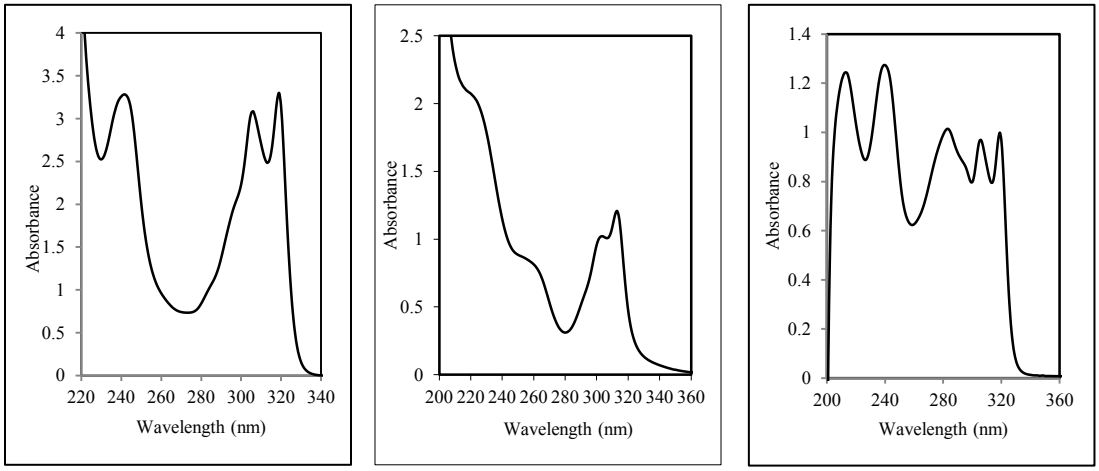

Figure 81. Absorption spectra of $[Rh(bpy)_3]^{3+}$, $[Rh(bpy)_2Cl_2]^{+}$ $[Rh(bpy)_2dpp]^{3+}$ in ethanol-methanol (4:1**,** v/v) r.t. Arranged from left to right.

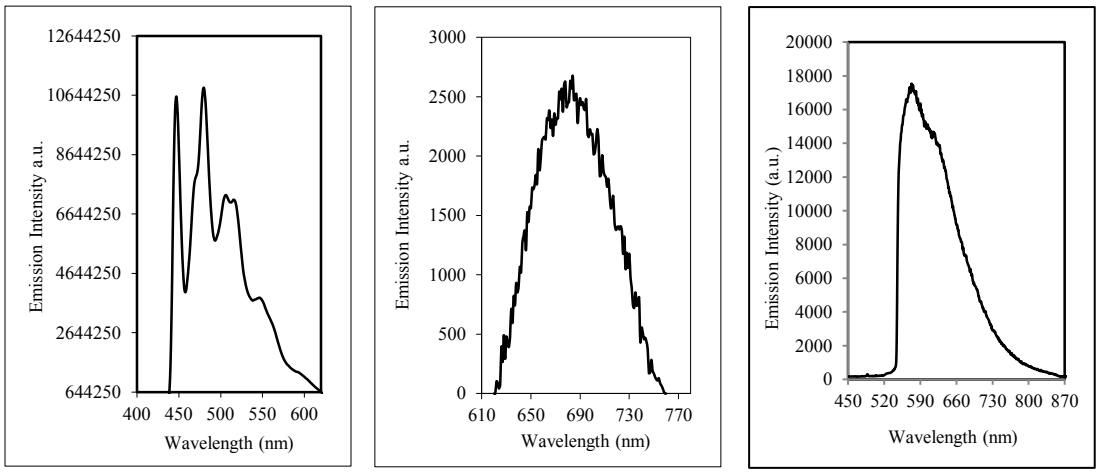

Figure 82. Emission spectra of $[Rh(bpy)_3]^{3+}$ ($\lambda_{ex.}$=319 nm), $[Rh(bpy)_2Cl_2]^{+}$ ($\lambda_{ex.}$=314 nm), $[Rh(bpy)_2dpp]^{3+}$ ($\lambda_{ex.}$=319 nm), in ethanol-methanol (4:1**,** v/v) glass at **77** K. Arranged from left to right.

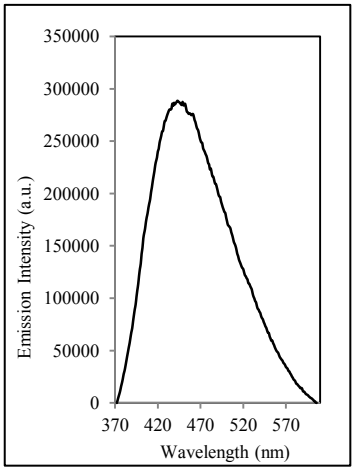

Figure 83. Emission spectrum of $[Rh(bpy)_2dpp]^{3+}$ in ethanol-methanol (4:1**,** v/v) r.t. Excitation wavelength 319 nm.

In contrast to the results seen for the dichloro bis(bpy) rhodium (III) complex, the photophysical properties of the tris(bpy) rhodium (III) complex are dramatically different. In low-temperature glasses, the $[Rh(bpy)_3]^{3+}$ complex displays a long-lived (62 ms) structured emission with the 0-0 transition identified at 479 nm (Figures 38 and 82). The emission from $[Rh(bpy)_3]^{3+}$ is undoubtedly π-π^* in nature. This assignment can be made on the basis of the obvious similarities of both the location and the structure of the phosphorescence band observed from a glass at 77 K to those of the free ligand, although the lifetime is significantly shorter than that of the free ligand (bpy τ = 819 ms). Thus, it is clear that coordination to the metal introduces new radiative pathways to the ground.[72] The π-π^* nature of the emitting state was confirmed by Komada *et al*.[87] he established that excitation is localized on ligands, especially on a single ligand molecule, to produce $^3\pi$-π^* states of ligands that are only slightly perturbed by chelating to Rh(III) ions. Moreover, the shortening of the triplet lifetime in the rhodium complex was attributed to

spin-orbit coupling between the emitting $^3\pi$-π^* state and ^{3,1}d-π^* charge-transfer state.[87] In fluid acetonitrile or ethanol/methanol solutions (297 K) an exceedingly weak emission was observed, however, it was considerable blue-shifted (0-0 energy ~ 440 nm) (Figure 39b). Attempts to measure the luminescence lifetime at this temperature in fluid acetonitrile showed the lifetime to be shorter than the pulse from the laser used for excitation (< 3.5 ns).

A different emission spectrum was found for the $[Rh(bpy)_2dpp]^{3+}$ complex in the 77 K methanol-ethanol glass (Figure 41 and 82). The predominant characteristic is an intense, broad band centered at 570 nm. The lifetime of the intense, broad emission, monitored at the 570 nm maximum, is 75 μs. At higher temperatures and more specifically at room temperature there is a significant change in the emission properties of the rhodium complex. Under these conditions, in either acetonitrile or ethanol-methanol (4:1 by volume) solutions the emission is dominated by a broad Gaussian band with a maximum intensity at 443 nm. The lifetime of this emission in fluid solutions was measured to be 17 ns, which was very close to the laser pulse lifetime used to excite the complex.

The emission data described above will be discussed in terms of two key features: firstly, the relative qualitative similarity of the emission spectra of the dichloro bis(bpy) rhodium complex along with the similar lifetime**,** and secondly, the marked differences in excited-state luminescence properties of the tris(bpy) rhodium complex. As previously stated, the broad Gaussian emission and relatively short excited-state lifetime of $[Rh(bpy)_2Cl_2]^+$ (28.3 μs at 77 K) led to the assignment of the lowest energy, emitting

excited state of this complex as a triplet MC state. [84] On the basis of the similar in energy Gaussian band shape at 570 nm and short lifetime of the $[Rh(bpy)_2dpp]^{3+}$ emission, the analogous excited-state assignment in this case would be appropriate. Although initial 319 nm excitation is into π-π* intraligand absorption bands, it has been well established that internal conversion/intersystem crossing to the lowest excited state is very rapid. [105] A similar argument can be for the higher energy band in the emission spectrum of the $[Rh(bpy)_2dpp]^{3+}$ at room temperature by comparing it with the $[Rh(bpy)_3]^{3+}$ complex; based on the location, this emission is ligand centered π-π* in nature. Thus, $[Rh(bpy)_2dpp]^{3+}$, exhibits two independent emissions, one at low temperature and one at high temperature where the two have different orbital parentages. By keeping the two bpy ligands as the common factor between the three rhodium complexes ($[Rh(bpy)_2dpp]^{3+}$, $[Rh(bpy)_2Cl_2]^{+}$, $[Rh(bpy)_3]^{3+}$), and changing the third ligand by either two chlorines or one bpy and one dpp the symmetry of the complex changes and this change in symmetry has a profound effect on the emission properties of each complex. The change in the coordination environment of the rhodium metal, results in the change of the Rh−N bond length and bond angles. Qualitatively, one might expect that the twisting of the bpy would reduce the π-acceptor ability of the rings as well as reduce the overlap between the pyridyl nitrogen σ orbitals and metal orbitals of the same symmetry. In the case of the $[Rh(bpy)_2Cl_2]^{+}$, this twisting is more pronounced thus making the MC states lower in energy. When the tris(bpy) rhodium complex is considered, the distortion noted above is less pronounced, lowering the LC state energies of the$[Rh(bpy)_3]^{3+}$ complex relative to the other two complexes.

Observation of only π-π* emission under the higher temperature conditions implies that the radiative rate constant from the π-π* state is likely to be much smaller than that from the MC excited state,[106] thus, that the LC excited state has the greater population and is therefore lower in energy. The noticeable intensity enhancement of the π-π* emission relative to the MC emission upon the phase change to the liquid acetonitrile medium at 297 K is consistent with equilibration of the two states, which, according to the present analysis, should result in a substantial increase in population of the lower energy π-π* state. A very surprising and puzzling finding was the extremely short lifetime of the $[Rh(bpy)_2dpp]^{3+}$ emission in fluid solution. The lifetime 17 ns, which was recorded in both acetonitrile and ethanol/methanol (4:1,v/v) solutions, was extremely short to be considered either a MC d-d or a LC π-π* phosphorescence. As previously state, for the analogous polypyridine Rh (III) complexes, the MC lifetimes are expected to be in the μs domain, whereas the LC lifetimes are expected to be in the ms domain. One plausible explanation would be that, in room temperature the two state are closer in energy and the LC π-π* triplet state undergoes fast thermal equilibrium with the MC d-d state. Thus, the two states would appear to behave as a single excite state.[60] This could suggest that at low temperature the two states fail to interconvert efficiently, due to a significant differences in the geometries of the two states and in the structures of the associated hydration spheres. Consequently, this can result in large, viscosity-dependent activation barriers for the nonradiative transitions between these states. Thus, once the MC and LC excited states are populated by competing internal-conversion/ intersystem crossing/vibrational relaxation pathways (Figure 9) from the upper states formed by

initial excitation, the rates of internal conversion between them are slower than the independent deactivation processes to the ground state. At higher temperatures and lower viscosities, solvent reorganizational barriers are reduced, and the thermal energy of the system becomes sufficient to overcome the remaining activation barriers. [107] Unlike the other complexes studied in this thesis, the emission properties of the $[Rh(bpy)_2dpp]^{3+}$ complex are strongly depended upon the solvent phase change from solid to liquid. This result suggests that the formation of the π-π^* requires a geometry change that is particularly strongly influenced by interactions with the solvent cage. Thus, some required twisting about the bridging bond between the pyridine rings, leads to large solvent induced barriers to formation of the π-π^* state.

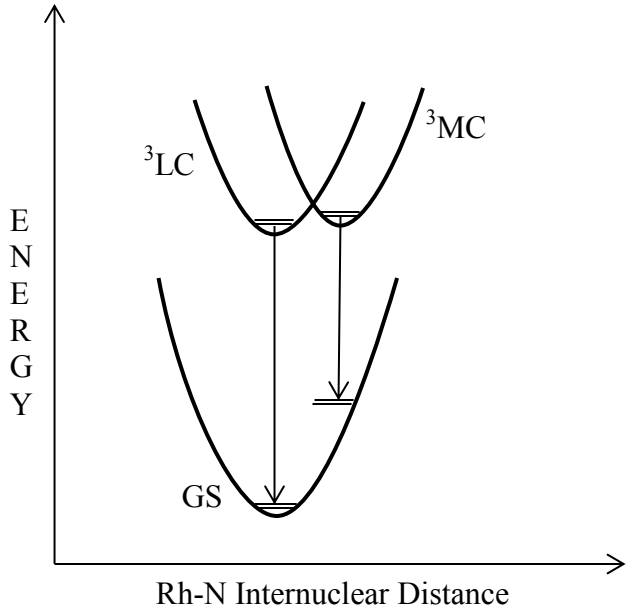

Figure 84. Potential energy curves for a Rhodium (III) polypyridine complex, relative energy ordering of LC and MC states depending on the complex. The photophysical behavior of Rh(III) polypyridine complexes are influenced by the two relevant low-energy excited states: the lowest triplet state centered on the polypyridine ligands and the lowest triplet state centered on the metal.

As previously state the photophysical properties of the rhodium (III) polypyridine complexes depend on the coordination environment of the metal. The higher symmetry (D_3) and less perturbed $[Rh(bpy)_3]^{3+}$ exhibits only a LC emission, $[Rh(bpy)_2Cl_2]^{+}$ with C_{2v} symmetry exhibits only MC emission and the lowest symmetry (C_2) $[Rh(bpy)_2dpp]^{3+}$ exhibits both MC and LC emissions. In the latter case, it is clear that the pyridine group in the position ortho to the C-C bond linking to the pyridine and pyrazine rings of the dpp ligand have served to alter the energies of both d-d and π-π* excited states. Relative to $[Rh(bpy)_3]^{3+}$, the energy of the metal-centered state is apparently the more greatly affected by the dpp ligand since MC emission is not seen in the $[Rh(bpy)_3]^{3+}$ complex but

is the major contributor for the $[Rh(bpy)_2dpp]^{3+}$ complex. This lowering of the MC state energies can be rationalized in terms of the ligand out-of-plane distortion causing decreased overlap between metal and ligand σ orbitals. The result is the decrease in the effective ligand field strengths of the distorted ligands. Figure 84, shows potential energy curves of the MC and LC states as a function of metal-ligand stretching. The MC excited states of d^6 octahedral complexes are strongly displaced with respect to the ground-state geometry along metal-ligand vibration coordinates.[119] When the lowest excited state is MC, it undergoes fast radiationless deactivation to the ground state and/or ligand dissociation reactions (Figure 85). As a consequence, at room temperature the excited-state lifetime is very short, no luminescence emission can be observed[120], and very rarely bimolecular reactions can take place. LC and MLCT excited states are usually not strongly displaced compared to the ground-state geometry. Thus, when the lowest excited state is LC or MLCT (Figure 85) it does not undergo fast radiationless decay to the ground state and luminescence can usually be observed, except at high temperature when thermally activated radiationless deactivation via upper lying MC excited states can occur.[118] The radiative deactivation rate constant is somewhat higher for ^{3}MLCT than for ^{3}LC because of the larger spin–orbit coupling effect. For this reason, the ^{3}LC excited states are longer lived at low temperature in a rigid matrix (e.g. $[Rh(bpy)_3]^{3+}$) and the ^{3}MLCT excited states are more likely to exhibit luminescence at room temperature in fluid solution (e.g. $[Ru(bpy)_3]^{2+}$).[118]

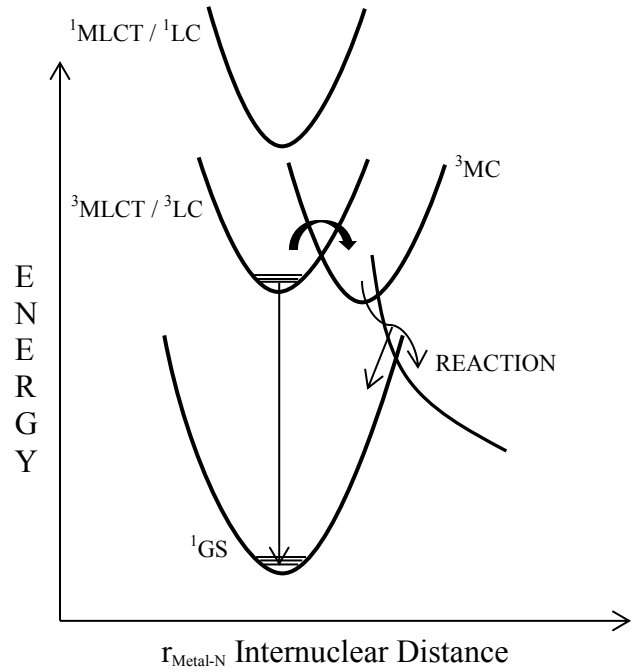

Figure 85. Potential well diagrams involving relative energies of the ^{3}MC ^{3}LCand ^{3}MLCT for Rh(III) and Ru(II) polypyridyl complexes.

4. B. 3. ABSORPTION AND EMISSION SPECTRA OF $[Ru(bpy)_{2(}dpp)]^{2+}$

In 1936, F. H. Burnstall published the first synthesis and characterization of $[Ru(bpy)_3]^{2+}$.[108] In 1965 Crosby *et al.*[109] characterized the luminescence of the $[Ru(bpy)_3]^{2+}$ complex; this complex exhibits a long-lived (~650 ns) metal to ligand charge transfer (MLCT) excited state. In 1972, Gafney and Adamson[110] found that it was capable of excited state energy and electron transfer; this paper, established $[Ru(bpy)_3]^{2+}$ as a relatively efficient excited state electron transfer agent, capable of transferring one electron to a substrate. Thus, $[Ru(bpy)_3]^{2+}$, gained a prominent role in photochemical schemes. Subsequent studies by other research groups,[111-114] showed that this complex

has a unique combination of chemical stability, redox properties, excited state reactivity, and excited state lifetime. Shortly thereafter it was recognized that, because of its photoredox properties, $[Ru(bpy)_3]^{2+}$ might function as a photocatalyst for the decomposition of water into hydrogen and oxygen.[116] Since then, the interest in the study of the photochemistry of Ru(II) polypyridine complexes has increased exponentially.[115] Ru(II) polypyridine complexes are good visible light absorbers, feature relatively intense and long-lived luminescence, and can undergo reversible redox processes in both the ground and excited states. A wide variety of $[Ru(bpy)_3]^{2+}$ analogs have been synthesized and characterized; in the Gafney group, $[Ru(bpy)_2dpp]^{2+}$ was extensively studied by Dr. Jose Zambrana, [117] and it was the first complex that I experiment with to get my feet wet.

The spectroscopic and electrochemical properties of transition metal complexes, as previously stated in the introduction, are typically described using molecular orbitals. For pseudo octahedral d^6 metal complexes, like Ru(II) polypyridine complexes, the molecular orbital picture is commonly described by the linear combination of atomic orbitals (LCAO) theory (Figure 86). Figure 86 depicts a molecular orbital diagram for an octahedral complex with both σ bonding and π back-bonding. The s, p, and d metal orbitals combine with the σ and π ligand orbitals to form molecular orbitals. The highest occupied molecular orbitals (HOMOs) for the Ru(II) complex are mainly localized on the metal and are metal-based (dπ) in character. The lowest unoccupied molecular orbitals (LUMOs) for the Ru(II) complex are mainly localized on the ligands and are ligand based (π*) in character. These frontier orbitals play a key role in photochemical and redox processes. The HOMO will be the orbital involved in oxidation, the LUMO in reduction.

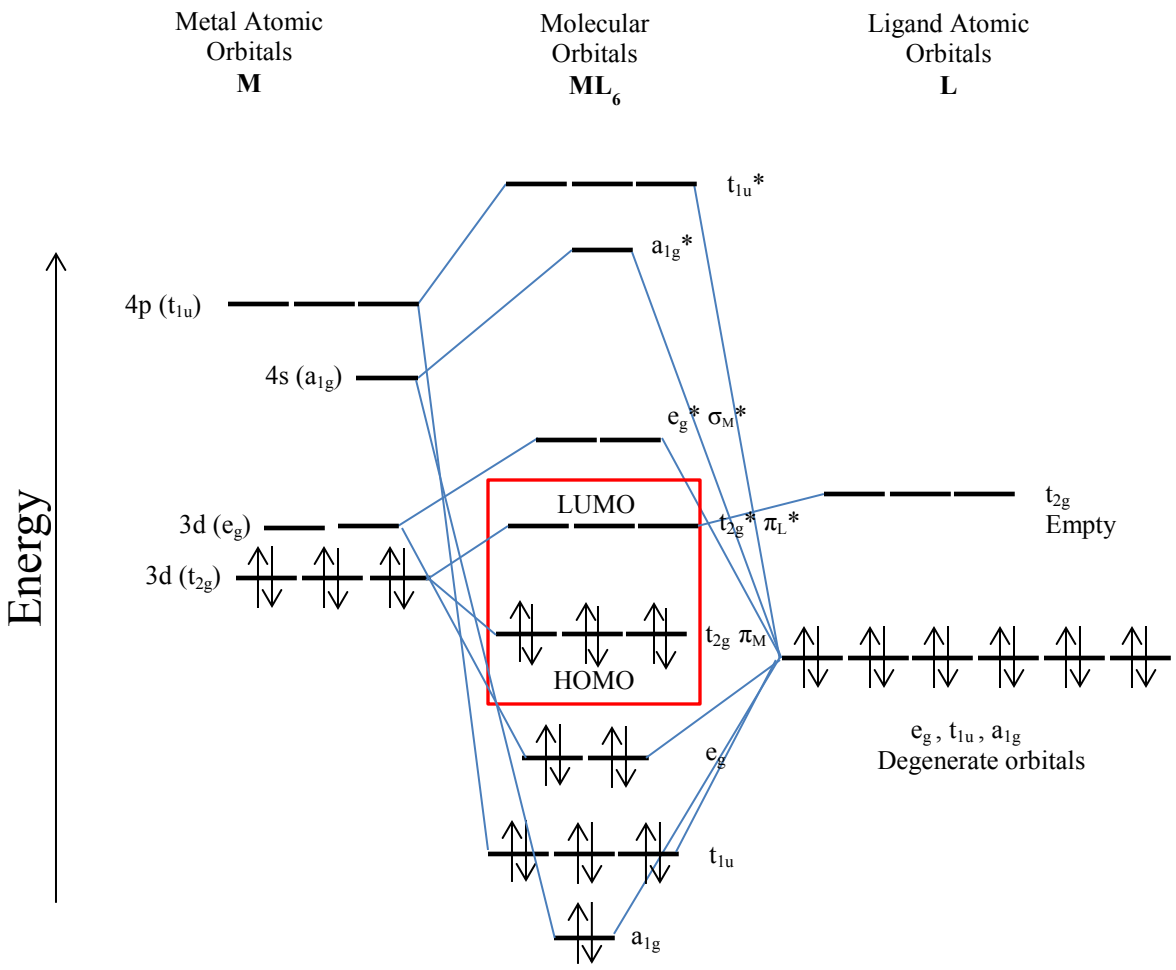

Figure 86. Molecular Orbital Representation of Octahedral Ru(II) Complexes.

Ru(II) is a d^6 system and the polypyridine ligands are molecules possessing σ-donor orbitals localized on the nitrogen atoms and π donor and π* acceptor orbitals more or less delocalized on aromatic rings. Following a single-configuration one-electron description of the excited state in octahedral symmetry (Figures 86 and 87), promotion of an electron from a π_M metal orbital to the π_L^* ligand orbitals gives rise to MLCT excited states, whereas promotion of an electron from π_M to σ_M^* orbitals gives rise to MC excited

states. LC excited states can be obtained by promoting an electron from π_L to π_L*. All these excited states may have singlet or triplet multiplicity, although spin-orbit coupling causes singlet-triplet mixing, particularly in the MC and MLCT excited states. For Ru(II) polypyridine complexes, the lowest excited state is a ^{3}MLCT level (or, as Figure 87 shows, a cluster of closely spaced ^{3}MLCT levels), which undergoes relatively slow radiationless transitions and thus exhibits relatively long lifetime and intense luminescence emission.[118]

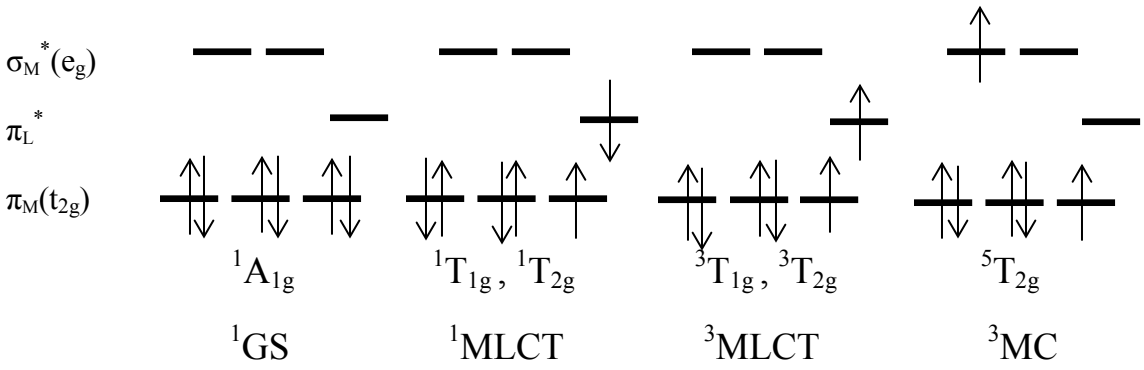

Figure 87. The *d* orbital diagram for the electronic ground and excited states for low spin d^6 Ru(II) complexes in O_h symmetry.

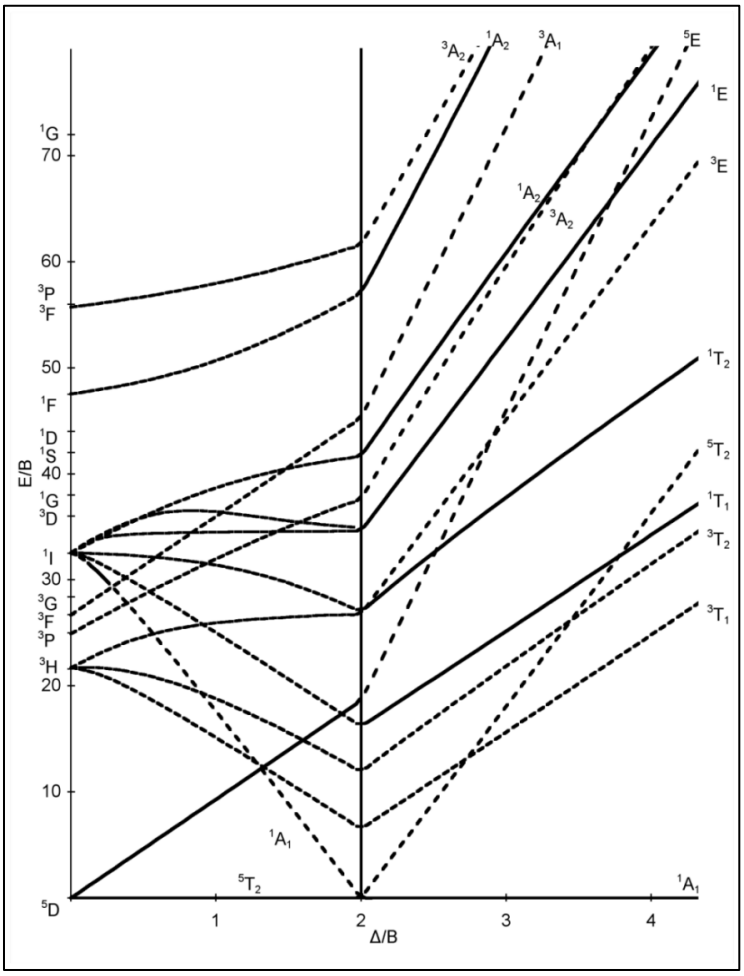

Figure 88. Tanabe-Sugano diagram for d^6 electron configuration.

The absorption spectrum of $[Ru(bpy)_2dpp]^{2+}$ is shown in Figure 72 along with the proposed assignments. The bands at 188 nm and 286 nm have been assigned to spin-allowed LC π-π^* transitions. The remaining intense bands at 248 and between 420-488 nm have been assigned to spin allowed MLCT d-π^* transitions. The shoulder at approximately 330 nm has been assigned to MC transitions. In the long-wavelength tail of the absorption spectrum a shoulder is present at about 530 nm. This absorption feature

is thought to be due to spin-forbidden MLCT transitions. As mentioned in the Introduction, the upper excited states of transition metal complexes usually undergo radiationless deactivation to the lowest excited state. For $[Ru(bpy)_2dpp]^{2+}$ the lowest lying excited state is typically Ru(d)→dpp(π^*) charge transfer. Excitation of $[Ru(bpy)_2dpp]^{2+}$ in any of its absorption bands leads to a luminescence emission observed in Figure 73. This ^{3}MLCT has an emission lifetime of 203 ± 8 ns.

4. C. 1. ELECTROCHEMICAL BEHAVIOR OF CHROMIUM (III) POLYPYRIDINE COMPLEXES.

Unlike the widely investigated $[Ru(diimine)_3]^{2+}$ complexes, charge transfer states do not dominate the chemistry of the Cr(III) analogs; instead, the lowest energy excited states are the metal centered ligand field doublet states. Thus, $[Cr(diimine)_3]^{3+}$ ions generally show long-lived metal centered phosphorescence at about 730 nm. The excited state reduction potential, $E^0(^*Cr^{3+}/Cr^{2+})$ can be estimated from the $^2E_g \rightarrow {}^4A_{2g}$ emission energy (E_{0-0}) and the ground state reduction potential $E^0(Cr^{3+}/Cr^{2+})$. Notably, the metal centered ligand field excited state, $[^*Cr(phen)_2dpp]^{3+}$ is a significantly stronger oxidant than the MLCT excited state $[^*Ru(bpy)_2dpp]^{2+}$ (Figures 89 and 92).

For all four chromium complexes investigated by cyclic voltammetry(Pt working electrode, 0.1 M KCl aqueous solution), a reversible $[Cr(diimine)_3]^{3+}/[Cr(diimine)_3]^{2+}$ couple was observed prior to the water reduction wave. Cyclic voltammograms are provided in Figures 48 and 49 for the $[Cr(phen)_2(dpp)]^{3+}$ and $[Cr(bpy)_2dpp]^{3+}$ complexes, respectively, and a complete listing of the Cr^{3+}/Cr^{2+} reduction potentials obtained are

presented in Table 3, along with similar $[Cr(diimine)_3]^{3+}/[Cr(diimine)_3]^{2+}$ systems for comparison reasons (Table 6).[16,48,49,50] For the homoleptic complexes $[Cr(phen)_3]^{3+}$ and $[Cr(bpy)_3]^{3+}$, the reduction potentials are slightly less negative than those reported by Brunschwig and Sutin[52] under somewhat different conditions (1 M LiCl solution). The literature value of -0.23 V and -0.25 V for the Cr^{3+}/Cr^{2+} reduction potential of $[Cr(bpy)_3]^{3+}$ and $[Cr(phen)_3]^{3+}$, respectively, are in agreement with my corresponding values of -0.24 and -0.26 V (Table 3) obtained by a CV investigation of the much more water soluble $CF_3SO_3^-$ salt. Of particular interest with regard to future $Cr(diimine)_3^{3+}$ studies is the oxidizing power of the ^2E_g excited state, $E°(*Cr^{3+}/Cr^{2+})$, for this series of $[Cr(diimine)_3]^{3+}$ complexes (second column, Table 6).

TABLE 6. Electrochemical data of polypyridine chromium (III) complexes ($[Cr(diimine)_3]^{3+}$) in aqueous solution. r.t.

Complex	$E°/V(Cr^{3+}/Cr^{2+})$	$E°/V(*Cr^{3+}/Cr^{2+})$
$Cr(phen)_2(DPPZ)^{3+}$	-0.17	1.53
$Cr(bpy)_3^{3+}$	-0.23	1.47
$Cr(phen)_2(bpy)^{3+}$	-0.25	1.45
$Cr(phen)_3^{3+}$	-0.25	1.45
$Cr(phen)(TMP)_2^{3+}$	-0.40	1.28
$Cr(TMP)_3^{3+}$	-0.49	1.19
$Cr(phen)_2(dpp)^{3+}$	-0.52	1.18
$Cr(bpy)_2(dpp)^{3+}$	-0.23	1.48

These values were estimated from the difference between their emission energies expressed in V and standard reduction potentials, $E°(Cr^{3+}/Cr^{2+})$. It is noteworthy that the complex $[Cr(bpy)_2(dpp)]^{3+}$ is estimated from Table 6 to have a 30 mV greater excited state oxidizing power, $E°(*Cr^{3+}/Cr^{2+})$, than the $[Cr(phen)_3dpp]^{3+}$ complex.

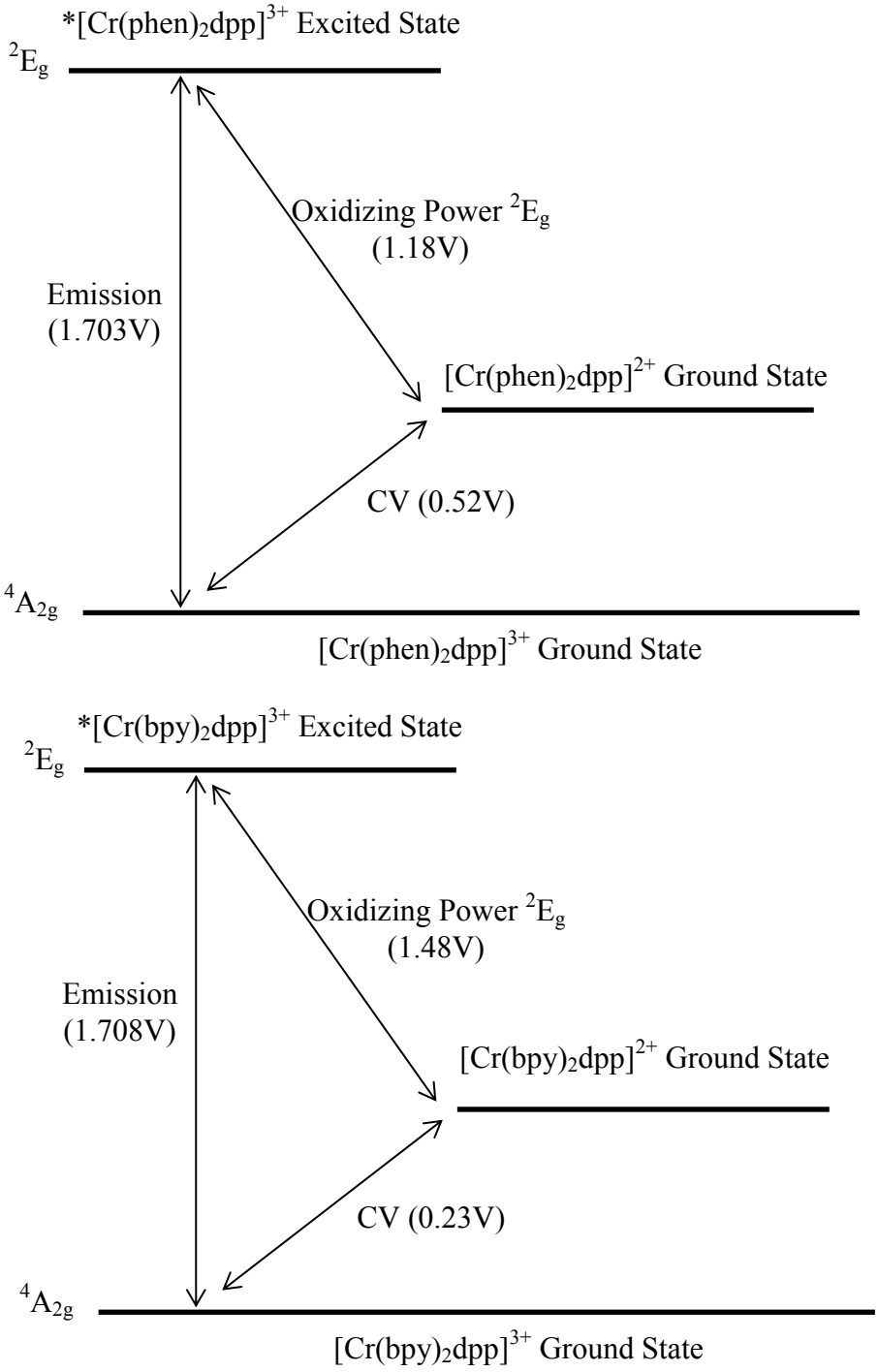

Figure 89. Energies and potentials related to the excited and ground state redox properties of the $[Cr(phen)_2dpp]^{3+}$ and $[Cr(bpy)_2dpp]^{3+}$ complexes.

4. C. 2. ELECTROCHEMICAL BEHAVIOR OF RHODIUM (III) POLYPYRIDINE COMPLEXES.

The d^6 Rh(III) polypyridine complexes have been much less thoroughly investigated than their isoelectronic Ru(II) polypyridine counterparts. As previously stated, the lowest lying excited state of $[Rh(bpy)_3]^{3+}$ differs from that of $[Ru(bpy)_3]^{2+}$. The lowest lying excited state in Ru(II) polypyridine complexes is Ru(d) → bpy(π^*) CT based, whereas the lowest lying excited state of $[Rh(bpy)_3]^{3+}$ has been reported to be largely ligand based ($\pi \rightarrow \pi^*$). The MLCT nature of the $[Ru(bpy)_3]^{2+}$ lowest lying excited state results in different properties than the $\pi \rightarrow \pi^*$ nature of the $[Rh(bpy)_3]^{3+}$ lowest lying excited state. Although $[Rh(bpy)_3]^{3+}$ and $[Ru(bpy)_3]^{2+}$ are isoelectronic and isostructural, $[Rh(bpy)_3]^{3+}$ is not a desirable excited state electron transfer agent. In principle, $[Rh(bpy)_3]^{3+}$ has outstanding oxidizing properties in their lowest excited state, with E^o values of approximately +1.96V, (Figure 90 the reduction potential of the $[Rh(bpy)_3]^{3+}/Rh(bpy)_3]^{2+}$ couple is -0.79V and the excited-state spectroscopic energy of the $\pi \rightarrow \pi^*$ state 2.75V). In theory, this means that $*[Rh(bpy)_3]^{3+}$ is expected to be a much stronger oxidant than all the excited Ru(II) and Cr(III) complexes. In spite of this, the practical use of these photosensitizers in excited-state electron transfer studies has been extremely limited. This is no doubt due to the fact that Rh(III) polypyridine complexes are essentially non-luminescent in room-temperature fluid solutions, a feature which has made the monitoring of excited-state bimolecular processes with these systems a very difficult task. Thus, there are distinct differences in the electrochemistry of the $[Rh(bpy)_3]^{3+}$ and $[Ru(bpy)_3]^{2+}$ complexes. The first reduction displayed in the CV of $[Rh(bpy)_3]^{3+}$ is rhodium based followed by ligand based reductions, there are no

oxidations present in the electrochemistry of the rhodium in this complex (Figure 51). The $[Rh(bpy)_2dpp]^{3+}$ complex displays a similar cyclic voltammogram (Figure 50).

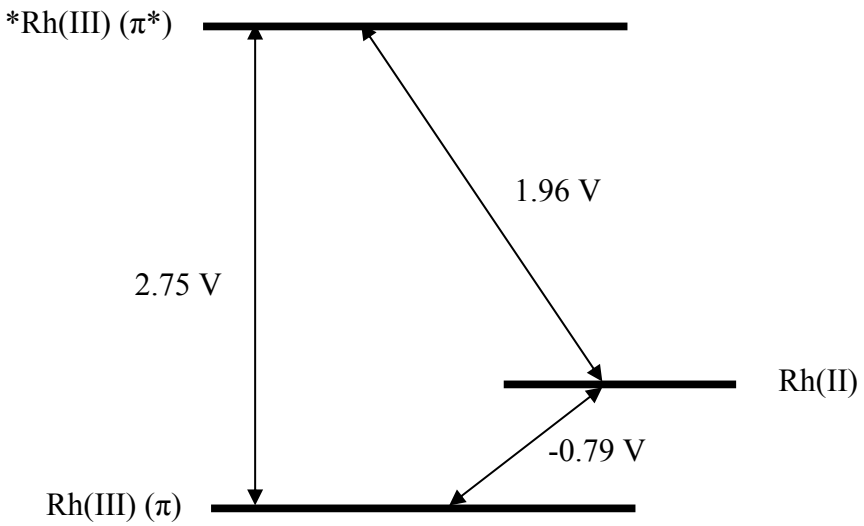

Figure 90. Redox energy level diagram for $[Rh(bpy)_3]^{3+}$ complex.

DeArmond *et al.*[78,79] examined the electrochemical properties of several Rh(III) polypyridine complexes. A cyclic voltammetry study of $[Rh(bpy)_3]^{3+}$ showed the first reduction to be at rhodium, followed by subsequent reductions of the bpy ligands. The two-electron reduction of $[Rh(bpy)_3]^{3+}$ results in the loss of a bpy ligand and in the conversion of the rhodium from d^6 to d^8. In the initial complex $[Rh(bpy)_3]^{3+}$, the d^6 rhodium is pseudo-octahedral. Upon conversion from the Rh(III) d^6 electron configuration to Rh(I) d^8, the stable rhodium geometry becomes square planar. Therefore, the two-electron reduction product of $[Rh(bpy)_3]^{3+}$ is the square planar Rh(I) complex, $[Rh(bpy)_2]^-$.[78,79] As seen in Figure 91, after the Rh(III) center is reduced by one electron,

a rapid chemical step occurs. The subsequent rhodium reduction [Rh(II/I)] is also followed by a rapid loss of one bpy ligand, which results in $[Rh(bpy)_2]^-$. These steps encompass the ECEC portion of the electrochemical mechanism, which was proposed by DeArmond *et al.*,[79] and could successfully explain the electrochemical mechanism of the related $[Rh(bpy)_2dpp]^{3+}$ complex.

$[Rh(bpy)_3]^{3+}$

↓↑ $1e^-$ E

$[Rh(bpy)_3]^{2+}$

+Y ↓ (Very Fast) C

$[Rh(bpy)_2Y]^{2+}$ + bpy

↓↑ $1e^-$ E

$[Rh(bpy)_2Y]^+$

↓ (Very Fast) C

$[Rh(bpy)_2]^+$ + Y

↓↑ $1e^-$

$[Rh(bpy)_2]^0$

↓↑ $1e^-$

$[Rh(bpy)_2]^-$

Figure 91. Proposed ECEC Mechanism for the two-electron Reduction of $[Rh(bpy)_3]^{3+}$ by cyclic voltammetry, where ECEC = electrochemical-chemical-electrochemical-chemical, Y = acetonitrile.
Proposed reaction sequence adapted from reference 79.

4. C. 3. ELECTROCHEMICAL BEHAVIOR OF RUTHENIUM (II) POLYPYRIDINE COMPLEXES.

As previously mentioned, the complexes of the Ru(II) polypyridine family are particularly interesting as excited state reactants or products in electron transfer processes. A fundamental requirement for playing these roles is the stability of the oxidized and/or reduced forms, i.e. the reversibility of the oxidation and/or reduction processes in the ground state. A plethora of information is available on the electrochemical behavior of Ru(II) polypyridine complexes, and the most widely used electrochemical method has been CV in non-aqueous aprotic solvents. Oxidation of Ru(II) polypyridine complexes usually involves a metal centered [π_M (t_{2g})] orbital, with formation of Ru(III) complexes (low spin $4d^5$ configuration) which are inert to ligand substitution.[121] Electrochemical experiments on the $[Ru(bpy)_2dpp]^{2+}$ complex were not conducted during my research. According to Braustein *et al.*[103] the $[Ru(bpy)_2dpp]^{2+}$ complex exhibits a metal centered one electron reversible oxidation with a mean half-wave potential of 1.34 V[104] (in acetonitrile, working electrode Pt, SCE).

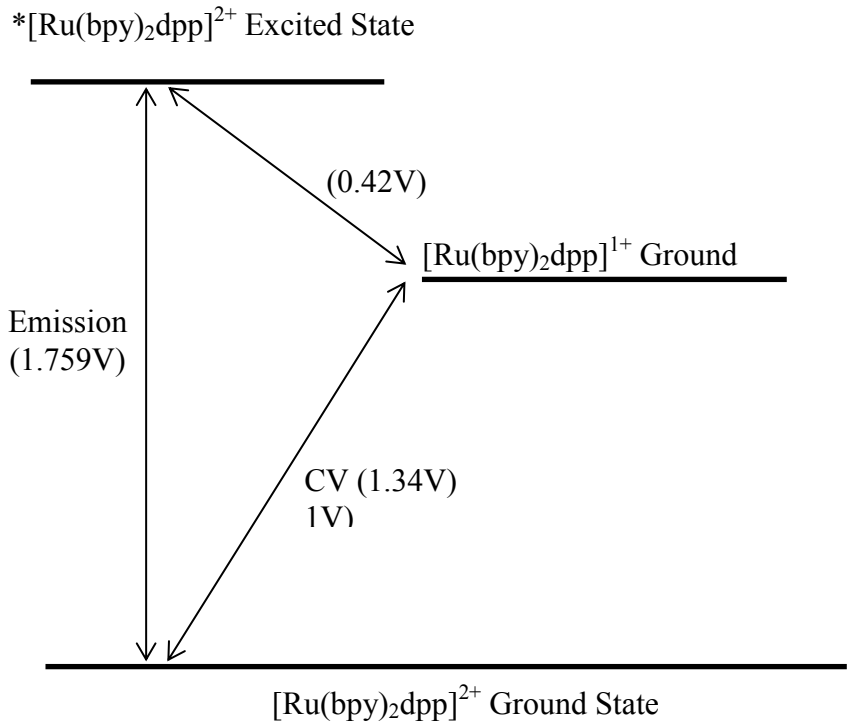

Figure 92. Energies and potentials related to the excited and ground state redox properties of the $[Ru(bpy)_2dpp]^{2+}$ complex.

4. D. TITRATIONS

The ground and excited states of both chromium (III) complexes, $[Cr(phen)_2(dpp)]^{3+}$ and $[Cr(bpy)_2(dpp)]^{3+}$, were probed using buffer solutions. The emission properties of $[Cr(phen)_2(dpp)]^{3+}$ were further investigated using sodium hydroxide. The complexes $[Cr(phen)_2(dpp)]^{3+}$ and $[Cr(bpy)_2(dpp)]^{3+}$ emit strongly in room temperature aqueous solution, with long emission lifetimes of 87 μs and 327 μs in N_2 saturated solution, respectively.

In solutions of high pH, strong quenching of the 727 nm steady-state $^2E_g \rightarrow {}^4A_{2g}$ phosphorescence signal of both chromium complexes is observed (Figures 52 and 60), as well as quenching of the corresponding emission lifetime. This result is exactly the opposite of that observed for the $[Ru(bpy)_2(dpp)]^{2+}$ complex[117], where quenching of Ru(II) luminescence signals occur in strong acidic media. Moreover, in the case of the $[Rh(bpy)_2(dpp)]^{3+}$ complex, a moderate intensification of the Rh(III) luminescence signal occurs in high pH, whereas in low pH the luminescence signal appears to be unaffected (Figure 67).

The single inflection point in the titration plot of the emission spectra vs. pH (Figures 53 and 61) is indicative of one protonation step with a characteristic pKa^* at the inflection point. The inflection points indicate an excited state pKa^* of 8.5 and 9.5, for the $[Cr(phen)_2(dpp)]^{3+}$ and $[Cr(bpy)_2(dpp)]^{3+}$ complexes, respectively. The absorption spectrum of the $[Cr(phen)_2(dpp)]^{3+}$ was monitored at 280 nm and 307 nm, which correspond to the dpp and bpy ligands, respectively. The absorption band at 280 nm shows an increase in intensity, whereas the one at 307 nm shows a decrease. Titration curves are presented in Figures 58 and 59. A single inflection point is present at approximately 5±0.3. The moderate inflection change, as opposed to a sharp, steep change, may be indicative of a weak acid-weak base titration in buffer solutions or may reflect the kinetics of protonation. The inflection point shows a ground state pK_a of 5±0.3 (Figures 58 and 59). Comparison of the excited and ground state pK_a values of the $[Cr(phen)_2(dpp)]^{3+}$ complex shows that the excited state is a much stronger base than the ground state.

As previously stated the emission properties of the for $[Cr(phen)_{2(}dpp)]^{3+}$ were further investigated using aqueous solutions of sodium hydroxide. A gradual decrease in the phosphorescence signal occurs with increasing hydroxide concentration. The $[OH^-]$ Stern-Volmer lifetime quenching plot for $[Cr(phen)_{2(}dpp)]^{3+}$ at r.t. in N_2 saturated shows a good straight line fit (Figures 65) in accordance with collisional quenching of unbound $[Cr(phen)_2(dpp)]^{3+}$ by the hydroxide ion. Dividing the slope by the complex lifetime in the absence of hydroxide ion yields a bimolecular quenching rate constant of $3\times10^{7}\ M^{-1}\ s^{-1}$. However, the analogous Stern-Volmer steady-state emission-quenching plot (Figure 65) exhibits marked upward curvature with increasing OH^- concentration. The curvature is attributed to static quenching associated with (OH^-)-bound $[Cr(phen)_2(dpp)]^{3+}$, which is non-luminescent. Consistent with this rationalization, the initial $[Cr(phen)_2(dpp)]^{3+}$ phosphorescence intensity in timed-resolved emission studies decreases significantly as the hydroxide ion concentration is increased. From the difference between the emission energy and standard reduction potential in aqueous solution, I have previously estimated that $[Cr(phen)_2(dpp)]^{3+}$ has an excited state oxidizing power of 1.18 V. The emission quenching of this complex by hydroxide ions can be rationalized by the significantly high oxidizing power of the ^2E_g excited state.

Examination of the emission spectrum of $[Rh(bpy)_2(dpp)]^{3+}$ shows that there is a noticeable enhancement of the 440 nm emission at high pH. The single inflection point in the titration plot of the emission spectra vs. pH (Figure 68) yields a pKa^* of 9.5 for $[Rh(bpy)_2(dpp)]^{3+}$ complex. The absorption spectrum of the $[Rh(bpy)_2(dpp)]^{3+}$ was also

monitored at 280 nm and 307 nm. The absorption band at 280 nm shows an increase in absorption intensity, whereas the one at 307 nm shows a decrease. This result is the inverse of that observed for the $[Cr(phen)_2(dpp)]^{3+}$ complex. Titration curves are presented in Figures 58 and 59, both show an inflection point at approximately 8.5. It is noteworthy that the difference in pK_a values between ground state and excited is much smaller for the rhodium complex compared to that of the chromium complex. Furthermore, due to the extremely short lifetime of $[Rh(bpy)_2(dpp)]^{3+}$ complex in room temperature, meaningful lifetime measurements could not be conducted.

CHAPTER 5

5. CONCLUSION

5. A. GENERAL DISCUSSION

Transition metal complexes with organic ligands have found an increasing interest, since these complexes exhibit an enormous potential for the discovery of new physical and chemical properties and applications. Most of the possible applications are related to properties of the lowest excited electronic states which, therefore, are intensively investigated. In addition, there is substantial scientific interest to come to a better understanding of these metal complexes with organic ligands, especially since they exhibit new electronic and vibronic properties, which are found neither in pure and well-studied organic molecules[122] nor in simple transition metal complexes with d-d* transitions.[123] For example, complexes with electronic states of metal-to-ligand- charge-transfer (MLCT) character, like $[Ru(bpy)_3]^{2+}$,[118] complexes with a very small amount of metal-d contributions in the lowest excited states, like $[Rh(bpy)_3]^{3+}$ [58,65,87,93,124] and complexes with electronic states of metal center character (MC), like $[Cr(bpy)_3]^{3+}$. For these it is still a challenge to derive a comprehensive description of their excited states' properties. Different combinations of coordination metals and aromatic ligands give rise to different characters of the lowest excited states depending on the ligand-field parameters and magnitudes of oxidation potentials of the metal ions. The lowest excited π-π*, d-π*, and d-d* states have been found for different complexes of the diimine ligands: bpy, dpp, and phen. The energies of transition-metal-complex excited states can

be modified with the usage of ligand substituents. The use of ligand substituents to alter absorption and emission properties in this manner has been termed “tuning”, and such molecular engineering has proved especially successful in modifying the photochemical properties of various pyridyl, polypyridyl, and similar nitrogen aromatic heterocyclic transition-metal complexes. In most of these cases the substituent role is largely confined to electronic effects on the σ- and π-donor and -acceptor properties of the heterocyclic ligands.

Chromium (III) tris-diimine and Rhodium (III) tris-diimine complexes were synthesized, characterized and studied by electrochemistry, electronic absorption spectroscopy, luminescence spectroscopy, and time resolved luminescence spectroscopy.

By attaching the dpp ligand to the metal, the complex itself then can be considered to be a weak base due to the non-ligating nitrogens. This has some interesting and distinctive results, differentiating each metal from the other. In the case of the $[Ru(bpy)_2dpp]^{2+}$ complex protonation of those sites results in quenching of the MLCT emission. In the case of both the $[Cr(bpy)_2dpp]^{3+}$ and $[Cr(phen)_2dpp]^{3+}$ protonation results in enhancement of the both phosphorescence and fluorescence emissions, meaning that somehow the radiative rates has increase with respect to the nonradiative rates, whereas, in the $[Ru(bpy)_2dpp]^{2+}$ complex, protonation doesn’t seem to effect it’s the room temperature emission. Furthermore, in both Chromium (III) complexes, $[Cr(bpy)_2dpp]^{3+}$ and $[Cr(phen)_2dpp]^{3+}$, the emissions are quenched in basic solutions, whereas, the emission of $[Rh(bpy)_2dpp]^{3+}$ is enhanced. The luminescence properties of the rhodium complexes are greatly affected by the symmetry environment of the

complex. The usage of different ligands causes significant disturbances to the bond angles and bond distances. Consequently, one could expect the energies of excited states involving π-symmetry ligand orbitals to be affected due to decreased delocalization between the rings.[2] Furthermore, the twisting of the bpy and dpp ligands would reduce the π-acceptor ability of the rings as well as reduce the overlap between the pyridyl nitrogen σ orbitals and metal orbitals of the same symmetry. In the case of the $[Rh(bpy)_2dpp]^{3+}$ complex the dpp ligand plays a crucial role in its emission properties. Tables 7 and 8 summarize the absorption and emission for rhodium, chromium and ruthenium complexes. In contrast to the rhodium, the emission properties of the analogous chromium and ruthenium complexes are not significantly affected by the coordination environment; their emission assignments remain the same with a noticeable change in lifetimes.

TABLE 7. Electronic absorption data for a series of chromium, rhodium and ruthenium polypyridyl complexes.

Complex	Wavelength (nm)	Assignment
$[Ru(bpy)_2(dpp)]^{2+}$	286	bpy π → π*
	426	Ru(d) → bpy(π*) MLCT
	484	Ru(d) → dpp(π*) MLCT
$[Cr(phen)_2(dpp)]^{3+}$	283	dpp π → π*
	314	bpy π → π*
	400-460	Cr d→ d
$[Rh(bpy)_2(dpp)]^{3+}$	286	dpp π → π*
	307	bpy π → π*
	320	bpy π → π*

TABLE 8. Emission spectral data and lifetimes for a series of chromium, rhodium and ruthenium complexes.

Complex	Emission Max (nm)	τ_o	Assignment	
$[Ru(bpy)_2(dpp)]^{2+}$	683	203 ns	$d \rightarrow \pi^*$	MLCT (r.t.)
$[Ru(bpy)_3]^{2+}$	430	650 ns	$d \rightarrow \pi^*$	MLCT (r.t.)
$[Cr(phen)_2(dpp)]^{3+}$	728	87μs	$d \rightarrow d$	MC (r.t.)
$[Cr(bpy)_2(dpp)]^{3+}$	726	327μs	$d \rightarrow d$	MC (r.t.)
$[Cr(bpy)_3]^{3+}$	730	67 μs	$d \rightarrow d$	MC (r.t.)
$[Cr(phen)_3]^{3+}$	730	351 μs	$d \rightarrow d$	MC (r.t.)
$[Rh(bpy)_2(dpp)]^{3+}$	570	75μs	$d \rightarrow d$	MC (77 K)
	443	17 ns	$\pi \rightarrow \pi^*$	LC (r.t.)
$[Rh(bpy)_3]^{3+}$	479	62 ms	$\pi \rightarrow \pi^*$	LC (77 K)
$[Rh(bpy)_2Cl_2]^{+}$	675	28μs	$d \rightarrow d$	MC (77 K)

5. B. FUTURE DIRECTIONS

Chromium (III) tris-diimine complexes like those presented herein show efficient photochemistry with DNA, making them interesting biologically relevant photochemicals. The interaction of $M(diimine)_3^{n+}$ complexes with DNA has matured into a vital sub-discipline of bioinorganic chemistry. To date, literature reports have been restricted almost exclusively to low-spin d^6 complexes, such as Ru^{2+}; and d^3 complexes, like $Cr(diimine)_3^{3+}$, provides an attractive alternative to these species because of their strong room temperature luminescence ($^2E_g \rightarrow {}^4A_{2g}$ phosphorescence), and the well-documented oxidizing power of the ^{2}Eg excited state.

BIBLIOGRAPHY

(1) Gilbert, A. and Baggott, J. E., *Essentials of molecular photochemistry*, Blackwell Scientific: London, 1991.
(2) Turro, N. J., *Modern molecular photochemistry*, University Science Books: Sausalito, 1991.
(3) Turro, N. J., Ramamurthy, V. and Scaiano, J.C., *Principles of molecular photochemistry: An introduction*, University Science Books: Sausalito, 2009.
(4) Wayne, C.E. and Wayne, R.P., *Photochemistry*, Oxford University Press: Oxford, 1996.
(5) Balzani, V. and Campagna, S., *Topics in current chemistry: Photochemistry and photophysics of coordination compounds I*, Springer: Berlin, 2007.
(6) Steinfeld, J. I., *Molecules and radiation: An introduction to modern molecular spectroscopy,* The MIT Press: Cambridge, 1974.
(7) Demas, J. N., *Excited state lifetime measurements,* American Press, INC: New York, 1983.
(8) Parker, C.A., *Photoluminescence of solutions*, Elsevier Publishing Company: Amsterdam, 1968.
(9) Basolo, F.; Pearson, R.G., *Mechanisms of Inorganic Reactions*, 2nd Edition; Wiley: New York, 1967.
(10) Shriver, D. F.; Atkins, P.; Langford, C. H. *Inorganic Chemistry,* 2nd Edition; W.H. Freeman and Company: New York, 1994.
(11) Lakowicz, J.R., *Principles of Fluorescence Spectroscopy*, 3rd Edition; Springer: New York, 2006.
(12) Kalyanasundaram, K., *Photochemistry of polypyridine and porphyrin complexes,* Academic Press: London, 1992.
(13) Favaro, G. *J. Photochem.* **1986**, 35, 375.
(14) Burstall, F.H.; Nyhlom, R.S. *J. Chem. Soc.* **1952**, 3570.
(15) Ryu, C.K.; Endicott, J.F. *Inorg. Chem.* **1988**, 27, 2203.
(16) Barker, K.D.; Barnett, K.A.; Connell, S.M.; Glaeser, J.W.; Wallace, A.J.; Wildsmith, J.; Herbert, B.J.; Wheeler, J.F.; Kane-Maguire, N.A.P. *Inorg. Chim. Acta.* **2001,** 316, 41.
(17) Ronco, S.; Persing, B.; Mortinsen, R.; Barber, J.; Shotwell, S. *Inorg. Chim. Acta.* **2000,** 308, 107.
(18) Kang, Y. S.; Castelli, F.; Forster, L. S. *J. Phys. Chem.* **1979**,83,2366.
(19) Kirk, A. D.; Porter, G. B. *J. Phys. Chem.* **1980**, 84, 887.
(20) Kirk, A. D.; Porter, G. B. *J. Phys. Chem*. **1980**, 84, 2998.
(21) Gutierrez, A.R.; Adamson, A.W. *J. Phys. Chem*.**1978**, 82, 902.
(22) Kane-Maguire, N.A.P.; Crippen, W.S.; Miller, P.K. *Inorg. Chem.* **1983**, 22, 696.
(23) Zinato, E.; Adamson, A.W. *J. Phys. Chem.* **1985**, 89, 839.
(24) Chen, P.; Meyer, T.J. *Chem. Rev.* **1998**, *98,* 1439.
(25) Watson, R.T.; Desai, N.; Wildsmith, J.; Wheeler, J.F.; Kane-Maguire, N.A.P. *Inorg. Chem.* **1999**, *38,* 2683.
(26) Kane-Maguire, N.A.P.; Wheeler, J.F. *Coord. Chem. Rev.* **2000**, 211, 145.

(27) Wagenknecht, P.S.; Ford, P.C. *Coord. Chem. Rev.* **2011**, 255, 591.
(28) Serpone, N; Jamieson, M.A.; Henry, M.S.; Hoffman, M.Z.; Bolletta, F.; Maestri, M.J. *J. Am. Chem. Soc*. **1979**,101, 2907.
(29) Herbert, B.J; Carpenter, H.E; Kane-Maguire, N.A.P.; Wheeler, J.F. *Anal. Chim. Acta.* **2004,** 514, 27.
(30) Smith, J.A.; George, M.W.; Kelly, J.M. *Coord. Chem. Rev.* **2011**, 255, 2666.
(31) Forster, L.S. *Coord. Chem. Rev.* **2002**, 227, 59.
(32) Kharmawphlang, W.; Choudhury, S.; Deb, A.K.; Goswami, S. *Inorg. Chem.***1995**, 34, 3826.
(33) Haq, I.; Lincoln, P.; Suh, B.; Norden, B.; Chowdhry, B.Z.; Chaires, J.B. *J. Am. Chem. Soc*. **1995**,117, 4788.
(34) Mytykh, O.V.; Martin, S.E; Wheeler, J.F.; Kane-Maguire, N.A.P. *Inorg. Chim. Acta.* **2000,** 311, 143.
(35) Tiyabhorn, A.; Zahir, O.K. *Can. J. Chem.* **1996**, 74, 336.
(36) Kalyanasundaram, K. *Coord. Chem. Rev.* **1982**, 46, 161.
(37) Kalyanasundaram, K.; Grätzel, M. *Coord. Chem. Rev.* **1998**, 77, 347.
(38) Kirk, A.D.; Namasivayam, C.; Riske, W.; Ristic-Petrovic, D. *Inorg. Chem.* **1989**, 28, 972.
(39) Ferraudi, G.; Argiiello, G.A.; Frink, M.E. *J. Phys. Chem.* **1987**, 91, 64.
(40) Bolletta, F.; Maestri, M.; Moggi, L.; Jamieson, M.A.; Serpone, N.; Henry, M.S.; Hoffman, M.Z. *Inorg. Chem.* **1983**, 22, 2502.
(41) Dixon, N.E.; Jackson, G.W.; Lamcaster, M.J.; Lawrence, G.A.; Sargeson, A.M. *Inorg. Chem.* **1981**, 20, 470.
(42) Hauser, A.; Mäder, M.; Robinson, W. T.; Murugesan, R.; Ferguson, J. *Inorg. Chem.* **1987**, 26, 1331.
(43) Kane-Maguire, N.A.P.; Wallace, K.C.; Miller, D.B. *Inorg. Chem.* **1985**, 24, 597.
(44) Kane-Maguire, N.A.P.; Allen, M.M.; Vaught, J.M.; Hallock, J.S.; Heatherington, A.L. *Inorg. Chem.* **1983**, 22, 3851.
(45) Kane-Maguire, N.A.P.; Wallace, K.C.; Cobranchi, D.P.; Derrick, J.M.; Speece, D.G. *Inorg. Chem.* **1986**, 25, 2101.
(46) Vaidyanathan, V.G.; Nair, B.U. *J. Inorg. Bio.* **2003**, 95, 334.
(47) Cornioley-Deuschel, C.; Zelewsky, A.V. *Inorg. Chem.* **1987**, 26, 962.
(48) Vandiver, M. S.; Bridges, E. P; Koon, R. L.; Kinnaird, A. N.; Glaeser, J. W.; Campbell, J. F.; Priedemann, C. J.; Rosenblatt, W. T.; Herbert, B. J.; Wheeler, S. K.; Wheeler, J. F.; Kane-Maguire, N. A. P. *Inorg. Chem.* **2010**, 49, 839.
(49) McDaniel, A. M; Tseng, H. W.; Damrauer, N. H.; Shores, M. P. *Inorg. Chem.* **2010**, 49, 7981.
(50) Donnay, E. G.; Schaeper, J. P.; Brooksbank, R. D.; Fox, J. L.; Potts, R. G.; Davidson, R. M.; Wheeler, J. F.; Kane-Maguire, N. A. P. *Inorg. Chim. Acta.* **2007,** 360, 3272.
(51) Vagnini, M. T.; Kane-Maguire, N. A. P.; Wagenknecht, P. S. *Inorg. Chem.* **2006**, 45, 3789.
(52) Brunschwig, B.; Sutin, N. *J. Am. Chem. Soc.* **1978**, 100, 7568.

(53) Serpone, N.; Jamieson, M. A.; Emmi, S. S.; Fuochi, P. G.; Mulazzani, Q. G.; Hoffman, M. Z. *J. Am. Chem. Soc.* **1981**, 103, 1091.
(54) Burrows, C. J.; Muller, J. G. *Chem. Rev.* **1998**, 98, 1109.
(55) Williams, A. T. R.; Wenfield, S. A.; Miller, J. N. *Analyst*, **1983**, 108, 1067.
(56) Kane-Maguire, N. A. P.; Langford, C. H. *J. Am. Chem. Soc.*, **1972**, 94, 2125.
(57) Sriram, R.; Henry, M. S.; Hoffman, M. Z. *Inorg. Chem.*, **1979**, 18, 1727.
(58) Crosby, G.A.; Elfrlng, W.H., Jr. *J. Phys. Chem.* **1976**, 80, 2206.
(59) Kalyanasundaram, K.; Grätzel, M.; Nazeeruddin, Md. K. *J. Phys. Chem.* **1992**, 96, 5865.
(60) Indelli, M.T.; Carioli, A.; Scandola, F. *J. Phys. Chem.* **1984**, 88, 2685.
(61) Mulazzani, Q.G.; Venturi, M.; Hoffman, M.Z. *J. Phys. Chem.* **1982**, 86, 242.
(62) Indelli, M.T.; Scandola, F. *Inorg. Chem.* **1990**, 29, 3056.
(63) Maestri, M.; Sandrini, D.; Balzani, V.; Maeder, U.; Zelewsky, A.V. *Inorg. Chem.* **1987**, 26, 1323.
(64) Frei, G.; Zilian, A.; Raselli, A.; Güdel, H.U.; Bürgi, H. *Inorg. Chem.* **1992**, 31, 4766.
(65) Nishizawa, M.; Suzuki, T.M.; Sprouse, S.; Watts, R.J.; Ford, P.C. *Inorg. Chem.* **1984**, 23, 1837.
(66) Amarante, D.; Cherian, C.; Catapano, A.; Adams, R.; Wang, M.H.; Megehee, E.G. *Inorg. Chem.* **2005**, 44, 8804.
(67) Amarante, D.; Cherian, C.; Emmel, C.; Chen, H.; Dayal, S.; Koshy, M.; Megehee, E.G.; *Inorg. Chim. Acta.* **2005**, 358, 2231.
(68) Burke, H.M.; Gallagher, J.F.; Indelli, M.T.; Vos, J.G. *Inorg. Chim. Acta.* **2004**, 357, 2989.
(69) Mürner, H.; Jackson, B.A.; Barton, J.K. *Inorg. Chem.* **1998**, 37, 3007.
(70) Gidney, P.M.; Gillard, R.D.; Heaton, B.T. *J. Chem. Soc., Dalton Trans.* **1972**, 2621.
(71) Miller, D.B.; Miller, P.K.; Kane-Maguire, N.A.P. *Inorg. Chem*. **1983**, 22, 3831.
(72) Miki, H.; Shimada, M.; Azumi, T.; Brozik, J.A., Crosby, G.A. *J. Phys. Chem.*, **1993**, 97, 11175.
(73) Hannon, M.J. *Coord. Chem. Rev.* **1996**, 152, 393.
(74) Brozik, J.A.; Crosby, G.A. *J. Phys. Chem. A* **1998**, *102,* 45.
(75) Brozik, J.A.; Crosby, G.A. *Chem. Phys. Lett.* **1996**, *255,* 445.
(76) Brozik, J.A.; Crosby, G.A. *Coord. Chem. Rev*. **2005**, 249, 1310.
(77) Ortmans, I.; Didier, P.; Kirsch-De Mesmaeker, A. *Inorg. Chem.*, **1995**, 34, 3695.
(78) Kew, G.; Hanck, K.; DeArmond, K. *J. Phys. Chem.* **1975**, *79*, 1828.
(79) Kew, G.; DeArmond, K.; Hanck, K. *J. Phys. Chem.* **1974**, *78*, 727.
(80) Rasmussen, S. C.; Richter, M. M.; Yi, E.; Place, H.; Brewer, K. J. *Inorg. Chem.* **1990**, *29*, 3926.
(81) Bard, A. J.; Faulkner, L. R. *Electrochemical Methods: Fundamentals and Applications*; Second ed.; John Wiley & Sons, Inc.: New York, 2001.
(82) Schwarz, H. A.; Creutz, C. *Inorg. Chem.* **1983**, *22*, 707.
(83) Frink, M. E.; Sprouse, S. D.; Goodwin, H. A.; Watts, R. J.; Ford, P. C. *Inorg. Chem.* **1988**, 27, 1283.
(84) Demas, J. N.; Crosby, G.A. *J. Am. Chem. Soc*. **1970**, 92, 7262.

(85) Demas, J. N.; Crosby, G. A. *J. Phys. Chem.* **1971**, 75, 991.
(86) Carstens, D. H. W.; Crosby, G. A. *J. Mol. Spectrosc.*, **1970**, 34, 113.
(87) Komada, Y.; Yamauchi, S.; Hirota, N. *J. Phys. Chem.*, **1986**, 90, 6425.
(88) Hannon, M.J. *Coord. Chem. Revs.*, **1997**, *162*, 477.
(89) Balzani, V.; Juris, A.; Venturi, M.; Campagna, S.; Serroni, S. *Chem. Rev.* **1996**, 96, 759.
(90) Chiorboli, C.; Indelli, M.T.; Scandola, F. *Top. Curr. Chem.* **2005**, 257, 63.
(91) Humbs, W.; Yersin, H. *Inorg. Chem.* **1996**, 35, 2220.
(92) Calvert, J.M.; Caspar, J.V.; Binstead, R.A.; Westmoreland, T.D.; Meyer, T. J. *J. Am. Chem.* Soc. **1982**, 104, 6620.
(93) Watts, R.J.; Van Houten, J. *J. Am. Chem. Soc.* **1978**, 100, 1718.
(94) Ikeda, S.; Yamamoto, S.; Azumi, T.; Crosby. G. A. *J. Phys. Chem.* **1992**, 96, 6593.
(95) Islam, A.; Ikeda, N.; Nozaki, K.; Ohno, T. *J. Photoch. Photobio. A* **1997**, 106, 61.
(96) Gafney, H. D.; Adamson, A. *J. Am. Chem. Soc.* **1972**, 94, 8238.
(97) Önfelt, B.; Olofsson, J.; Lincoln, P.; Nordén, B. *J. Phys. Chem. A* **2003,** *107,* 1000.
(98) Brennaman, M.K.; Alstrum-Acevedo, J.H.; Fleming, C.N.; Jang, P.; Meyer, T.J.; Papanikolas, J.M. *J. Am. Chem. Soc.* **2002**, 124, 15094.
(99) Friedman, A.E.; Chambron, J.C.; Sauvage, J.P.; Turro, N.J.; Barton. J.K. *J. Am. Chem. Soc.* **1990**, 112, 4960.
(100) Olson, E. J. C.; Hu, D.; Hö1rmann, A.; Jonkman, A.M.; Arkin, M.R.; Stemp, E.D.A.; Barton, J.K.; Barbara, P.F. *J. Am. Chem. Soc.* **1997**, 119, 11458.
(101) Haq, I.; Lincoln, P.; Suh, D.; Norden, B.; Chowdhry, B.Z.; Chaires, J.B. *J. Am. Chem. Soc.* **1995**, 117, 4788.
(102) Barton, J. K.; Kumar, C. V.; Turro, N. J. *J. Am. Chem. Soc.* **1986**, 108, 6391.
(103) Braunstein, C. H.; Baker, A. D.; Strekas, T. C.; Gafney, H. D. *Inorg. Chem.* **1984**, 23, 857.
(104) Fuchs, Y.; Lofters, S.; Dieter, T.; Shi, W.; Morgan, R.; Strekas, T. C.; Gafney, H. D.; Baker, A. D. *J. Am. Chem. Soc.* **1987**, 109, 2691.
(105) Kobayashi, T.; Ohashi, *Y. Chem. Phys. Lett.* **1982**, 86, 289.
(106) Crosby, G. A.; Watts, R. J.; Carstens, D. H. W. *Science,* **1970**, 170*,* 1195.
(107) Dellinger, B.; Kasha, M. *Chem. Phys. Lett.* **1975**, 36, 410.
(108) Morgan, G. T.; Burstall, F. H. *J. Chem. Soc.* **1936**, 41.
(109) Crosby, G. A.; Perkins, W. G.; Klassen, D. M. *J. Chem. Phys.* **1965**, 43**,** 1498.
(110) Gafney, H. D.; Adamson, A. W. *J. Am. Chem. Soc.* **1972**, 94, 8238.
(111) Sabbatini, N.; Balzani, V. *J. Am. Chem. Soc.* **1972**, 94, 7587.
(112) Natarajan, P.; Endicott, F. J. *J. Phys. Chem.* **1973**, 77, 971.
(113) Navon, G.; Sutin, N. *Inorg. Chem.* **1974**, 13, 2159.
(114) Bock, C. R.; Meyer, T. J.; Whitten, D. G. *J. Am. Chem. Soc*. **1974**, 96, 4710.
(115) Balzani, V. Juris, A. *Coord. Chem. Rev.* **2001**, 211, 97.
(116) Creutz, C.; Sutin, N. *Proc. Natl. Acad. Sci. USA* **1975**, 72, 2858.
(117) Zambrana, J. L. Excited-state acid-base & coordination chemistry of ruthenium(ll)diimines: association with various metal cations. Ph.D. Thesis, The City university of New York, New York, NY, 2007

(118) Juris, A.; Balzani, V.; Barigelletti, F.; Campagna, S.; Belser, P.; Von Zelewsky. A. *Coord. Chem. Rev.* **1988**, 84, 85.
(119) Sutin, N. *Acc. Chem. Res.* **1982**, 15, 275.
(120) Sutin, N. *Prog. Inorg. Chem.* **1983**, 30, 441.
(121) Tokel-Takvoryan, N. E.; Hemingway, R. E.; Bard, A. J. *J. Am. Chem. Soc*. **1973**, 95, 6582.
(122) Barltrop, J. A.; Coyle, J. D. *Excited States in Organic Chemistry*; Wiley-Interscience: London, 1975.
(123) Schläfer, H. L.; Gliemann, G. *Basic Principles of Ligand Field Theory*; Wiley-Interscience: London, 1969.
(124) Kamyshny, A. L.; Suisalu, A. P.; Aslanov, L. A. *Coord. Chem. Rev*. **1992**, 117, 1.